

# Sensing and Control of Flows over Membrane Wings

by

Jillian Bohnker

B.S., Mechanical Engineering, Franklin W. Olin College of Engineering, 2010

M.S., Engineering, Brown University, 2014

A dissertation submitted in partial fulfillment of the  
requirements for the degree of Doctor of Philosophy  
in the School of Engineering at Brown University

PROVIDENCE, RHODE ISLAND

May 2019

© Copyright 2019 by Jillian Bohnker

This dissertation by Jillian Bohnker is accepted in its present form  
by the School of Engineering as satisfying the  
dissertation requirement for the degree of Doctor of Philosophy.

Date \_\_\_\_\_

Kenneth S. Breuer, Ph.D., Advisor

Recommended to the Graduate Council

Date \_\_\_\_\_

Daniel Harris, Ph.D., Reader

Date \_\_\_\_\_

David Henann, Ph.D., Reader

Approved by the Graduate Council

Date \_\_\_\_\_

Andrew G. Campbell, Dean of the Graduate School

Abstract of “Sensing and Control of Flows over Membrane Wings” by Jillian Bohnker, Ph.D., Brown University, May 2019

While a wide variety of active flow control techniques have been developed for rigid wings, membrane wings have generally relied on their inherent passive deformation to flow conditions. But as micro-air vehicles (MAVs) become more prevalent, the benefits of membrane wings at low Reynolds number make the development of novel control and sensing techniques particularly relevant. In this work, the foundation is laid for an integrated sensing and control system, in which a membrane wing is constructed from a dielectric elastomer actuator. The membrane material, VHB 4905 (3M), is characterized using a three-element generalized Kelvin-Voigt model, which is fitted to experimental data for creep, relaxation, and steady state AC actuation. The performance of a fixed membrane wing under sinusoidal actuation is demonstrated for a range of angles of attack, freestream velocities, and actuation frequencies. Enhancements in the coefficient of lift of up to 20% are seen within a limited range of experimental parameters. In this regime, actuation is seen to cause or enhance vortex shedding from the leading edge, as visualized with DMD analysis. The root cause of this peak in performance is explored, including the effects of reduced frequency, the location of the separated shear layer, and fluid-induced damping. Finally, integrated self-sensing of the membrane wing is demonstrated. The deformation of the membrane is sensed using the capacitance of the wing, which is measured using an online RLS algorithm. The parameters of the algorithm are optimized, and the performance is validated in a series of benchtop and wind tunnel tests. The correlation between camber and aerodynamic load is demonstrated, and the unsteady camber is linked to large-scale structures in the surrounding flow. Ultimately, the combination of active flow control and integrated sensing may allow the development of closed-loop control of membrane wings, enhancing the capabilities of MAVs.

## Curriculum Vitae

Jillian Bohnker hails from Columbus, Ohio, where she was raised as a faithful follower of Buckeye Nation. She attended Olin College of Engineering in Needham, MA, earning a B.S. in Mechanical Engineering in 2010, following four years of intensive training in blue foam modeling and team-building exercises. Research projects during these years included binary colloidal nucleation and the development of esophageal stents, as well as summer projects in grayscale lithography at Cornell University and the cellular uptake of gold nanoparticles at the National Institute for Material Science in Tsukuba, Japan. Since graduating in 2010, she has been gainfully employed at the Naval Undersea Warfare Center in Newport, RI, where she has worked on a number of projects, ranging from turbulent boundary layer measurements, to magnetostrictive thin-film bridge characterization, to transducer design for both standard and parametric applications. More recently, the complexities of towed array dynamics has captured her interest. While working at NUWC and under the support of a SMART Fellowship, she earned an M.S. in Engineering (Fluids and Thermal Sciences) at Brown University in 2014, studying the performance of dielectric barrier discharge actuators in quiescent flow conditions with Professor Kenny Breuer. Since then, she has been studying the unsteady aerodynamics of membrane wings, with a focus on active flow control and passive self-sensing.

## Preface

The research described herein was conducted under the supervision of Professor Kenneth S. Breuer at the School of Engineering between September 2014 and May 2019. The content includes research presented in the publications and proceedings listed below. To the best of my knowledge, this work is original, except where acknowledgements and references are made. Neither this, nor any substantially similar dissertation, has been or is being submitted for any other degree, diploma, or other qualification at any other university.

### Publications

Kiser, J., Manning, M., Adler, D., & Breuer, K. (2016). A reduced order model for dielectric elastomer actuators over a range of frequencies and prestrains. *Applied Physics Letters*, 109(13), 133506.

Bohnker, J., & Breuer, K. (2019). Control of separated flow using actuated compliant membrane wings. Accepted for publication. *AIAA Journal*.

### Conference Presentations

Bohnker, J., & Breuer, K. (2018, November). Integrated sensing and actuation of unsteady flow-induced membrane deformations. *APS Division of Fluid Dynamics Meeting Abstracts*.

Bohnker, J., & Breuer, K. (2018, July). Control of separated flows over membrane wings using adaptive membrane compliance. *5th International Conference on Experimental Fluid Mechanics*.

Bohnker, J., & Breuer, K. S. (2018, June). Control of separated flows over membrane wings. In *2018 AIAA Flow Control Conference*.

Bohnker, J., & Breuer, K. (2017, November). Separated flow control with actuated membrane wings. In *APS Division of Fluid Dynamics Meeting Abstracts*.

Kiser, J., & Breuer, K. (2016, November). Unsteady aerodynamics of membrane wings with adaptive compliance. In *APS Division of Fluid Dynamics Meeting Abstracts*.

## Acknowledgements

This dissertation would not have been possible without the constant advice and guidance of Dr. Kenny Breuer - I couldn't have asked for a better advisor, and am grateful for his patience and encouragement. Thanks also to my committee members, Dr. Daniel Harris and Dr. David Henann, as well as Dr. Shreyas Mandre, Dr. Jennifer Franck, and Dr. Sharon Swartz, for their valuable technical insights, which have significantly improved this work.

The members of the Breuer Lab during my time here have contributed significantly to this work, both in terms of technical discussion and camaraderie. Thanks to Ben Lyons for assistance building experimental set-ups. Thanks to Gali Alon, Asimanshu Das, and Varghese Mathai for discussions on membrane characterization and set-up and data collection assistance. I'd especially like to thank Cosima Schunk for her friendship (and teaching me PIV!), and Zeynep Temel for giving excellent advice. Our game nights and evenings in the GCB were a highlight of the early years.

I'm grateful to those who encouraged and mentored my earliest interest in research, when I was nearly useless in a lab. Particularly Dr. Rebecca Christianson, who oversaw my first research experience at Olin College, and Dr. Sharon Gerbode, who mentored my first summer research experience. I'm forever grateful for these strong female researchers who were willing to take time out of their busy schedules to guide me on my path. I wouldn't be where I am without you.

I'd like to thank my mentors at the Naval Undersea Warfare Center for helping me navigate the complexities of completing a Ph.D. while working full-time. I'm not sure I would have made the leap from Masters to Ph.D. programs without the advice and encouragement of Dr. Neil Dubois, who answered many silly questions with great patience. And to my supervisor, Dr. Fletcher Blackmon, for being extraordinarily accommodating when I missed more branch meetings and trainings than can be easily counted.

Finally and especially, I'd like to thank my family for all their support and encouragement. To my parents, who've stood by me through years of long-distance visits and who have been unfailingly patient regarding my work commitments. To my brother, Doug, who never hit me quite hard enough to cause permanent brain damage. And to my husband, Chris, who has been unwavering in his emotional support - not to mention doing more than his fair share of household logistics and cleaning. Living my dream wouldn't be possible without you. Finally, I'd like to thank Hannah Bohnker, for literally kicking me in the guts every time I considered slacking off for the last six months. The nugget certainly provided motivation and a clear deadline.

# Contents

<b>Curriculum Vitae</b>	<b>iv</b>
<b>Preface</b>	<b>v</b>
<b>Acknowledgments</b>	<b>vii</b>
<b>1 Introduction</b>	<b>1</b>
1.1 Motivation . . . . .	2
1.2 Literature Review . . . . .	3
1.2.1 Dielectric Elastomer Actuators: Actuation . . . . .	3
1.2.2 Dielectric Elastomer Actuators: Self-sensing . . . . .	5
1.2.3 Membrane Wings . . . . .	7
1.2.4 Active Flow Control . . . . .	9
1.2.5 Active Control of Membrane Wings . . . . .	12
1.3 Outline of the Dissertation . . . . .	13

<b>2</b>	<b>Characterization of DEA actuation</b>	<b>16</b>
2.1	Abstract . . . . .	17
2.2	Introduction . . . . .	17
2.3	Methods . . . . .	19
2.4	Constitutive model . . . . .	20
2.5	Results and Discussion . . . . .	24
2.5.1	Harmonic forcing . . . . .	24
2.5.2	Creep response . . . . .	26
2.6	Conclusions . . . . .	28
<b>3</b>	<b>Control of separated flow using actuated compliant membrane wings</b>	<b>30</b>
3.1	Abstract . . . . .	31
3.2	Introduction . . . . .	31
3.3	Experimental Methods . . . . .	36
3.4	Results and Discussion . . . . .	40
3.4.1	Membrane kinematics . . . . .	40
3.4.2	Effect of actuation on aerodynamic performance . . . . .	45
3.4.3	Actuation amplitude dependency . . . . .	48
3.4.4	Fluid-induced damping . . . . .	49
3.4.5	Actuated velocity fields . . . . .	52
3.5	Conclusions . . . . .	58
<b>4</b>	<b>Capacitive deformation sensing with DEA membranes</b>	<b>62</b>

4.1	Abstract . . . . .	63
4.2	Introduction . . . . .	63
4.3	Methods . . . . .	66
4.3.1	Algorithm optimization . . . . .	68
4.3.2	Benchtop validation . . . . .	69
4.4	Results and Discussion . . . . .	70
4.4.1	Algorithm optimization . . . . .	70
4.4.2	Benchtop validation . . . . .	74
4.5	Conclusions . . . . .	75
<b>5</b>	<b>Sensing aerodynamic load and flow structures using membrane wing deformation</b>	<b>77</b>
5.1	Abstract . . . . .	78
5.2	Introduction . . . . .	78
5.3	Methods . . . . .	80
5.4	Results and Discussion . . . . .	83
5.4.1	Measurement of wing camber . . . . .	83
5.4.2	Measurement of aerodynamic load . . . . .	87
5.4.3	Connection with flow structure . . . . .	90
5.5	Conclusions . . . . .	96
<b>6</b>	<b>Conclusions</b>	<b>98</b>

# List of Tables

3.1	Summary of data collected. Dataset I includes time-resolved and synced PIV, membrane kinematics, and aerodynamic forces and torques. Dataset II includes only forces and torques. . . . .	39
4.1	The range of variables used in the RLS algorithm optimization. . . . .	69

# List of Figures

2.1	(Left) The experimental setup, with membrane prestretched to approximately 250% and grease electrodes applied. (Right) The electrode as identified by the MATLAB post-processing script (gray) with the dashed line showing the bounds of a circle of equivalent area and radius. . . . .	19
2.2	A three-element Kelvin-Voigt viscoelastic model in series with an additional dashpot. Each element represents a relaxation time constant while the additional dashpot represents some amount of irrecoverable strain. . . . .	21
2.3	Steady state strain amplitude time-series (top) at three frequencies, with corresponding voltage excitation (bottom), showing the increasing phase lag and decreasing amplitude as a function of frequency . .	25
2.4	(a) Actuation amplitude as a function of frequency for a membrane under 250-300% prestretch (markers), and the fitted model (dashed lines) (b) Actuation phase lag (relative to driving voltage) as a function of frequency for a membrane under 250-300% prestretch (markers), and the fitted model (dashed lines) . . . . .	26

2.5	Experimental data showing creep and recovery response of a membrane under 250% prestrain and 4 kV <sub>dc</sub> actuation voltage (gray dots), and fitted model (black dashed) . . . . .	27
3.1	Experimental set-up showing (a) the top view of the wing and (b) the wind tunnel test section. . . . .	37
3.2	Comparison of experimental camber with the camber predicted by a potential flow aeroelastic model [1]. . . . .	40
3.3	The time-series amplitude of membrane vibration is shown as a function of actuation frequency under three loading conditions, while actuation frequency is swept at a rate of 1 Hz per second. . . . .	42
3.4	Mean (a, b) and RMS (c, d) camber for a wing at 25°, 10 m/s, and 115 Hz actuation is shown. . . . .	43
3.5	Phase averaged kinematics are shown for a wing at 25°, actuated at 115 Hz under 10 (a), 15 (b), and 20 (c) m/s freestream velocities. Camber of an unactuated wing under the same aerodynamic conditions is shown in black. . . . .	45
3.6	The coefficient of lift for a wing at 25°, actuated at 115 Hz, is shown as a function of time (a, c, e) and phase (b, d, f) for 10 m/s (a, b), 15 m/s (c, d), and 20 m/s (e, f) freestream velocities. . . . .	46
3.7	The effect of reduced frequency on lift enhancement is shown for wings at 25°-30° angle of attack and 10-15 m/s freestream velocity. . . . .	47
3.8	Lift enhancement is shown as a function of angle of attack and freestream velocity for a wing being actuated at (a) 50 Hz, (b) 75 Hz, and (c) 115 Hz. . . . .	48

3.9	The effect of actuation on lift enhancement is shown as a function of coefficient of momentum, $C_\mu$ , for parameters ranging from 15-30° angle of attack, 10-20 m/s freestream velocity, and 50-115 Hz actuation frequency. . . . .	49
3.10	The relationship between (a) mode amplitude and change in normal force coefficient and (b) mode velocity and change in normal force coefficient is shown. (c) The resulting predicted amplitude of vibration is compared with the measured camber amplitude. . . . .	52
3.11	Mean velocity magnitude and streamlines for unactuated wings (a, c, e) and wings actuated at 115 Hz (b, d, f) at 10 m/s freestream velocity and 10° (a, b), 20° (c, d), and 30° (e, f) angle of attack. . . . .	53
3.12	(a) A time-averaged flow field at 20° and 10 m/s freestream velocity is shown, with the separation streamline of an unactuated wing (black solid) and a 115 Hz actuated wing (white dashed) shown. (b) The relative location of the separation streamlines for unactuated wings (solid lines) and actuated wings (dashed lines) for a range of angles of attack from 10° to 30°, with 115 Hz actuation and 10 m/s freestream velocity. . . . .	55
3.13	Spectra showing the frequency content of a wing at 25° and 10 m/s, for an (a) unactuated wing, as well as wings actuated at (b) 50 Hz, (c) 75 Hz, and (d) 115 Hz. . . . .	57
3.14	The DMD mode at the frequency of actuation is shown for the region immediately behind the leading edge of the wing for a range of $Ae$ and $f^+$ conditions (a-f). Additionally, the eigenvalue of these modes is shown in (g). . . . .	58

4.1	The benchtop membrane pressurization set-up, showing a membrane at an intermediate stretch. The compliant electrode, made from carbon grease, is seen on the surface of the transparent membrane. . . .	70
4.2	The effect of $N_c$ on the accuracy of RLS output amplitude is shown for a range of $f_c$ , $f_p$ , $f_s$ , and $\mu$ values. It is seen that accuracy monotonically decreases with increasing $N_c$ , regardless of the value of $f_s/f_p$ , which is indicated by marker color. . . . .	71
4.3	The effect of forgetting factor on the noise level of the RLS estimated capacitance is shown. It is seen that noise increases substantially at forgetting factors lower than 0.9. At higher lambda values, noise is low regardless of the ratio of sampling frequency to capacitance frequency (shown in grayscale). . . . .	72
4.4	The effect of sampling frequency, normalized by probe frequency, on the offset error of the RLS estimated capacitance is shown. As the sampling frequency decreases, the algorithm increasingly underestimates the mean capacitance of the signal. For an offset error of 1%, the sampling frequency should be at least 35 times that of the probe frequency. . . . .	73

4.5	The RLS estimated capacitance is compared to the video-derived capacitance, over the course of six minutes of randomly varying membrane strains. (a) A representative example of video-derived and RLS capacitance values are shown over the course of 20 seconds, including both slow and fast changes in strain. (b) Comparing the values over the entire experiment, very close correlation between the values is seen, suggesting that the algorithm is performing well. (b) The frequency content of the two capacitance values (offset for clarity) compares well, showing that the RLS algorithm successfully captures capacitance variations up to the Nyquist frequency of the video data (30 Hz). . . . .	74
4.6	The error in RLS estimated capacitance $((C_{video} - C_{RLS})/C_{video})$ is shown as a function of normalized capacitance. RLS capacitance estimations are seen to generally underpredict capacitance values at low strains, and become more accurate at higher strains. . . . .	75
5.1	(a) The membrane wing is constructed from a rigid frame, to which the membrane is adhered. The load cell is mounted on a custom angle of attack adapter. (b) The wing is mounted in the center of the wind tunnel test section. Kinematics cameras are used to capture membrane kinematics, 2D-2C PIV is used to measure the surrounding flow, and a single-point laser displacement sensor measures the displacement at the center of a membrane segment. . . . .	81
5.2	Analysis of the error introduced by the spherical cap assumption. (a) The camber predicted for a circular vs. a square membrane under uniform pressure is shown. (b) The error in camber is shown for the range of cambers observed in this work. . . . .	84

5.3	The mean camber as measured by displacement sensor is compared to the mean camber as measured by capacitance for (a) purely sensing (without actuation) and (b) sensing during actuation. Acrylic membrane results are shown in cool colors, while silicone tests are shown in warm colors. The angle of attack is indicated with shade, and the freestream velocity with marker size. Additionally, for tests that included actuation, both off-resonance (20 Hz) and on-resonance actuation frequencies were tested. . . . .	85
5.4	A representative time series of the measured camber is shown, for laser displacement sensor measurements (blue) and capacitive self-sensing estimates (red). Good correlation between the signals is seen, though some variations in amplitude and frequency are seen intermittently. .	86
5.5	The cross-correlation coefficient is shown as a function of camber, for both acrylic and silicone membranes. Very little correlation is seen at low cambers, with correlation coefficients increasing to 0.5-0.8 at cambers of above roughly 4%. This trend holds across all angles of attack and velocities tested, for both acrylic and silicone membranes.	87
5.6	(a) The aerodynamic load normal to the membrane is estimated via capacitance, and compared with the measured normal load. This force is then decomposed into (b) lift and (c) drag using the angle of attack.	89
5.7	Aerodynamic loads are converted into aerodynamic coefficients, including (a) the normal force coefficient, (b) the lift coefficient, and (c) the drag coefficient. Good agreement is seen at higher velocities (larger markers), with loss of accuracy at low velocities (small markers).	89

5.8	(a) The time-averaged vorticity field and streamlines are shown for a membrane wing at $5^\circ$ and 16 m/s. The mean membrane camber is shown (solid black line), as well as the camber standard deviation (dashed lines). Additionally (b) the first POD mode and (c) the second POD mode are shown for the region of interest immediately above the membrane. . . . .	91
5.9	(a) The first three POD modes are shown for the membrane deformation along the chord at quarter-span of the wing. In (b), the cumulative energy captured in the first five POD modes is shown. Over 90% of the dynamics are captured in the first 3 modes. . . . .	92
5.10	The power spectral density is shown for lift, capacitance, membrane strain, and shear layer location at $0.5c$ . The peak frequencies for lift and capacitance are seen to be doubled relative to the peak frequencies for membrane strain and shear layer location. Spectra are offset for clarity. . . . .	93
5.11	The coherence of lift with the shear layer location is shown as a function of (a) time and (b) the chord-wise location on the membrane. Time-based coherence was taken at $0.5c$ , and the spatial coherence was averaged over the full time-series, such that the white dashed line is the average of the time-based plot. In both cases, bands of coherence are seen at $f_{12}$ , $2f_{12}$ , and $2f_{13}$ , with very little coherence at $f_{13}$ . . . . .	94

5.12 The coherence of the capacitance with (a) the first POD mode coefficient and (b) the second POD mode coefficient is shown as a function of time. For the first POD mode, high coherence is seen across the entire time series at  $2f_{12}$ . Less coherence is generally seen with the second POD mode, though there are bands of somewhat enhanced coherence at both  $2f_{12}$  and  $2f_{13}$  . . . . . 95

# CHAPTER ONE

---

## Introduction

## 1.1 Motivation

Micro air vehicles (MAVs) have found increasing use in recent years in a number of applications, ranging from surveillance and inspection, to search and rescue operations. With characteristic dimensions on the order of 15-20 centimeters, MAVs are capable of traversing collapsed buildings, and with relatively low mass and inertia, are often robust to collisions. They can be operated as swarms for efficient mission completion, and individual units can be manufactured relatively cheaply. However, some aspects of aerodynamic performance become challenging at this speed and length scale, particularly with MAVs that employ rigid fixed wings.

At relatively low Reynolds numbers, of the order  $10^3 - 10^5$ , rigid fixed wings suffer from a decreasing lift to drag ratio, an increasing susceptibility to unsteady flow conditions such as gusts, and an increased potential for intermittent flow separation. Membrane wings have been shown to mitigate a number of these factors by passively and dynamically conforming to the surrounding flow. However, when flow separation inevitably occurs, methods for active flow control over membrane wings are limited. The development of such a method, particularly in conjunction with an integrated flow sensor, could substantially improve the performance regime for a fixed membrane wing MAV.

By constructing a membrane wing from a dielectric elastomer actuator (DEA), both active flow control and integrated flow sensing are possible. These benefits are combined with those of passive membrane wings at low Reynolds number, and pave the way for closed-loop control of membrane wing MAVs.

## 1.2 Literature Review

This thesis lies at the intersection of DEAs and membrane wing aerodynamics. Understanding the current state of research across this breadth of technical work is critical - each topic will be reviewed in the following section, as well as the emerging field at their intersection.

### 1.2.1 Dielectric Elastomer Actuators: Actuation

The dielectric elastomer actuator (DEA) was first proposed in 1998 by Pelrine, Kornbluh, and Joseph [2]. The DEA consists of a flexible elastomeric membrane sandwiched between two compliant electrodes. When a voltage is applied across the electrodes, the electrostatic attraction of free charges causes the membrane to thin. Because most membranes used for DEAs are incompressible, this results in an in-plane strain. The amplitude of these strains can be greater than 200%, depending on the properties of the membrane material, the amplitude and direction of prestrain, and a number of other factors [3]. The underlying mechanism of this strain has been shown to be purely a due to Maxwell stress, rather than electrostrictive mechanisms, as thoroughly demonstrated by Kofod *et al.* [4]. When an electric field is applied along the z-direction, this results in an actuation stress that goes as:

$$\sigma_{zz} = -\frac{1}{2}\varepsilon_0\varepsilon E^2 = -\frac{1}{2}\varepsilon_0\varepsilon \frac{V^2}{h^2}, \quad (1.1)$$

$$\sigma_{xx} = \sigma_{yy} = \frac{1}{2}\varepsilon_0\varepsilon E^2 = \frac{1}{2}\varepsilon_0\varepsilon \frac{V^2}{h^2}, \quad (1.2)$$

where  $\sigma_{zz}$  is the out-of-plane Cauchy stress,  $\sigma_{xx,yy}$  are the in-plane Cauchy stress components,  $\varepsilon_0$  is the permittivity of free space,  $\varepsilon$  is the dielectric constant of the

membrane,  $E$  is the applied electric field,  $V$  is the applied voltage, and  $h$  is the deformed thickness of the membrane. This type of actuation can be applied to a wide range of actuator configurations, ranging from rolled configurations common in artificial muscle applications [5], stacked or folded actuators used in linear actuator applications [6], and sheet configurations used for adaptive lenses, loudspeaker, and other applications [7, 8].

To convert the actuation stress to high actuation strain, the membrane material is paramount. For DC operations, or for materials that are primarily elastic, a minimum Young's modulus results in a maximum strain [4]. For AC operations, the viscous properties of the material can dominate, particularly as the frequency is increased [9]. As such, the end application has a strong influence on material selection, with low-loss materials such as silicone often being chosen for unsteady applications that require fast response times, while acrylic materials provide a higher actuation strain for applications that occur on a slower timescale [10].

One of the most common materials for DEA membranes is VHB 4905/4910, an acrylic manufactured by 3M. The performance of VHB as a function of prestrain, frequency, and temperature has been the subject of many studies, widely ranging in complexity. When modeling the viscoelastic behavior, analytical models can range in complexity from a single relaxation time constant [11, 12] to multiple elements of a generalized Kelvin-Voigt [13] or Maxwell model [14] - each element serving to increase the accuracy and range of captured time scales, while also increasing the model's complexity. This principle can be extended to capturing the full spectra of time constants, which is generally accomplished experimentally using a dynamic mechanical analysis (DMA), as demonstrated by Guo *et al.* [15], Sheng *et al.* [12], and Palakodeti *et al.* [9], among others. Still other approaches employ a thermodynamic framework to explore dissipative losses and electromechanical instabilities, such as

works by Chiang Foo *et al.* [16] and Wang *et al.* [17], among others.

In addition to the membrane material itself, the electrode material plays a critical role in actuation. If the electrode loses conductivity as it strains, the actuator will be limited in performance. Some of the most common electrode materials, such as loose carbon powder, carbon grease, and conducting polymers, have been empirically characterized and shown to have varying degrees of increasing resistance with strain [18], with carbon grease demonstrating the least loss. Improved actuation performance has been seen with novel compliant electrode technology, which include patterned thin films and nanoparticle implantation, among other techniques [19].

### 1.2.2 Dielectric Elastomer Actuators: Self-sensing

In addition to their actuation capabilities, DEAs have been used as integrated self-sensors. Changes in physical configuration result in changes in electrical characteristics, which, when combined with knowledge of the membrane material properties, can be interpreted as mechanical strain. As the membrane is deformed, either by actuation or applied mechanical load, the membrane's capacitance, electrode resistance, and dielectric resistance can all vary substantially, and several methods have been developed to take advantages of these variations.

The earliest examples of self-sensing in DEAs often assume that two of the three variables (capacitance, resistance, and dielectric constant) vary negligibly, allowing the sensing algorithm to capture only the remaining variable. Sommer-Larsen *et al.* [20] provided the earliest demonstration of the technique in 2001, using higher-order harmonics in the current response to estimate membrane extension. Soon after, Toth and Goldenberg [21], implemented an empirical relationship to approximate the

variation in electrode resistance, and found the capacitance using the membrane's frequency response function. Other approaches to measuring capacitance include the application of a pulse width modulation signal [22] and treating the membrane and electrodes as a high pass filter [23]. Other work, such as O'Brien *et al.* [24], have explored the use of electrode resistance as the primary sensing variable, but this approach has been shown to have significantly more hysteresis and history dependence than strain measurement via capacitance.

Rizzello *et al.* demonstrated an approach that simultaneously takes electrode resistance and membrane capacitance into account, using an online adaptive algorithm [25, 26]. Treating the membrane and electrodes as a variable RC circuit and neglecting any leakage current across the membrane itself, the problem simplifies into a simple series circuit. By using a probe voltage that is at a higher frequency than that of the changing resistance and capacitance, and a probe sampling frequency of sufficiently short period, the analog RC circuit equations can be discretized and linearized between each voltage and current measurement. The result is a linear-in-parameters equation, which can be solved by adaptive filters. After investigating both the Least Mean Squares (LMS) and Recursive Least Squares (RLS) algorithms, smaller errors were seen with the RLS algorithm. As such, this work will follow the approach Rizzello *et al.* and use an RLS adaptive filter to estimate variable capacitance and resistance.

One method that has proven successful in tracking all three variables was demonstrated by Gisby, O'Brien, and Anderson [27]. In this technique, electrical charge, voltage, and time are plotted in 3D space, and a 2D hyperplane is fitted to the data using regression. The coefficients of the resulting characteristic equation can be used to measure the capacitance, resistance, and leakage current. However, this method resulted in errors as high as 4%, particularly at high strains, which is not significantly

improved from the RLS algorithm developed by Rizzello *et al.* [25], despite increased complexity.

As the complexity and accuracy of self-sensing algorithms improve, additional applications become possible. For example, Xu *et al.* proposed a method to allow for localized strain sensing using a single electrode pair [28]. Recognizing that the resistance of the electrode is a function of the distance from the point of voltage application, Xu *et al.* treats the electrode as a transmission line [29]. In this way, by varying the probe frequency and measuring the decrease in amplitude as a function of position, changes in capacitance can be localized without requiring multiple discrete electrodes. Advances in sensing algorithms such as this may enable the development of more complex applications, such as mode shape sensing or wavenumber frequency analysis of flexible materials in flows.

### 1.2.3 Membrane Wings

Because membranes are flexible, they are intrinsically coupled to the surrounding flow, allowing them to passively adapt to flow conditions. This results in advantages over rigid wings under equivalent conditions, such as delayed stall [30], but also makes analysis and prediction of wing performance increasingly dynamic. Fluid-structure interactions (FSI) result in camber changes and modal vibrations that can, in turn, influence the flow field itself. These interactions can be captured by analytical approaches as simple as an aeroelastic model to predict mean camber of the wing [1,31], to high-fidelity coupled computational models [32] or experiments [33–36] to capture the unsteady vibrations of a membrane in flow. Both mean camber and membrane vibrations have significant influence on the performance of a membrane wing.

The aeroelastic model developed by Waldman and Breuer [1], based on earlier work by Song and Breuer [31], predicts the mean camber of the wing as a function of membrane properties and flow speed. The Young-Laplace equation,

$$\kappa + \frac{p}{T} = 0, \quad (1.3)$$

where  $\kappa$  is the membrane curvature,  $p$  is a uniform pressure loading, and  $T$  is the membrane tension, balances the membrane dynamics with the aerodynamic pressure load. Assuming linear elasticity, uniform pressure distribution, and potential flow, this equation can be solved to show that the ratio of coefficient of lift to membrane stretch and curvature is equal to the aeroelastic constant,

$$Ae = \frac{Eh}{\frac{1}{2}\rho U^2 c}, \quad (1.4)$$

where  $E$  and  $h$  are the membrane's Young's modulus and thickness, respectively,  $c$  is the wing chord, and  $\rho$  and  $U$  are the fluid density and freestream velocity, respectively. Because coefficient of lift, membrane stretch, and membrane curvature are only functions of camber and angle of attack, if the aeroelastic number and angle of attack are known, the mean camber can be predicted.

Membrane vibrations can be as critical to aerodynamic performance as auto-cambering, but the dynamics are considerably more complex [36]. Coupling has been observed with aeroelastic instabilities [32], and FSI may result in lock-in between vibration frequencies and fluidic instability frequencies, resulting in amplification of both membrane motion and excitation of the surrounding flow. This has been studied with coupled computational models, such as the work of Gordnier [32], who showed that close coupling of the membrane vibration with vortex shedding directly results in delayed stall relative to equivalent rigid wings. This was confirmed experimentally

by Rojratsirikul *et al.* [36], who studied the coupling of membrane vibration to vortex shedding, as compared to rigid cambered airfoils.

Because membrane vibrations are very sensitive to the location and unsteadiness of the separated shear layer [36], the mode of membrane vibration is strongly a function of Reynolds number and angle of attack, as well as membrane prestrain or excess length. Rojratsirikul *et al.* focused on the effect of prestrain or excess length on membrane dynamics, showing that excess length generally resulted in higher amplitude vibration and earlier roll-up of vortices than membranes under pretension, which approached the performance of rigid wings as pretension increases [35]. Later work from Rojratsirikul *et al.* focused on the modal shape on low aspect ratio wings, where the tip vortex often generates spanwise modes that would not be present in large aspect ratio wings [34]. Finally, it has been shown by both Rojratsirikul *et al.* and Tregidgo *et al.* that flow conditions (angle of attack and freestream velocity) strongly influence the mode and amplitude of vibration [33,34]. A number of regimes were observed by Tregidgo *et al.*, ranging from higher order modes with low amplitude when the flow is attached to the wing, to high amplitude second order modes after separation, which result from interactions with the separated shear layer [33].

#### **1.2.4 Active Flow Control**

Active flow control can be used to accomplish a number of goals, and the methods used can vary substantially. Often, flow control is meant to interact with a flow that has partially or fully separated from the suction surface of the wing, either acting to reattach the flow (separation control) or to reduce the degree of separation (separated flow control) [37]. This is often accomplished through the injection of

momentum into the separated flow, either directly or through excitation of fluidic instabilities. Depending on the degree of separation, this additional momentum can overcome the momentum deficit that led to separation, reattaching the flow.

This addition of momentum has been accomplished in many ways, including surface morphing and flaps [38–40], acoustic excitation [41], plasma actuators [42], and steady or unsteady blowing [43,44], among other methods. However, the limitations in many of these methods, such as sensitivity to experimental conditions for effective acoustic excitation, or design constraints for continuous blowing methods, have led to the relative dominance of synthetic jet actuators. These actuators alternate between blowing and suction, such that the net mass flux is zero. However, due to flow separation and vortex formation that occurs at the edge of the actuator orifice during the blowing half-cycle, the resulting momentum flux is positive and a jet is formed. The spatial and temporal characteristics of this jet are complex, and have been shown to be a function of actuation frequency, actuation amplitude, the surrounding flow, and actuator geometry, among other factors [43].

Actuation frequency is perhaps one of the most critical factors to synthetic jet performance, as is often expressed in terms of the reduced frequency,  $f^+ = fc/U$ , where  $f$  is the actuation frequency,  $c$  is the wing chord length, and  $U$  is the freestream velocity [45]. Effective actuation regimes can be seen at reduced frequencies ranging from  $\mathcal{O}(1)$  to  $\mathcal{O}(10)$ , or even higher [46]. At low reduced frequencies, discrete vortices are seen at or near the frequency of actuation, suggesting that the unsteady momentum addition is interacting with flow field instabilities to result in vortex roll-up. Within this regime, maximum performance is seen to occur at reduced frequencies closely aligned to the flow field instability. At higher actuation frequencies, no discrete vortex formation is observed, and power spectral density measurements of the flow field suggest that the actuation resulted in tripping transition from lam-

inear to turbulent flow, thus increasing the lift to pressure drag ratio. In this regime, actuation authority is nearly invariant with actuation frequency [46].

The coefficient of momentum is often used as a normalized measurement of the actuation amplitude. This coefficient captures the ratio of the actuator-generated momentum to that of the freestream, such that:

$$C_\mu = \frac{\rho_j U_j^2 G}{0.5 \rho_\infty U_\infty^2 L}, \quad (1.5)$$

where  $j$  refers to parameters of the jet,  $\infty$  refers to parameters of the freestream,  $G$  is the actuator slot width, and  $L$  is typically the wing chord [44]. Generally, increasing  $C_\mu$  values lead to increasing flow control, with diminishing returns past a certain point. The ideal  $C_\mu$  value is a function of Reynolds number and airfoil shape, among other variables [47].

Finally, Reynolds number has been shown to be a significant factor in the performance of synthetic jet actuators [47]. At Reynolds numbers less than  $10^5$ , it is difficult or impossible to force transition to turbulence, making excitation of flow instabilities the primary method of flow control. As Reynolds number is increased, the effects of forced transition to turbulence and control of separation are closely related, but even as Reynolds number approaches  $10^7$ , where transition has occurred naturally, active flow control with unsteady forcing remains viable [47]. The ability of synthetic jet actuators to effectively control flow through this wide range of Reynolds numbers makes them a highly versatile flow control tool.

### 1.2.5 Active Control of Membrane Wings

Membrane wings constructed from a DEA have been studied by several groups, both for DC camber control [48–50], and sinusoidal flow control [51]. DC actuation voltages provide a direct method of control of the wing camber, while AC actuation voltages have less effect on mean camber. Despite minimal change in mean membrane camber, sinusoidal variations in the membrane compliance can have a substantial effect on the surrounding flow.

Hays *et al.* [48] first studied the effect of DC voltage on a DEA membrane wing, demonstrating that wing camber can be significantly increased by application of voltage. Control of wing camber, in turn, significantly affected the aerodynamic performance of the wing, and the optimum aerodynamic efficiency was found to be a function of applied voltage, prestrain, and Reynolds number. Additional work from Hays *et al.* [49] demonstrates the effect of DC voltage on the membrane resonance frequency, as well as the flow field. The reduction in tension caused by actuation resulted in decreased resonance frequency. Additionally, increasing actuation voltage was seen to result in an increasing region of recirculation on the suction side of the wing.

By nature, fluid-structure interactions are fundamental to the performance of a membrane wing, making the material properties of the actuator itself of critical importance. Buoso and Palacios [52] numerically studied the effect of membrane viscoelasticity on aerodynamic performance of an actuated wing, finding decreased aerodynamic efficiency relative to the fully elastic membrane during AC actuation. However, this decrease in aerodynamic performance was balanced by an decreased sensitivity to unsteady flow disturbances. Regarding the effect of DEA configuration, Barbu *et al.* [50] experimentally studied the effect of prestrain on the control

authority and aerodynamic performance of DC-actuated DEA wings, finding lower prestrains to provide both higher control authority as well as improved aerodynamic performance.

This thesis closely follows in the footsteps of Curet and Breuer [51], who first demonstrated the effect of modulating compliance of a membrane wing using an AC actuation voltage. Actuation at specific reduced frequencies was found to significantly increase lift and delay stall. This is in good agreement with numerical modeling by Buoso and Palacios [53], who showed that the effect of harmonic actuation can either increase or decrease the aerodynamic efficiency, depending on the relationship between actuation frequency and the membrane resonance.

### **1.3 Outline of the Dissertation**

In this thesis, the development of a membrane wing capable of simultaneous active flow control and sensing is presented. The thesis is composed of four chapters, in addition to this introduction and literature review.

In the second chapter, the characterization of a membrane will be presented. This material, VHB, is commercially manufactured by the 3M Company, and known to be highly viscoelastic. We will characterize the viscoelastic losses using a three-element generalized Kelvin-Voigt model, with parameters fitted using experimental data. Data was captured by applying high voltage to a biaxially-stretched VHB membrane, and measuring in-plane strain for both a DC voltage as well as steady state AC responses for a range of frequencies. We demonstrate that a relatively simple model can be used to accurately predict the actuation performance of the

membrane over a range of frequencies. This work consists of an expanded version of Kiser *et al.* [54]. Additions to the referenced work include discussion on the breadth of applicability, the limitations imposed by certain assumptions (including the effect of an additional dashpot in the generalized model, the impact of varying prestrain values, etc), and an additional figure with phase-averaged strain data. This chapter includes contributions from Michael Manning and David Adler, who collected and processed the video data measuring the creep and relaxation of the membrane. All experimental set-up, post-processing analysis, and writing was completed by the author.

In the third chapter, the effect of unsteady actuation of the membrane wing is explored. By actuating the membrane with an AC voltage, an in-plane strain is generated, which acts to reduce the pretension. When this reduction in tension is coupled with the aerodynamic load, the high-voltage actuation serves as a method to dynamically control the camber of the wing. The effect of this varying camber was explored for a range of angles of attack, freestream velocities, and actuation frequencies. Lift enhancements of up to 20% were observed over a limited range of experimental conditions. Ultimately, this lift enhancement is tied to leading edge vortex shedding that is initiated or enhanced by the varying camber, as visualized with phase-averaged particle image velocimetry (PIV). The effect of reduced frequency, fluid-induced damping, and separated shear layer location will be examined. This chapter consists of the manuscript entitled "Control of separated flow using actuated compliant membrane wings", which has been accepted for publication in the AIAA Journal.

In the fourth chapter, a method for integrated membrane deformation sensing is presented. The membrane and electrodes are treated as a series RC circuit, following the work of Rizzello *et al.* [25]. Using known relationships between voltage, current,

resistance, and capacitance for a simple RC circuit, the constitutive equations can be rewritten into linear-in-parameters form, appropriate for application to online adaptive algorithms. By applying a probe voltage that is sufficiently higher than the frequency of deformation, the voltage and current measured across the membrane are input in a recursive least squares algorithm to estimate the value of resistance and capacitance at each time-step. This RLS algorithm is optimized over a range of deformation frequencies, probe frequencies, sampling frequencies, and forgetting factors. The algorithm is validated by comparing the estimated capacitance with that predicted by video data of a deforming membrane, and good correlation is seen. Limitations of the approach are discussed.

Finally, in the fifth chapter, capacitive self-sensing is applied to an aerodynamic environment. Because the membrane wing camber is integrally tied to the surrounding flow conditions, both mean and unsteady aerodynamic forces can be sensed if the membrane kinematics and material properties are known. The optimized and validated RLS algorithm described in the previous chapter is used to measure the capacitance of a membrane wing. Using this capacitance, the in-plane strain is estimated, which naturally leads to the instantaneous camber. In a series of wind tunnel experiments, this camber estimation is compared with true camber measurements, and a good correlation is seen. Links between the camber and the surrounding flow field are presented, both for mean lift and drag, as well as large-scale flow field structures, such as leading edge vortex shedding. This chapter includes work by Asimanshu Das, who assisted with data collection to validate the relationship between camber and capacitance. The author completed the test set-up, the remainder of data collection, all data post-processing, and writing.

## CHAPTER TWO

---

### **Characterization of DEA actuation**

## 2.1 Abstract

The actuation strain of an equibiaxially prestrained dielectric elastomer membrane is studied as a function of driving frequency and prestrain. Experimental data is gathered on the membrane's creep and recovery following DC actuation, as well as the steady state amplitude and phase for AC driving voltages ranging from 2 to 40 Hz. The effect of prestretch on steady state actuation was also investigated, using membranes of both 250% and 300% prestretch. A three-element generalized Kelvin-Voigt model is developed to capture the transient and steady-state actuation responses as a function of frequency and prestrain. We show that, despite its relative simplicity, this model captures the relevant timescales for the membrane behavior with good fidelity and can be used to accurately predict the actuation magnitude and phase as a function of time over a range of actuation configurations and driving conditions.

## 2.2 Introduction

Dielectric elastomer (DE) membranes have gained popularity as electromechanical actuators due to their simple and light design, fast response times, and high actuation strains. The actuator consists of a thin membrane (on the order of 0.5-1 mm) with a compliant electrode on either side, forming a capacitor. When charge accumulates on the electrodes, a Maxwell pressure acts upon the soft elastomer and causes the membrane to expand laterally. These actuators have been used in a wide variety of applications including energy harvesting [55,56], robotic muscles [5,57], and adaptive compliance membrane wings [48,51].

Despite the many advantages, some DE membrane materials suffer from significant viscoelastic losses which make it difficult to drive the actuators periodically [9]. A great deal of work has been done to understand and model the viscoelastic properties of one of the most common DE actuator materials, VHB (3M). Experimental studies, such as the work of Palakodeti and Kessler [9], use dynamic mechanical analysis to quantify the stiffness and efficiency as a function of temperature and frequency. Other experimentalists, such as Wissler and Mazza [58], have focused on large strain experiments to compare and optimize hyperelastic material models, but have largely neglected sinusoidal excitation. Analytical viscoelastic models of varying complexity have been implemented, from the relatively simple standard linear solid (SLS) model used by Wang *et al.* [11] and Sheng *et al.* [12], to the full-spectrum generalized Maxwell model used by Guo *et al.* [15]. The simple analytical SLS model can be quickly and easily evaluated, but diverges from experimental data as frequency or prestrain are changed, while the results of Guo *et al.* have not been compared with sinusoidal actuation results. Other models, such as the nonequilibrium thermodynamic approaches of Suo [59] can include effects such as dielectric relaxation. Numerical approaches have also been used, such as the work of Goulbourne *et al.* [60] and Park and Nguyen [61], who accounted for geometric and material nonlinearities in a finite element approach, but these numerical approaches have been focused on DC actuation.

In this work, a reduced order viscoelastic analysis of a DE membrane (VHB4905) is presented. Experimental data is taken on actuation strain as a function of membrane prestrain and actuation frequency. Viscoelastic creep and recovery are also captured. A modified three-element Kelvin-Voigt model is used to generate a constitutive equation for actuation strain. The seven necessary coefficients of the resulting linear differential equation are fit to experimental data, resulting in a reduced order

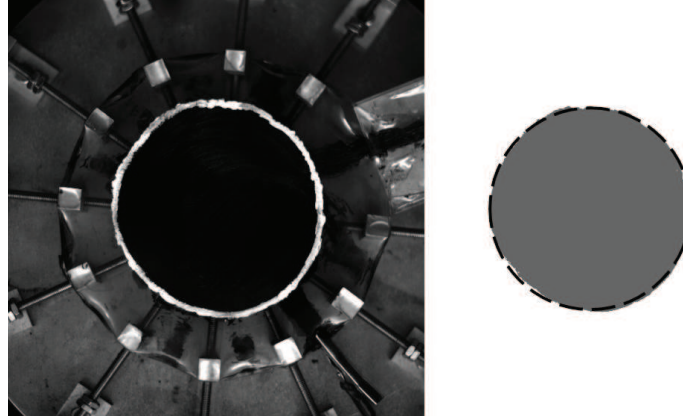


**Figure 2.1:** (Left) The experimental setup, with membrane prestretched to approximately 250% and grease electrodes applied. (Right) The electrode as identified by the MATLAB post-processing script (gray) with the dashed line showing the bounds of a circle of equivalent area and radius.

model that captures both DC and sinusoidal actuation strains. This model can easily be applied to predict the actuation behavior of an arbitrary forcing input.

## 2.3 Methods

The dielectric elastomer, VHB4905 (3M), was attached using its own adhesive to twelve posts, equally distributed around the perimeter of a 70 mm diameter circle. The posts were then expanded radially to apply equibiaxial (radial) strain to the membrane. Conductive grease (MG Chemicals, #846) was applied as an electrode, to either side of the stretched membrane and outlined with a white paint marker. Voltage was applied using a high voltage amplifier (Trek, model 5/80). Video of the actuating membrane was collected with a high speed camera (1024 pixels  $\times$  1024 pixels) (Phantom Miro 340) at frame rates which varied depending on the experiment. Two experiments were conducted: sinusoidal forcing was used to measure steady-state strain amplitude and phase as a function of driving frequency and amplitude, and creep and recovery were measured following the impulsive application and removal of a DC electric field.

To capture the steady state strain amplitude and phase, voltages of the form  $V(t) = 2000(1 + \sin(2\pi ft))$  were applied to membranes at both 250% and 300% prestrain, with frequencies,  $f$ , ranging from 2 to 40 Hz. Following ten seconds of continuous actuation, videos were taken at 801 fps, chosen to ensure complete coverage of the actuation cycle. Applied voltage data was collected synchronously so that the phase between stress and strain can be recovered. For the creep tests, a 4 kV<sub>dc</sub> step function voltage was applied to a membrane at 250% prestrain, and the actuation strain was captured at 60 fps for 10 seconds, at which point the voltage was removed and the membrane's strain recovery was captured for an additional 28 seconds.

Videos were imported into MATLAB for post-processing using the Image Processing Toolbox. Each frame was converted to black and white using a constant brightness threshold and inverted such that the black electrode was labeled as an object in B/W space. The white line outlining the electrode served to create a clear boundary between the electrode and the rest of the image. The area of the electrode was measured for each frame and the average radius was calculated with the assumption of a circular electrode, as shown in Figure 2.1. The electrode radius was converted into actuation strain by dividing by the radius of the unactuated (pre-strained) electrode.

## 2.4 Constitutive model

A three-element generalized Kelvin-Voigt model was used to model the membrane behavior, allowing for the inclusion of fast, intermediate, and slow relaxation [62]. A damper was added to capture irrecoverable strain (Figure 2.2). It should be noted

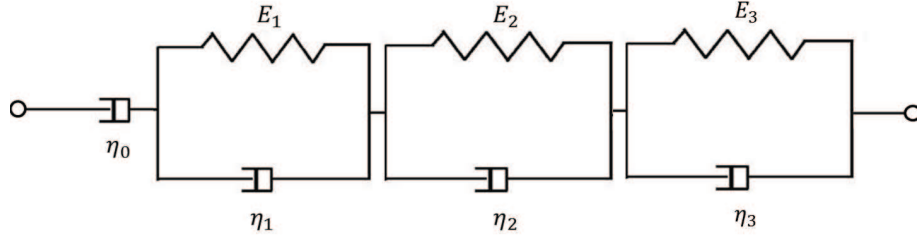


**Figure 2.2:** A three-element Kelvin-Voigt viscoelastic model in series with an additional dashpot. Each element represents a relaxation time constant while the additional dashpot represents some amount of irrecoverable strain.

that the material is not characterized by truly irrecoverable strain - the additional damper only reflects strains that are not recovered over the duration of these experiments. This limits the applicability of the model to actuation on the order of 30-40 seconds of duration.

In this system, the stress across each unit is equal to the stress across the entire system, and the strain across each individual unit can be summed to find the strain across the entire system. Assuming linear behavior, the strain across the system is defined as:

$$\varepsilon = \sigma \left( \frac{1}{\eta_0 D} + \frac{1}{E_1 + \eta_1 D} + \frac{1}{E_2 + \eta_2 D} + \frac{1}{E_3 + \eta_3 D} \right) \quad (2.1)$$

where  $\sigma$  is total stress,  $\varepsilon$  is total strain,  $\eta_i$  is the respective dashpot constant,  $E_i$  is the respective spring constant, and  $D$  is the derivative operator in time [62]. Solving for stress and expressing the equation as a linear function of stress, strain, and their time derivatives (denoted here with dots):

$$A_1 \dot{\varepsilon} + A_2 \ddot{\varepsilon} + A_3 \dddot{\varepsilon} + A_4 \ddddot{\varepsilon} = B_1 \sigma + B_2 \dot{\sigma} + B_3 \ddot{\sigma} + B_4 \dddot{\sigma} \quad (2.2)$$

where

$$A_1 = E_1 E_2 E_3 \eta_0$$

$$A_2 = E_2 E_3 \eta_1 \eta_0 + E_1 E_3 \eta_2 \eta_0 + E_1 E_2 \eta_3 \eta_0$$

$$A_3 = E_3 \eta_1 \eta_2 \eta_0 + E_1 \eta_2 \eta_3 \eta_0 + E_2 \eta_1 \eta_3 \eta_0$$

$$A_4 = \eta_1 \eta_2 \eta_3 \eta_0$$

$$B_1 = E_1 E_2 E_3$$

$$B_2 = E_1 E_3 \eta_2 + E_2 E_3 \eta_1 + E_1 E_2 \eta_3 + E_2 E_3 \eta_0 +$$

$$E_1 E_3 \eta_0 + E_1 E_2 \eta_0$$

$$B_3 = E_3 \eta_1 \eta_2 + E_1 \eta_2 \eta_3 + E_2 \eta_1 \eta_3 + E_2 \eta_3 \eta_0 + E_3 \eta_2 \eta_0 +$$

$$E_1 \eta_3 \eta_0 + E_3 \eta_1 \eta_0 + E_1 \eta_2 \eta_0 + E_2 \eta_1 \eta_0$$

$$B_4 = \eta_1 \eta_2 \eta_3 + \eta_2 \eta_3 \eta_0 + \eta_1 \eta_3 \eta_0 + \eta_1 \eta_2 \eta_0$$

This differential equation can be solved for any arbitrary stress input to predict the output strain.

The actuation stress has been shown by Kofod *et al.* [4] and Ma and Cross [63] to be accurately and completely described by a Maxwell pressure, such that  $\sigma_{zz} = -0.5\epsilon_0\epsilon_r E^2$ , where  $\sigma_{zz}$  is the stress normal to the membrane,  $\epsilon_0$  and  $\epsilon_r$  are the permittivity of free space and the relative permittivity of VHB, respectively, and  $E$  is the electric field across the membrane. Note that this analysis assumes that the electrode is large enough to neglect both mechanical and electrical edge effects - the electrical field is treated as purely 1D, and no mechanical tractions are included in the out-of-plane direction. Balancing the out-of-plane and in-plane stress state and applying the incompressibility boundary condition, the stress in the plane of the membrane is equal to  $\sigma_{xx} = \sigma_{yy} = 0.5\epsilon_0\epsilon_r E^2$ . The electric field is inversely

proportional to the thickness of the membrane, which is a function of the unstrained membrane thickness ( $h_0$ ) and applied prestretch ( $\lambda_0$ ):

$$E = \frac{\lambda_0^2 V}{h_0} \quad (2.3)$$

where  $h_0$  is the unstrained membrane thickness and  $\lambda_0$  is the prestretch applied to the membrane. Therefore, the applied stress can be expressed as

$$\sigma = \frac{1}{2} \epsilon_0 \epsilon_r \frac{\lambda_0^4 V^2}{h_0^2}. \quad (2.4)$$

This stress can be applied to Equation 2.2 which can then be solved for an arbitrary voltage input to predict the output actuation strain. The seven viscoelastic parameters can be fit to experimental data, using harmonic forcing data and creep/recovery responses.

Two simplifying assumptions are made to allow the differential equation to remain linear. First, this model assumes a linear elastic behavior of the dielectric. While it is known that VHB behaves hyperelastically at high strains [64], it can be approximated as linear for the small actuation strains surrounding any given prestrain. Furthermore, in this work, a single set of viscoelastic material parameters will be found for both 250% and 300% prestrain values, which may restrict the level of accuracy achieved. Secondly, we assume that the electric field remains constant during actuation. In actuality, the membrane thickness decreases as the membrane is actuated, increasing the electric field, until it balances the elastic restoring force. The implications of this simplification will be assessed in the following discussion.

## 2.5 Results and Discussion

The parameters of the three element Kelvin-Voigt model described above can be best understood by considering the relaxation time constants [62] ( $\tau_i = \eta_i/E_i$ ) that each element represents. Lower frequencies are dominated by longer time constants and higher frequencies by shorter time constants. Because creep and recovery occur on a much longer timescale than the sinusoidal data collected, optimization of the long time constant parameters can be carried out independently from the short time constant data, saving significant computational time. Therefore, steady state strain amplitude and phase data are used to tune parameters associated with short and intermediate time constants, while creep and recovery data are used to isolate the response associated with the long time constant. Each set of parameters for each time constant were optimized iteratively to minimize mean squared error.  $E_1, \eta_1, E_2,$  and  $\eta_2$  were each optimized to the amplitude and phase data of steady-state harmonic actuation, while  $E_3, \eta_3,$  and  $\eta_0$  were held constant. Once the optimum parameters for the short time constants were determined, the long time constant parameters were freely varied to fit the creep/relaxation data. The resulting optimum parameters are  $E_1 = 9300, \eta_1 = 22, E_2 = 1200, \eta_2 = 42, E_3 = 550, \eta_3 = 250,$  and  $\eta_0 = 25000,$  with corresponding relaxation time constants of  $\tau_1 = 0.0024, \tau_2 = 0.035,$  and  $\tau_3 = 2.2$  seconds.

### 2.5.1 Harmonic forcing

As discussed, one difficulty of using VHB as a DE actuator is that the viscous damping results in loss of actuation authority when actuated periodically. Figure 2.3 shows the steady-state actuation strains achieved under sinusoidal voltages, where

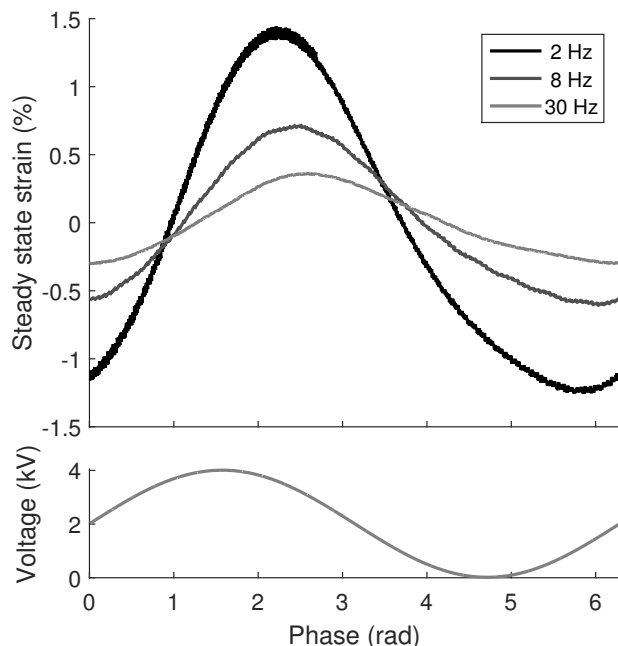


**Figure 2.3:** Steady state strain amplitude time-series (top) at three frequencies, with corresponding voltage excitation (bottom), showing the increasing phase lag and decreasing amplitude as a function of frequency

each frequency trial consisted of 1.21 seconds of data sampled at 801 Hz following 10 seconds of unrecorded actuation. All cycles are plotted relative to the phase of the driving voltage, such that there are 2.4 cycles of 2 Hz data overlaid, 9.7 cycles of 8 Hz data, and 36.3 cycles of 30 Hz data. As frequency is increased (and, consequently, rate of strain), viscous damping becomes more prominent.

The steady state frequency response is described in terms of amplitude and phase relative to the driving voltage. The steady state peak-to-peak strain actuation for frequencies from 2 to 40 Hz is shown in Figure 2.4a, decreasing from a maximum of 2.7% at 2 Hz for a membrane under 300% to a minimum of 0.28% at 40 Hz for a membrane under 250% prestrain. Comparing the resulting optimized fit with the experimental data, the model is seen to closely fit experimental data corresponding to prestretch values of 250%, though it slightly underestimates the amplitude data at 300% prestrain. This underestimation is likely due to the assumption that a single

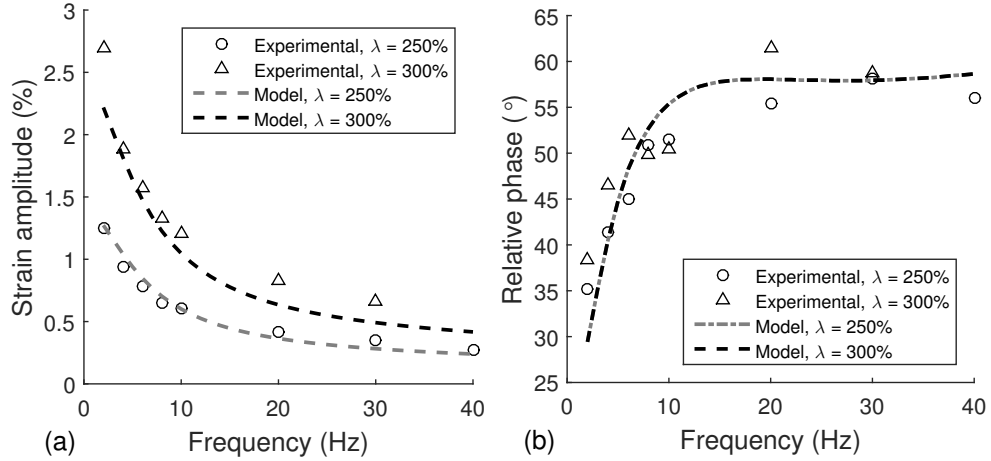


**Figure 2.4:** (a) Actuation amplitude as a function of frequency for a membrane under 250-300% prestretch (markers), and the fitted model (dashed lines) (b) Actuation phase lag (relative to driving voltage) as a function of frequency for a membrane under 250-300% prestretch (markers), and the fitted model (dashed lines)

set of viscoelastic parameters can capture the dynamics of both prestrain values, despite the material’s underlying hyperelastic properties.

The phase delay relative to the driving voltage is shown in Figure 2.4b, where it is seen to be independent of prestrain and to increase at low frequencies before leveling off at a phase lag of approximately 60 degrees at 15 Hz. This decreased efficiency with increasing frequency is consistent with the results of Palakodeti and Kessler [9], among others. The model captures the observed lack of dependence on prestretch, and the phase lag with respect to frequency is well captured. Because phase lag in viscoelastic materials is a result of the loss modulus, which is a bulk property [62], it is reasonable that the phase lag would be independent of prestretch.

## 2.5.2 Creep response

The creep and recovery response is shown in the gray curve of Figure 2.5, where the strain increases only gradually to the steady-state value after a step voltage is

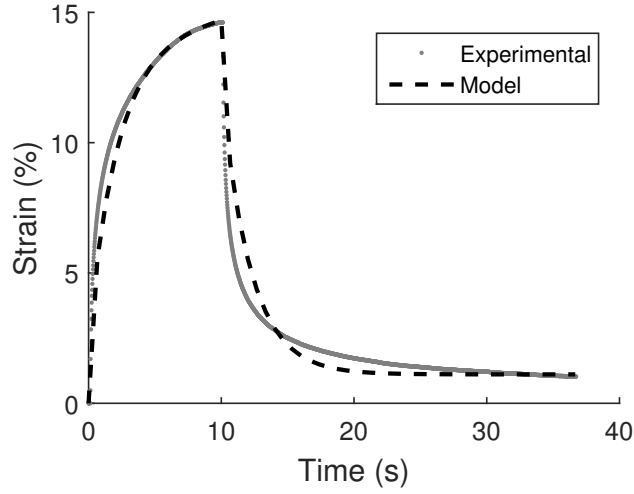


**Figure 2.5:** Experimental data showing creep and recovery response of a membrane under 250% prestrain and 4 kV<sub>dc</sub> actuation voltage (gray dots), and fitted model (black dashed)

applied at  $t = 0$ , and does not fully recover to 0% strain after the voltage is removed. Comparing the optimized model fit to this data, we see that the model fits the creep data closely, though the model predicts the recovery to be somewhat sharper than the experimental data. This is most likely due to the assumptions required to keep the model linear - the material is treated as linear viscoelastic, and the change in membrane thickness due to actuation is neglected. The effect of variable membrane thickness is greatest when the observed actuation strain is high, as it is here. Following the linear elastic and unconstrained analysis by Pelrine *et al.* [2], the thickness strain can be estimated by using the in-plane actuated strain and assuming incompressibility. For the maximum observed strain of 14.6%, the thickness strain can reach 23.8%. Applying the modified thickness to Eq 2.4, errors of up to 33.6% are possible. Consistent with Figure 2.5, the initial slope of the model would be underestimated relative to the experimental data, because the elastic restoring force is neglected.

## 2.6 Conclusions

The dielectric membrane used here, VHB4905, is known to be an effective material for dielectric membrane actuation, but has limited actuation authority in AC applications due to significant viscoelastic losses. Additionally, its hyperelastic and nonlinear nature can lead to complicated and computationally expensive models. However, for a given range of frequencies and prestrains, it is possible to develop a reduced order viscoelastic model that captures the relevant control parameters. In this case, three relaxation time constants were able to capture actuation behavior ranging from DC to 40 Hz AC driving voltage, and likely beyond. By utilizing least-squares fitting on both creep/recovery and frequency sweep experimental data, a generic linear differential equation was developed that captures the key physics - both steady state strains and amplitude/phase trends.

It should be emphasized that the viscoelastic parameters found in this analysis are not universal, but are only valid based on the assumptions made and the experimental conditions tested. Significantly varying the membrane prestretch or the actuation frequency and duration could affect the dominant time constants of the optimized Kelvin-Voigt model. Because the analysis relies on linear viscoelasticity, loss of accuracy would similarly be expected if the amplitude of actuation was significantly changed. Other variables, such as boundary conditions or the electroded area fraction, may also impact the results. Ultimately, this approach was designed to balance simplicity with accuracy, such that it could be applied independently for the experimental conditions of the application at hand, rather than accounting for every possible configuration. Using only a small set of experiments, a short series of Kelvin-Voigt elements can be used to generate a model to predict actuation strains with good fidelity. Following the optimization of the viscoelastic parameters, any

arbitrary voltage input can be converted to applied stress and used to predict the resulting strain, within the limits described above.

## **Acknowledgements**

This work was supported by AFOSR, monitored by Dr. Douglas Smith, as well as the In-House Laboratory Independent Research program at the Naval Undersea Warfare Center, Division Newport (JB). Many thanks go to the individuals of the Breuer Lab for valuable discussion, technical assistance, and glorious camaraderie.

# CHAPTER THREE

---

## Control of separated flow using actuated compliant membrane wings

## 3.1 Abstract

Membrane wings exhibit several aerodynamic advantages at low Reynolds numbers, passively adapting to flow conditions and delaying stall to significantly higher angles of attack relative to rigid wings. Rigid wings, on the other hand, often rely on active flow control mechanisms to achieve high angles of attack, injecting momentum to induce vortex roll-up in the shear layer. Active flow control for membrane wings is limited by the flexible nature of the wing surface. However, it is possible to achieve active flow control with a membrane wing by using a dielectric elastomer actuator as the membrane material. In this work, the performance of a sinusoidally actuated membrane wing is characterized for a range of actuation frequencies, freestream velocities, and angles of attack. Lift measurements show lift enhancement of up to 20%. Time-resolved membrane kinematics are used to calculate the coefficient of added momentum of the actuator, and the effect on the flow field is shown using phase-averaged particle image velocimetry measurements. Dynamic mode decomposition is used to show vortical structures being shed from the leading edge in phase with actuation, and comparisons are made with synthetic jet literature to show the similarities to separated flow control techniques used on rigid wings.

## 3.2 Introduction

At small scale, (Reynolds numbers  $\sim 10^3 - 10^5$ ), a number of factors contribute to the deteriorating aerodynamic performance of wings. For non-aerodynamic (structural) reasons, wings tend to be low-aspect ratio, resulting in a relatively high induced drag. Additionally, due to the typical dimensions of vehicles in this range of Reynolds numbers, unsteady or gusty flow conditions can have disproportionate effects on vehicle

dynamics. Finally, flow separation and transition from laminar to turbulent conditions may occur intermittently, particularly in the presence of gusty conditions or freestream turbulence. Rigid wings have limited ability to respond to flow separation, often requiring active flow control mechanisms. Common examples of active flow control devices include continuous suction or blowing, and unsteady excitation methods such as acoustic excitation [65], oscillatory camber [40], and synthetic jets [37, 44–46, 66, 67]. These approaches have been applied primarily to relatively low Reynolds numbers ( $10^4 - 10^5$ ), with wing cross-sections varying from flat plates to thin NACA airfoils.

Oscillatory actuation mechanisms have the advantage of being able to couple with natural frequencies in the system, such as the wake shedding frequency of the wing or the primary instability frequency of the separated shear layer [46], and a significant body of work exists to quantify this type of actuation on aerodynamic performance. The effect of actuation can be separated into two primary categories: separation control and separated flow control [37]. In separation control, the momentum injected into the separated shear layer is sufficient to reattach a separated flow, which simultaneously decreases drag and increases lift. However, as angle of attack or freestream velocity increases, the energy injected into the separated flow is insufficient to achieve reattachment. In this condition (separated flow control), the energy injected by the actuation mechanism serves to perturb the shear layer, resulting in a roll-up of vorticity and periodic shedding of vortices. With each shed vortex, lift is enhanced (as well as drag, roughly proportionally). This type of control can be useful for situations that demand operation at high angles of attack and optimum lift, but where increased drag is permissible, such as during tight turning maneuvers.

Frequency of actuation is a significant consideration in flow control applications

utilizing oscillatory mechanisms, with reduced frequencies ( $f^+ = f_{act}c/U_\infty$ ) ranging from  $f^+ \sim \mathcal{O}(1)$  to  $\mathcal{O}(100)$  having different effects on the surrounding flow field [45]. At  $f^+ \sim \mathcal{O}(1)$ , where this work focuses, large vortical structures are seen to form in the separated shear layer. For flows that remain separated during actuation, these vortical structures result in a decrease in the recirculation region and an increase in time-averaged lift [37]. The actuation frequency is often chosen to correspond with a natural frequency of the surrounding flow, such as the shear-layer instability frequency [41] or the vortex shedding frequency [68].

In contrast to the active control necessary for rigid wings in unsteady flow conditions, membrane wings have been shown to passively adapt to varying flow conditions [30, 31, 69]. As shown by Rojratsirikul *et al.*, performance of these membrane wings can be strongly dominated by the effects of prestrain, elasticity, and excess length [35] – each of these variables can affect the vibrational modes of the membrane under aerodynamic loading, the size of separated flow region, and the conditions under which vortex roll-up is expected. Significant coupling between large-scale flow structures, such as vortex shedding, and the membrane dynamics have been shown by Rojratsirikul *et al.* [34, 35], Gordnier [32], and others. Smith and Shyy [69] introduced two non-dimensional parameters to characterize the elastic-aerodynamic interactions:

$$\Pi_1 = \left( \frac{Eh}{0.5\rho U_\infty^2 c} \right)^{1/3} \quad \text{and} \quad \Pi_2 = \frac{Sh}{0.5\rho U_\infty^2 c},$$

where  $E$  is the membrane's Young's modulus,  $h$ , the membrane thickness,  $\rho$ , the air density and  $S$ , the membrane pretension. Here,  $\Pi_1$  compares the aerodynamic pressure with the elastic tension, while  $\Pi_2$  compares the aerodynamic pressure with the membrane pre-tension. More recently, however, Song *et al.* [31] and Waldman and Breuer [1] proposed a theoretical approach that incorporates both the elastic strain and pretension into a unified description, described by a single Aeroelastic

parameter:

$$Ae = \frac{Eh}{0.5\rho U_\infty^2 c} = \Pi_1^3,$$

which can be balanced with a geometric nondimensional term capturing both prestress and camber-induced tension [1]. Because prestress is not a variable in the current work,  $Ae$  varies only with freestream velocity and will be used throughout.

In addition to direct coupling between the membrane and large-scale flow structures, the dynamics of the membrane wing can also be influenced by fluid structure interactions in the form of flow-induced stiffness and damping terms. These effects are significant when the time scales of the fluid flow and membrane dynamics are comparable, such that the reduced velocity,  $U_R = U_\infty/f_{act}c$ , is of order unity [70]. Though this effect is most commonly discussed in terms of instability excitation, which occurs when flow-induced damping is negative [71], positive damping coefficients may be expected to result in decreased membrane vibration amplitude.

In addition to passive adaptation to flow conditions, membrane wings can be actively controlled. Dielectric elastomer actuators can be used as the wing material, allowing the camber to be controlled by a voltage across the membrane. A flexible electrode is applied on either side of a prestressed dielectric elastomer, and a voltage is applied. Because the membrane is essentially incompressible, the resulting Maxwell's pressure in the out-of-plane direction results in a positive in-plane strain [3]. The in-plane strain generated by the applied voltage results in a decrease in the tension of the wing membrane which, when coupled with an aerodynamic pressure difference, results in indirect control over the wing camber.

The use of dielectric elastomer membranes in an aerodynamic context has been studied primarily by Hays *et al.* [48, 49], Barbu *et al.* [50], and Curet *et al.* [51].

Hays *et al.* applied a DC voltage across a dielectric elastomer membrane wing and demonstrated that significant camber variation can be achieved, as well as an associated increase in the lift coefficient. Barbu *et al.* extended these results, focusing on the effect of membrane prestrain on DC actuation authority under aerodynamic load, finding that a membrane with no prestrain results in the largest change in both camber and lift due to actuation. Interestingly, this is at odds with DEA literature in the absence of aerodynamic load, which has shown improved actuation amplitude for prestrained membranes [9]. The discrepancy could be attributed to the interplay between aerodynamic load and aeroelastic response - the addition of prestress may lead to the membrane performance being dominated by mechanical tension rather than the aerodynamic load. Curet *et al.* extended the actuation modality to include unsteady (AC) actuation of the same type of membrane wing by driving the actuator with a sinusoidal voltage. They showed that, at specific actuation frequencies, a significant increase in lift occurred (with a corresponding increase in drag). However, lacking membrane kinematic data or flow field imaging, definitive conclusions could not be drawn regarding the cause of this increase in lift and drag.

The success of unsteady actuation on aerodynamic performance suggests that there is an interaction between the membrane motion and the flow over the wing that is maximized at particular frequencies. Several possibilities for this interaction exist. Firstly, the optimal frequency might excite a membrane (structural) resonance such that membrane *deflection* increases. Alternatively, the membrane *velocity* might induce a fluid perturbation, analogous to a conventional flow control actuator such as a synthetic jet. As discussed earlier, that unsteady fluid perturbation might have a preferred frequency. Lastly, the optimal response might be some combination of these two.

Exploring and untangling the source of the enhanced aerodynamic performance due to unsteady membrane actuation is the focus of the current chapter. We present wind tunnel measurements taken using a flat, rectangular membrane wing (similar to that used by Curet *et al.* (2014)). Particle image velocimetry (PIV) flow field analysis is combined with 3D time-resolved membrane kinematics to quantify the fluid-structure interactions. Lift and drag data is acquired for both actuated and unactuated wings. The interactions between actuation frequency, freestream velocity, and angle of attack are explored to understand the coupled behavior of the flexible wing membrane and the unsteady flow over a thin wing.

### 3.3 Experimental Methods

The membrane wing consisted of a rigid acrylic frame (180 mm  $\times$  90 mm  $\times$  3.175 mm), with two openings (76 mm  $\times$  76 mm) on either side of the center-line, to which an elastomeric membrane was affixed (Fig 3.1(a)). The membrane was an acrylic elastomer (VHB4905, 3M), biaxially prestrained to 250%, using the apparatus described by Kiser *et al.* [54]. This level of prestrain was chosen based on DEA literature showing improved actuation amplitude with increasing prestrain [9], balanced with decreasing reliability at high prestrains due to excessive thinning of the membrane. Carbon powder electrodes were applied to both top and bottom surfaces, using the membrane’s adhesive properties, with a gap of approximately 3.5 mm between the perimeter of the electrode and the perimeter of the frame. The membrane was attached to the acrylic frame, creating a rectangular membrane wing with full perimeter support. The dielectric membrane actuator was actuated using a high-voltage amplifier (Trek, model 5-80, Lockport, NY) and a sinusoidal input,  $V(t) = V_0(1 + \sin 2\pi f_{act}t)$ . The actuation voltage,  $V_0$ , was kept constant at 2 kV and

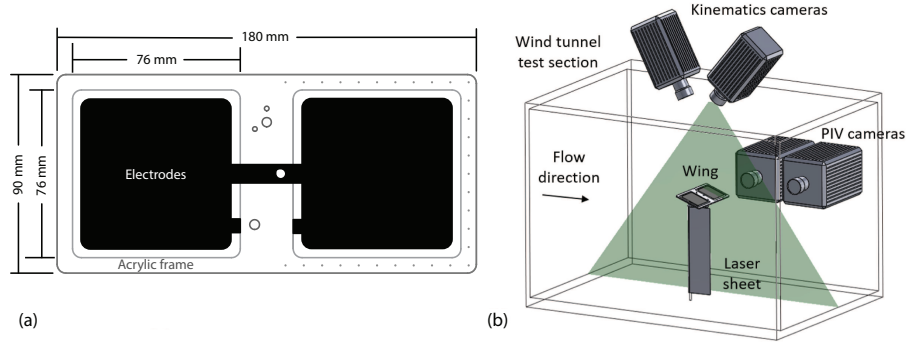


**Figure 3.1:** Experimental set-up showing (a) the top view of the wing and (b) the wind tunnel test section.

the frequency,  $f_{act}$ , ranged from 10 to 300 Hz. The voltage offset serves to eliminate frequency doubling due to the actuation mechanism, which would rectify an unbiased sine wave [54].

The elastic stiffness of a membrane wing has a significant influence on the aerodynamic performance [1]. VHB4905 exhibits significant hyperelastic and viscoelastic qualities [54] and is also strongly temperature dependent [15]. To characterize the elastic modulus, the membrane resonance frequency was measured by sweeping the excitation frequency from 50 to 150 Hz at a rate of 1 Hz per second and measuring the amplitude of the membrane motion without any aerodynamic load. Using this method, the fundamental frequency was established to be 75 Hz for a membrane with 250% prestrain. Assuming linear elasticity, the 2D wave equation gives the fundamental resonance frequency of a square membrane as a function of pre-stretch,  $\lambda$ , and elastic modulus,  $E$ , [72]:

$$f_{11} = \frac{\sqrt{2}}{2L_m} \sqrt{\frac{E(\lambda - 1)}{\rho_m}}, \quad (3.1)$$

where  $L_m$  is the membrane length (76 mm) and  $\rho_m$  is the membrane density (960 kg/m<sup>3</sup>). Solving for  $E$ , we found a Young's modulus of 41.6 kPa. This value was

found to be repeatable, and is consistent with other measurements performed in our laboratory, including a membrane bulge test and uniaxial extension test (results not shown here). Additionally, the result is consistent with the elastic modulus of  $E \sim 35$  kPa found by Michel *et al.* [10], as well as the unstrained Young's modulus of  $E \sim 46$  kPa found by Wang *et al.* [17]. It should be noted that this value is only valid at prestrains and temperatures comparable to those used in this study, as the material is both hyperelastic and viscoelastic. This value of the modulus was used for subsequent calculations throughout.

The wing was tested in a closed-loop wind tunnel (Figure 3.1(b)) at Brown University, with a test section measuring  $0.61 \text{ m} \times 0.61 \text{ m}$  in cross-section and  $2.4 \text{ m}$  in length. The wing was placed approximately in the center of the test section mounted onto a rigid fairing and held at the desired angle of attack with a custom-machined fixture. Freestream velocities ranged from  $5 \text{ m/s}$  to  $25 \text{ m/s}$  and angle of attack was varied from  $10^\circ$  to  $40^\circ$ . The air temperature was maintained to within  $0.1^\circ\text{C}$  of the tare temperature using a water-cooled heat exchanger. A six-axis load cell (F/T Nano17, ATI Industrial Automation, Apex, NC) was positioned at quarter-chord between the angle of attack fixture and the wing and was used to measure the aerodynamic forces and torques with a calibrated uncertainty of  $\pm 0.12 \text{ N}$ . Aerodynamic forces and torques were recorded at  $2 \text{ kHz}$ . For each testing configuration, 20 seconds of data was recorded without actuation, followed immediately by 30 seconds of data collection during membrane actuation.

Membrane kinematics were recorded at  $1000 \text{ fps}$  using two high-speed cameras ( $1024 \text{ pixels} \times 1024 \text{ pixels}$ ) (Photron SA3, Photron Ltd, Tokyo). A  $21 \times 21$  square matrix of marker dots was applied to the membrane surface and used to reconstruct the time-resolved membrane shape using the Direct Linear Transformation (DLT) method [73]. Ten seconds of video data were collected for each experimental condi-

**Table 3.1:** Summary of data collected. Dataset I includes time-resolved and synced PIV, membrane kinematics, and aerodynamic forces and torques. Dataset II includes only forces and torques.

	Velocity (m/s)		Angle of attack ( $^{\circ}$ )		Frequency (Hz)	
	Range	Increment	Range	Increment	Range	Increment
Dataset I	10-20	5	15-30	5	50, 75, 115	N/A
Dataset II	5-25	2	10-40	5	10-300	10

tion. The average reconstruction error was 0.56 mm.

Two additional high-speed cameras (1024 pixels  $\times$  1024 pixels) (Photron SA4, Photron Ltd, Tokyo) were used to capture planar 2D-2C Particle Image Velocimetry (PIV) data at 500 Hz. Nominally 1  $\mu$ m di(2-ethylhexyl)sebacate oil droplets were generated with a Laskin-type nozzle. The particles were illuminated with a laser sheet generated by an Nd:YLF double-pulsed laser (527 nm) (DM30, Photonics Industries, Ronkonkoma, NY), with an energy output of approximately 30 mJ/pulse, operated at 500 Hz double-pulsed. The laser sheet was positioned at approximately quarter-span of the wing, at the center of one of the membrane sections. Each camera had a field of view of approximately 80 mm  $\times$  80 mm, and the two fields of view were stitched together with approximately 15 mm of overlap, such that the flow over the full wing and near wake was captured. Resulting velocity fields have a maximum estimated uncertainty of  $\pm 1.0\%$  of the freestream velocity. PIV measurements were synchronized with the actuation voltage, the measurements of membrane kinematics, and the aerodynamic force/torque data.

Two series of measurements were conducted. In the first series, time-resolved and synchronized PIV, membrane kinematics, and aerodynamic forces and torques were acquired using a membrane under 250% biaxial pre-stretch. A range of freestream velocities, angles of attack, and actuation frequencies (Dataset I, Table 3.1) provided a detailed picture of the flow field and the aerodynamic coefficients, as well as their phase-locked relationship to the membrane motion. The second series of mea-

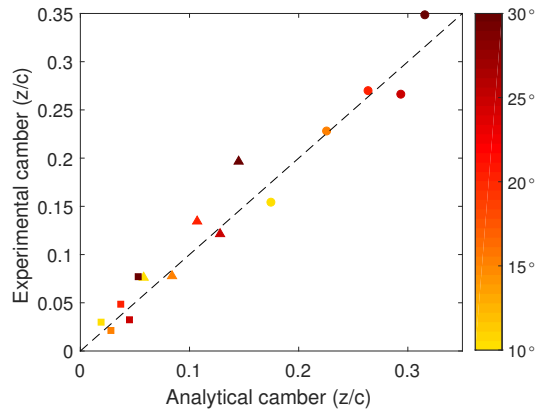


**Figure 3.2:** Comparison of experimental camber with the camber predicted by a potential flow aeroelastic model [1].

measurements recorded only the aerodynamic coefficients, but over a wider range and with a finer resolution of actuation frequencies and freestream velocities (Dataset II, Table 3.1).

## 3.4 Results and Discussion

### 3.4.1 Membrane kinematics

First considering the unactuated membrane wing, the self-cambering behavior is seen to correspond well with expected values. Waldman and Breuer [1] extended the potential flow aeroelastic model developed by Song *et al.* [31], which allows the prediction of camber for extensible membrane wings. Following their model, all unactuated runs from Dataset I (Table 3.1) are shown in Figure 3.2, with angle of attack indicated by color and freestream velocity indicated by symbol shape. The membrane camber is seen to match reasonably well with the predicted camber over the full range of angles of attack and freestream velocities.

When considering the effect of actuation, selection of the actuation frequency may depend on factors including the membrane resonance or the vortex shedding frequency. Matching the actuation frequency with a membrane resonance may allow natural amplification of the effect of actuation. Similarly, matching the actuation frequency with the vortex shedding frequency or the separated shear layer instability frequency may enhance coupling between the membrane and the flow. In studies on passive wing dynamics, lock-in between the vortex shedding frequency and the membrane vibrational modes (either the fundamental or higher harmonic) has been observed at angles of attack in excess of  $15^\circ$ , where bluff-body vortex shedding can generally be expected [1, 34]. However, under the conditions tested here, resonance does not appear to play a significant role in the membrane dynamics. This can be seen from the amplitude response of the membrane when forced over a range of frequencies, both with and without aerodynamic load (Figure 3.3). Without wind, resonant responses are clearly seen at approximately 75 and 115 Hz (Figure 3.3, black line). However, the amplitude of membrane vibration does not appear to vary with actuation frequency when the wing is under aerodynamic load. At 10 m/s freestream velocity (Figure 3.3, blue line), the mean camber increases due to the aerodynamic load and a small increase ( $\sim 2\%$ ) in vibration amplitude is seen from approximately 80-110 Hz. At 15 m/s freestream velocity (Figure 3.3, red line), the average camber further increases, again due to the mean aerodynamic load, but now no discernible variation in vibration amplitude is seen as the frequency changes. It should be noted that the resonance frequency would be expected to increase modestly ( $< 5$  Hz) due to camber-induced tensioning. However, the lack of any visible resonance under aerodynamic loading is likely due to fluid-induced damping, which becomes significant when the characteristic timescales of the fluid and membrane are comparable, and will be discussed in more detail in Section 3.4.4.

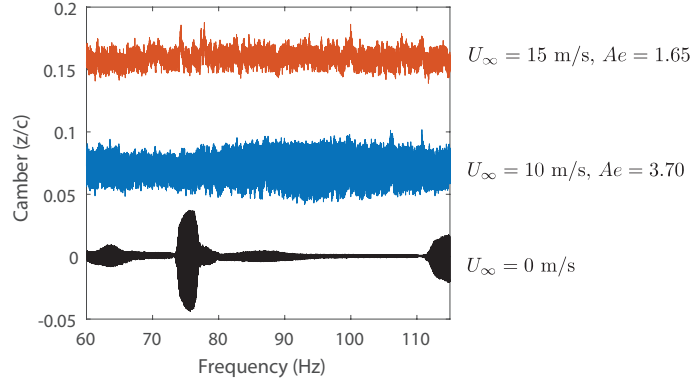


**Figure 3.3:** The time-series amplitude of membrane vibration is shown as a function of actuation frequency under three loading conditions, while actuation frequency is swept at a rate of 1 Hz per second.

In Figure 3.4, the spatial structure of the membrane subject to actuation at  $f_{act} = 115$  Hz is shown, for a wing at  $\alpha = 25^\circ$  and  $U_\infty = 10$  m/s. Both the mean (a,b), and the rms (c,d) camber are shown. The mean camber is roughly symmetric around the center of the membrane, regardless of whether the membrane is being actuated. Though the shape of the membrane does not change significantly, the mean amplitude increases with actuation from 12.3% to 17.1%. This increase in mean camber is likely driven primarily by the 2 kV DC component of the actuation voltage. The effect of DC voltage on aerodynamic performance has been studied elsewhere (e.g., Barbu *et al.* [50]), and will not be further addressed in this work. The unsteadiness in the membrane motion increases dramatically due to actuation, with the standard deviation doubling from 0.6% to 1.2%. This unsteadiness is primarily in the fundamental vibration mode, with the peak membrane velocities located near the center of the wing. The (1 – 1) vibration mode was observed to be dominant for all actuation frequencies, and for this reason, all future descriptions of the membrane kinematics refer solely to the peak camber.

The phase-averaged peak camber measured at three wind speeds is shown in Figure 3.5. The actuated camber is compared with the camber for the unactuated

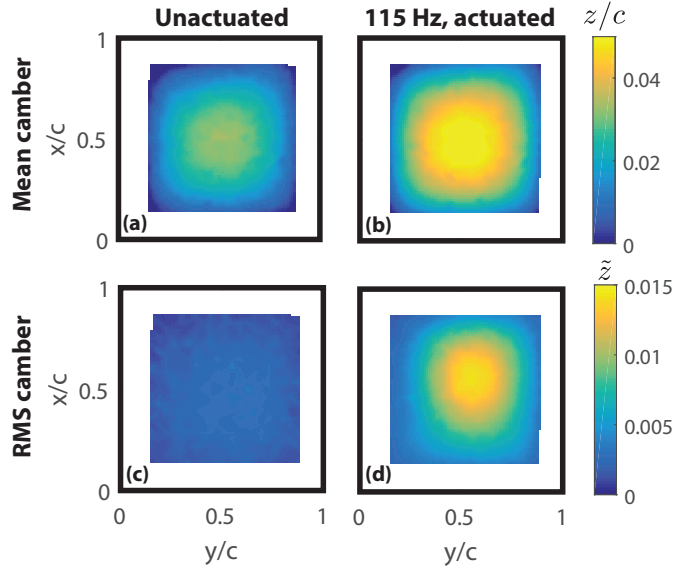


**Figure 3.4:** Mean (a, b) and RMS (c, d) camber for a wing at  $25^\circ$ , 10 m/s, and 115 Hz actuation is shown.

wing. At the lowest speed (10 m/s,  $Ae = 3.7$ ), the unactuated wing achieves a camber of 3.4%, with a very low standard deviation (0.25%). When actuation is applied under these conditions, a strong phase-averaged cyclic behavior is seen, with the peak camber varying from 3.9% to 7.2% over the period of actuation. Similar behavior is seen at the intermediate speed (15 m/s,  $Ae = 1.6$ ), with the phase-averaged camber varying from 15.9% to 18.6%, while the unactuated membrane camber achieves a lower mean camber (12%) and exhibits a standard deviation of only 0.6%. However, a distinct decrease in actuation authority is seen at the highest velocity (20 m/s,  $Ae = 0.9$ ). Though the mean camber increases significantly, there is much less phase-locked motion. This was seen throughout the range of angles of attack and actuation frequencies that were tested - at high freestream velocities (low  $Ae$ ), actuation consistently had a much weaker effect on the phase-averaged camber variation. Several factors may play a role in this loss of actuation authority.

Mechanically, several factors influence the expected level of actuation author-

ity. As the aeroelastic number decreases with higher freestream velocities, the mean camber is increased and the membrane requires more energy to deform. However, this is counteracted by the improved performance of DEAs under increasing prestrain [9]. As the membrane experiences additional strain due to camber, the membrane becomes thinner, resulting in a quadratically increasing electric field between the electrodes on the upper and lower surfaces. Ultimately, the effects of the increased energy requirement would be significantly mitigated, if not overcome, by the increased electric field, particularly at the modest ratios of camber-induced strain to membrane prestrain that are seen in this work.

One possibility is that high cambers were accompanied by increased electrode resistance, due to strain in the membrane surface. As the membrane strains, the carbon powder particles are pulled further apart, resulting in increased resistance and decreased actuation amplitude. As measured by Carpi *et al.* [18], the degree to which strain affects resistivity is strongly dependent on the electrode material. However, additional testing with carbon grease electrodes, which are much less sensitive to strain, displayed no change in performance at high cambers (not shown), suggesting that loss of conductivity is not the primary problem. Another possibility is that as the freestream velocity increases, the reduced frequency,  $f_{act}c/U_\infty$ , decreases, which may be associated with decreased membrane response. But, as will be discussed in Section 3.4.2, this effect does not explain the loss of actuation authority at high freestream velocities. We believe that the phenomenon is most consistent with fluid-induced damping effects, which will be discussed in more detail in Section 3.4.4.

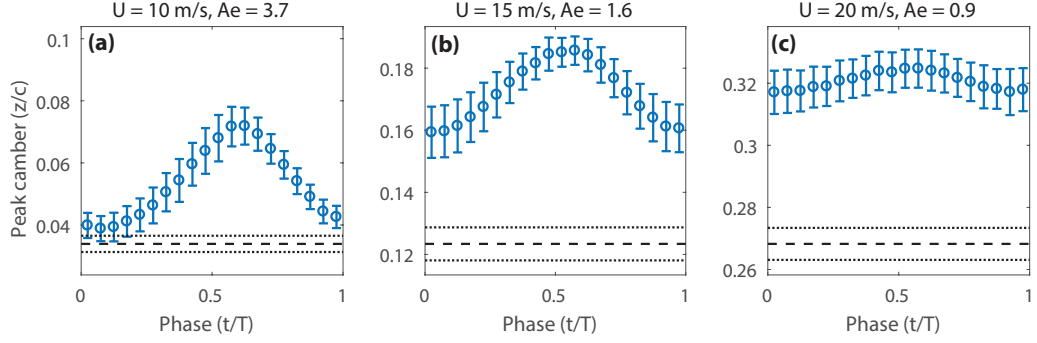


**Figure 3.5:** Phase averaged kinematics are shown for a wing at  $25^\circ$ , actuated at 115 Hz under 10 (a), 15 (b), and 20 (c) m/s freestream velocities. Camber of an unactuated wing under the same aerodynamic conditions is shown in black.

### 3.4.2 Effect of actuation on aerodynamic performance

Given the effect of actuation on the membrane shape, one would expect to see an associated change in the aerodynamic performance of the wing. The time response of the coefficient of lift,  $C_L$ , is shown in Figure 3.6. When the actuation voltage is applied, the effect on the aerodynamic performance is seen nearly instantaneously. At 10 m/s (Figure 3.6a), the mean lift coefficient is seen to increase from 0.81 to 1.07 due to actuation. The lift increment is less pronounced at 15 m/s (Figure 3.6c), and at 20 m/s (Figure 3.6e), the change in mean lift coefficient is negligible, remaining at 1.0 with or without actuation.

As we saw with the membrane kinematics (Fig. 3.5), there is a significant phased-locked variation in the lift signature (Fig. 3.6b,d,f). As with the camber measurements, the effect of actuation becomes weaker as the velocity increases ( $Ae$  decreases). The phase of maximum lift closely corresponds with the phase at which the membrane is at maximum camber, suggesting that the improved aerodynamic performance is directly related to the displacement of the membrane.

In addition to the effect of the aeroelastic number,  $Ae$ , lift enhancement is also

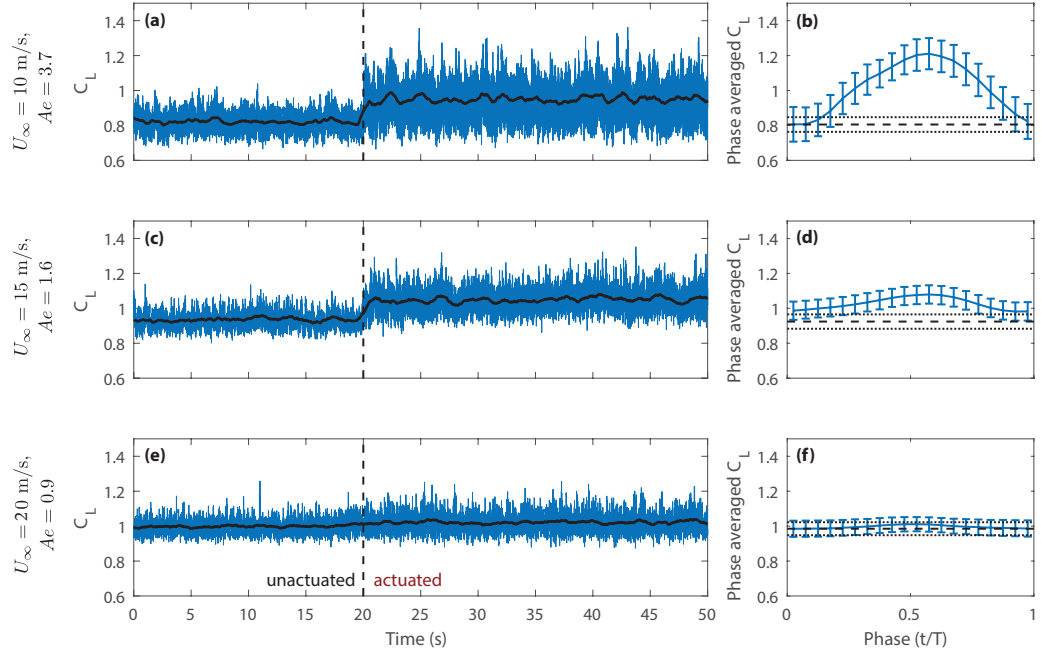


**Figure 3.6:** The coefficient of lift for a wing at  $25^\circ$ , actuated at 115 Hz, is shown as a function of time (a, c, e) and phase (b, d, f) for 10 m/s (a, b), 15 m/s (c, d), and 20 m/s (e, f) freestream velocities.

a function of reduced frequency,  $f^+ = f_{act}c/U_\infty$ , as shown in Figure 3.7 for several angles of attack and freestream velocities. As suggested by Figure 3.3, the mean camber is unaffected by actuation frequency, such that only camber unsteadiness is varying as a function of reduced frequency. Angle of attack and freestream velocity are seen to have some effect, such that a wing at  $25^\circ$  exhibits a broader range of optimal reduced frequencies relative to a wing at  $30^\circ$ , and the amplitude of lift enhancement is generally higher for lower freestream velocities (as addressed in Section 3.4.4). Despite these differences, the scaling of lift enhancement with reduced frequency remains fairly consistent, resulting in optimum lift enhancement between reduced frequencies of 0.5 – 1, which is consistent with the optimal performance regime of synthetic jets being operated at  $f^+ \sim \mathcal{O}(1)$  [44]. The flow physics behind this dependency on  $f^+$  will be discussed further in Section 3.4.5.

Significant lift enhancement due to membrane actuation is observed over a range

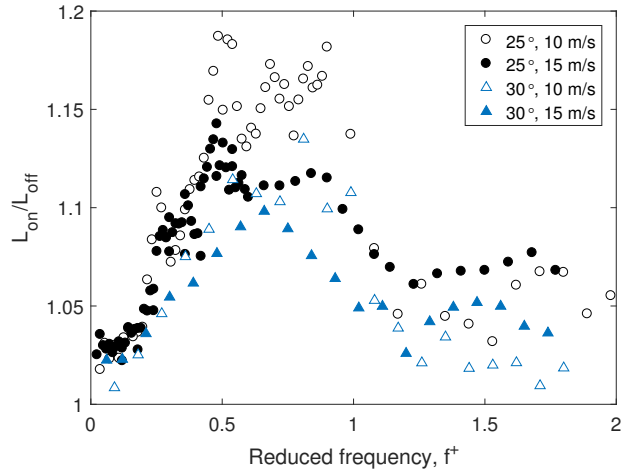


**Figure 3.7:** The effect of reduced frequency on lift enhancement is shown for wings at 25°-30° angle of attack and 10-15 m/s freestream velocity.

of angles of attack, freestream velocities, and actuation frequencies (Figure 3.8). From actuation frequencies from 50 Hz to 115 Hz, lift enhancement is consistently seen in the velocity range of  $U_\infty = 7$  m/s ( $Ae = 7.6$ ) to  $U_\infty = 15$  m/s ( $Ae = 1.6$ ) and over angles of attack,  $\alpha$ , between 15° and 30°. While the location of peak performance is at the same combination of velocity and angle of attack for all three actuation frequencies, the magnitude of lift enhancement is seen to increase with actuation frequency, suggesting that reduced frequency also plays a role in flow control efficiency. Note that the reduced frequency at 115 Hz and 10 m/s (the peak of Figure 3.8c) is 1.03, which is near the peak performance expected based on Figure 3.7.

However, reduced frequency does not provide a complete explanation of lift enhancement, as the performance peak occurs at a constant freestream velocity, rather than a constant reduced frequency. Just as is seen in the “traditional” synthetic jet literature (e.g. [44]), flow control effectiveness is tied to both reduced frequency and the magnitude of momentum injection. As discussed in Section 3.4.1, higher freestream velocity is associated with decreased membrane vibration, which signif-

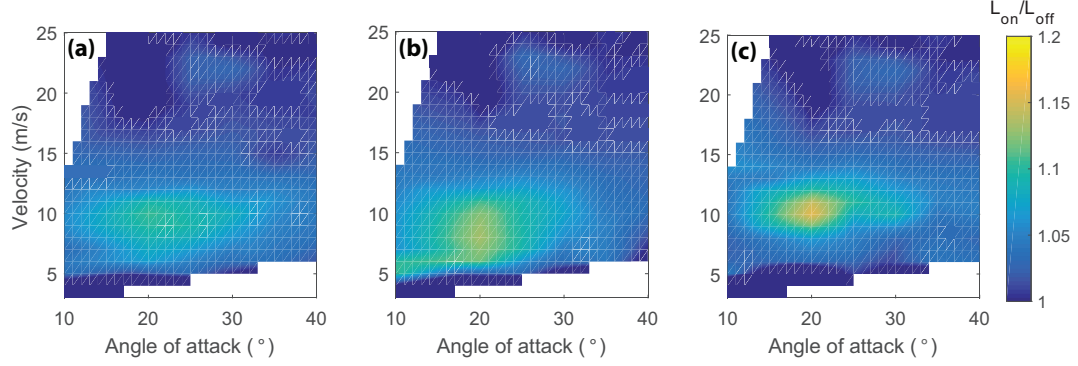


**Figure 3.8:** Lift enhancement is shown as a function of angle of attack and freestream velocity for a wing being actuated at (a) 50 Hz, (b) 75 Hz, and (c) 115 Hz.

icantly lowers the amount of momentum injected into the surrounding flow. The effect of actuation amplitude on flow control effectiveness can be seen in Figure 3.9, and will be explored in the following section.

### 3.4.3 Actuation amplitude dependency

The link between actuation amplitude and flow control effectiveness can be seen by plotting the lift enhancement vs. the coefficient of momentum (Figure 3.9). The coefficient of momentum ( $C_\mu$ ) is a convenient way to quantify the effect of membrane motion in a way analogous to the performance of synthetic jets. However, in this case the momentum is generated by the motion of the entire lifting surface, not just from a concentrated unsteady jet. For this application we define the coefficient of momentum in terms of the integrated membrane velocity:

$$\langle C_\mu \rangle = \frac{\rho \iint \langle u(x, y)^2 \rangle dx dy}{\frac{1}{2} \rho U_\infty^2 c^2}, \quad (3.2)$$

where  $\langle u(x, y)^2 \rangle$  is the RMS value of the locally measured velocity of the membrane,  $x$  and  $y$  are the in-plane coordinates of the membrane, and  $c$  is the wing chord. Using this definition we see that experimental conditions that lead to high values

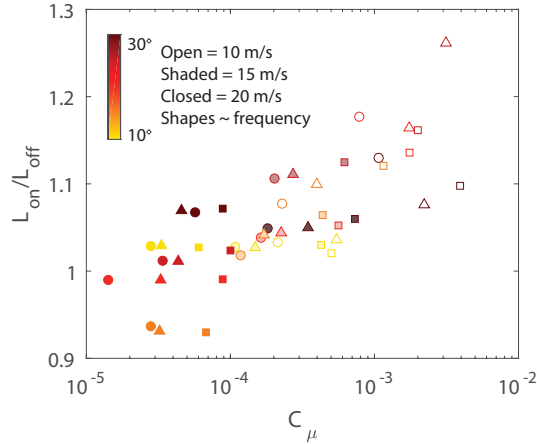


**Figure 3.9:** The effect of actuation on lift enhancement is shown as a function of coefficient of momentum,  $C_\mu$ , for parameters ranging from 15-30° angle of attack, 10-20 m/s freestream velocity, and 50-115 Hz actuation frequency.

of  $C_\mu$  are correlated with large enhancements of lift, and that lower improvements tend to be associated with higher freestream velocities where, as we have seen, the membrane motion is less dramatic.

### 3.4.4 Fluid-induced damping

Fluid-induced damping is a natural consequence of an unsteady fluid-structure interaction, and associated with either viscous drag induced by the structural motion or energy radiated from the structure in the form of acoustic energy or vortex shedding. We can estimate the effect of fluid-induced stiffness and damping on the wing using a simple aeroelastic analysis. Following the approach of Païdoussis *et al.* [70], we consider a membrane subject to a harmonic amplitude variation,  $z$ , expressed using complex notation as

$$z(t) = \tilde{z}e^{j\omega t}.$$

The fluid-induced stiffness,  $k$ , depends on the reduced frequency,  $f^+$ , and the relationship between the normal force coefficient,  $C_N$ , and the membrane deformation,

$\tilde{z}$ :

$$k = \frac{1}{2} \frac{m^*}{f^{+2}} \frac{\partial C_N}{\partial \tilde{z}}, \quad (3.3)$$

where  $m^*$  is the mass ratio:

$$m^* = \frac{\rho S c^2 \sin(\alpha)}{m}, \quad (3.4)$$

( $\rho$  is the fluid density, and  $m$  is the membrane mass). The normal force coefficient,  $C_N$ , is defined as:

$$C_N = \frac{F_N}{0.5 \rho U_\infty^2 c S}. \quad (3.5)$$

For our experiments,  $m^*$  ranges from 0.68 ( $\alpha = 10^\circ$ ) to 1.98 ( $\alpha = 30^\circ$ ). Similarly, the fluid-induced damping,  $b$ , is a function of the mass ratio, the reduced frequency, and the dependency of the normal force coefficient on the vibration velocity,  $f^+ \tilde{z}$ :

$$b = \frac{1}{2} \frac{m^*}{f^{+2}} \frac{\partial C_N}{\partial (f^+ \tilde{z})}. \quad (3.6)$$

To estimate  $k$  and  $b$ , the effects of the membrane motion on the coefficient of normal force must be estimated. To do this, we compute the relationship between the amplitude of phase-averaged  $C_N$  and the membrane deflection,  $\tilde{z}$ , and velocity,  $f^+ \tilde{z}$ , shown respectively in Figure 3.10(a-b) for all conditions tested in Dataset I. Although the data shows scatter, a reasonably good linear correlation is achieved, with slopes of 4.58 and 0.46, respectively.

With these coefficients in hand, the expected amplitude of membrane motion can be estimated by treating the wing membrane as a forced harmonic oscillator [74]:

$$\frac{d^2 z}{dt^2} + 2\zeta\omega_0 \frac{dz}{dt} + \omega_0^2 z = F e^{j\omega t}, \quad (3.7)$$

where  $\omega_0$  is the natural frequency of the oscillator ( $\sqrt{k/m}$ ),  $\zeta$  is the damping ratio

$(b/2\sqrt{mk})$ , and  $F e^{j\omega t}$  is the complex driving force of the oscillator. Solving for the complex displacement, we find that

$$z = \frac{1}{j\omega b + j(\omega m - k/\omega)} F e^{j\omega t} = \frac{1}{j\omega} \frac{F e^{j\omega t}}{Z_m}, \quad (3.8)$$

where  $Z_m$  is the complex mechanical impedance. The amplitude of the displacement is given by the magnitude of the real part of Equation 3.8:

$$\tilde{z} = \frac{F}{\omega Z_m}. \quad (3.9)$$

Calculating  $Z_m$  from the stiffness and damping coefficients derived from Figure 3.10(a-b) and using an arbitrary value of  $F$  as a fitting parameter, the expected amplitude of motion can be estimated and compared to the actual amplitude of camber variation during actuation, as shown in Figure 3.10(c). Though significant scatter is seen, the experimental phase-averaged camber variation is seen to follow the same trend as the vibration amplitude predicted by this simple theoretical model. The comparison is limited by the rough nature of the  $k$  and  $b$  estimates, which are certainly dependent on other parameters, most notably the reduced frequency. Indeed, the linear regression,  $R^2$ , values of each fit in Figure 3.10 range between 0.43 and 0.74, suggesting that the dynamics are not fully captured by fluid-induced loading. However, the trend of reduced actuation performance at high freestream velocities is consistent with fluid-induced loading and is an encouraging result that helps us to understand the overall behavior of the system.

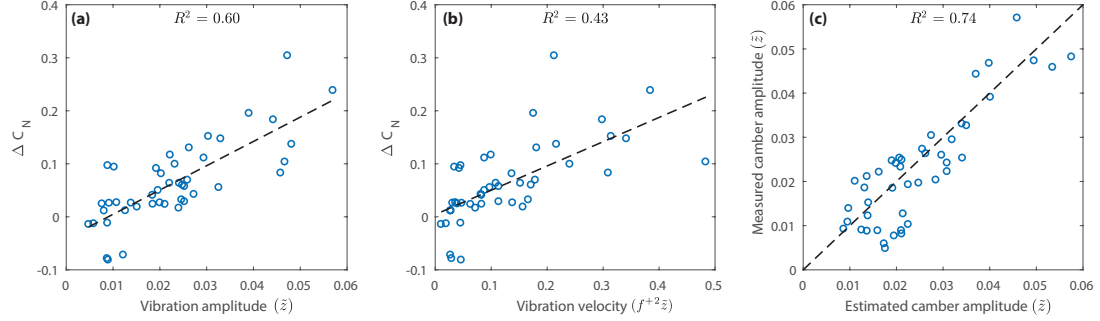


**Figure 3.10:** The relationship between (a) mode amplitude and change in normal force coefficient and (b) mode velocity and change in normal force coefficient is shown. (c) The resulting predicted amplitude of vibration is compared with the measured camber amplitude.

### 3.4.5 Actuated velocity fields

The effect of actuation on the time-averaged velocity field is shown in Figure 3.11 for a range of angles of attack and at a constant freestream velocity of 10 m/s. A small separation bubble is present for  $\alpha = 10^\circ$ , and the mean flow field under actuation is seen to be unchanged (Figure 3.11a,b). However, as the angle of attack increases to  $20^\circ$ , a larger separation bubble forms over the unactuated wing while actuation significantly reduces the size of this separation bubble, which is pulled closer to the membrane (Figure 3.11c,d). As seen in Figure 3.8, this configuration is one of the most effective for flow control, with lift enhancement on the order of 20%. Finally, as the angle of attack is increased to  $30^\circ$ , the mean flow is seen to be massively separated. The effect of actuation on the mean flow field is more subtle in this scenario, with a modest change to the position of the separated shear layer (Fig. 3.11d,e). Though this scenario also produces some lift enhancement, the effect is much smaller than that observed when the wing is at  $20^\circ$  angle of attack (Figure 3.8).

In Figure 3.12a, the time-averaged unactuated flow field at  $20^\circ$  and 10 m/s is shown, with the location of the separation shear layers for the unactuated (solid black line) and the actuated flow (dotted white line) superimposed. The shear layer

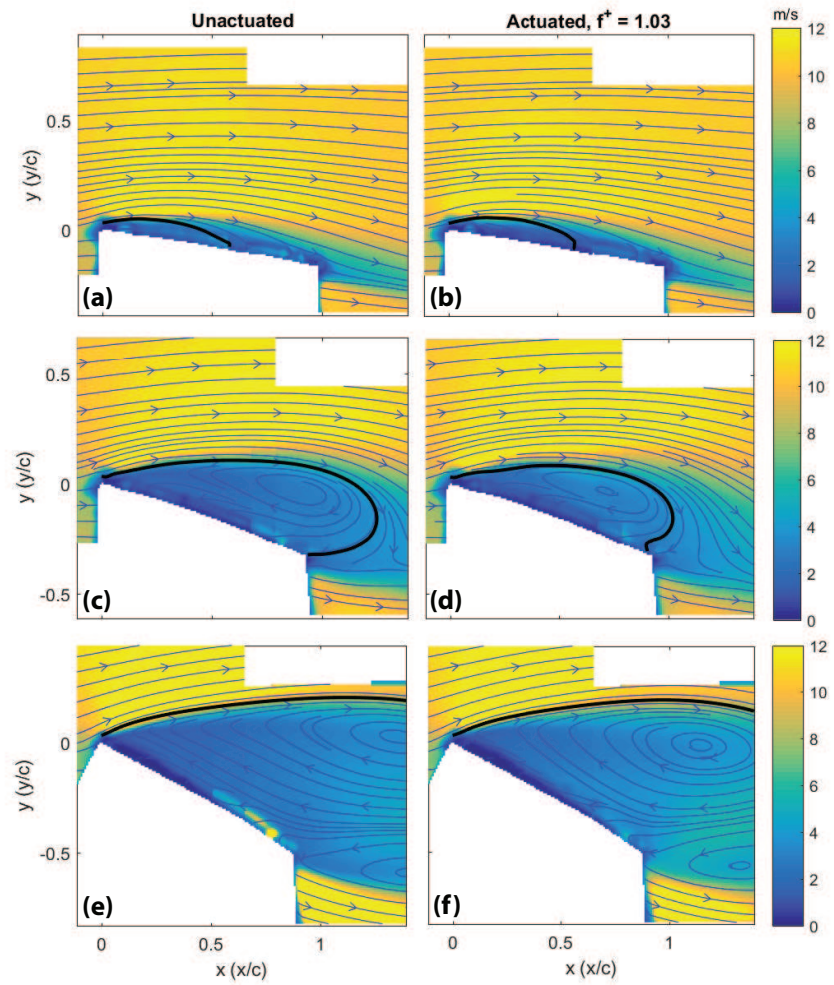


**Figure 3.11:** Mean velocity magnitude and streamlines for unactuated wings (a, c, e) and wings actuated at 115 Hz (b, d, f) at 10 m/s freestream velocity and  $10^\circ$  (a, b),  $20^\circ$  (c, d), and  $30^\circ$  (e, f) angle of attack.

location is (arbitrarily) defined as the streamline passing through a point two millimeters above the leading edge of the wing, and we see the strong reduction of the separated flow region that is achieved by the actuated membrane motion. In Figure 3.12b, this result is generalized for several angles of attack, and the location of the separation streamlines are shown for all unactuated flows from  $10^\circ$  to  $30^\circ$  (solid lines) with the corresponding streamlines for flows with actuation (115 Hz, dashed lines). The size of the separation bubble is significantly affected by membrane actuation for flows at intermediate angles of attack between  $15^\circ$  and  $25^\circ$ . At  $10^\circ$ , the separation is minimal, and actuation has little or no effect on the separation streamline. At  $30^\circ$ , the flow is massively separated and the separation streamline has moved far from the surface of the wing. In this case, the effect of actuation on the separation streamline is also minimal, presumably because the shear layer is too far from the surface of the wing to be effectively controlled. However, the effect of actuation on the streamline location may be greater than is suggested here. Because the separation streamline leaves the field of view for our measurements, the effect of actuation downstream of the wing is unknown. Despite the difficulty in visualizing the full separation streamline at high angles of attack, it can be noted that the center of the separated streamlines is significantly closer to the wing surface in Figure 3.11f as compared to the unactuated wing in Figure 3.11e, and that a lift enhancement of more than 10% can be seen in Figures 3.7 and 3.8 for these experimental conditions.

In the context of a separated flow, such as those shown in Figure 3.11(c-f), two unsteady mechanisms may be present: the separated shear layer instability and the global bluff-body vortex shedding instability [37]. The characteristic frequencies of both of these should be considered, as either has the potential to control the system behavior, resulting in interactions between membrane dynamics and flow structures.

The frequency of bluff body shedding is typically defined by a modified Strouhal

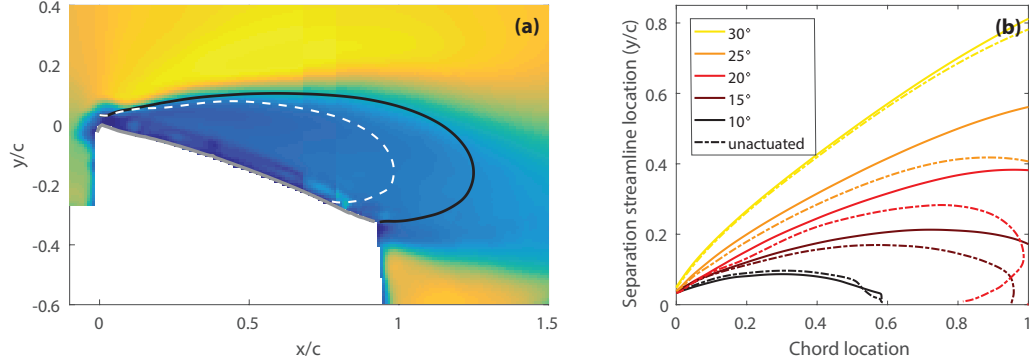


**Figure 3.12:** (a) A time-averaged flow field at  $20^\circ$  and  $10$  m/s freestream velocity is shown, with the separation streamline of an unactuated wing (black solid) and a  $115$  Hz actuated wing (white dashed) shown. (b) The relative location of the separation streamlines for unactuated wings (solid lines) and actuated wings (dashed lines) for a range of angles of attack from  $10^\circ$  to  $30^\circ$ , with  $115$  Hz actuation and  $10$  m/s freestream velocity.

number based on the projected area of the wing:

$$St_m = fc \sin(\alpha)/U_\infty,$$

where  $St_m$  has been empirically shown to remain fairly constant between  $0.15$  and  $0.2$  for a wide range of experimental conditions [34]. Here, a Strouhal number of  $0.15$  would result in bluff-body vortex shedding frequencies ranging from  $33$  Hz ( $U_\infty = 10$  m/s,  $\alpha = 30^\circ$ ) to  $192$  Hz ( $U_\infty = 20$  m/s,  $\alpha = 10^\circ$ ). However, these frequencies are only relevant for configurations in which bluff-body vortex shedding is expected, which generally requires fully separated flow. Vortex shedding is unlikely at angles of attack below  $15^\circ$ .

The local shear layer instability frequency is also important to consider, as it may interact with the membrane kinematics and the bluff body shedding (if present). The shear layer instability frequency,  $f_{SL}$ , can be defined as [37]:

$$f_{SL} = \frac{St_{SL}U_\infty}{2\theta}, \quad (3.10)$$

where  $St_{SL}$  is empirically determined to be roughly  $0.034$  for a laminar flow and

between  $0.044 - 0.048$  for a turbulent flow [75]. The momentum thickness of the separated shear layer,  $\theta$ , was estimated by integrating the PIV data at  $0.5c$  from the surface of the membrane to the upper extent of the PIV field of view, where freestream velocity had been achieved. Using this approach we find that  $\theta$  ranges between 2-5 mm, depending on the angle of attack and, to a lesser extent, freestream velocity (not shown). Combining this result with the freestream velocity and a nominal value of the characteristic Strouhal number,  $St_{SL} = 0.046$  [75], we estimate that the shear layer instability frequencies lie in the range of 60 to 215 Hz. This range is comparable to the leading edge vortex shedding frequencies that may be expected.

The potential interaction between the shear layer instability frequency and the global bluff-body shedding frequency can be considered by computing spectrograms of the streamwise velocity in the near wake. Power spectra are computed from the time-resolved PIV data, evaluated at a vertical cross-section of the wake that is located  $0.5c$  downstream of the wing's trailing edge, with  $y = 0$  corresponding to the leading edge. The frequency content of the wake behind the unactuated wing (Figure 3.13a) is compared with the frequency content of wakes resulting from actuation at reduced frequencies of  $f^+ = 0.45, 0.68, \text{ and } 1.03$  ( $f_{act} = 50, 75 \text{ and } 115$  Hz respectively) (Figure 3.13b,c,d).

Considering the frequency content in the near wake of the unactuated wing, very little energy is seen in the range of Strouhal numbers expected to be related to bluff body shedding ( $0.15 < St < 0.2$ ), suggesting that vortex shedding is relatively weak at this Reynolds number (120,000). Actuation at 50 Hz ( $f^+ = 0.45$ ) is seen to add a visible peak at  $f_{act}$  (white dotted line), as well as a very strong response at the subharmonic, 25 Hz. As the actuation frequency is increased in Figure 3.13c-d, additional energy (relative to the unactuated wing) remains visible at both the

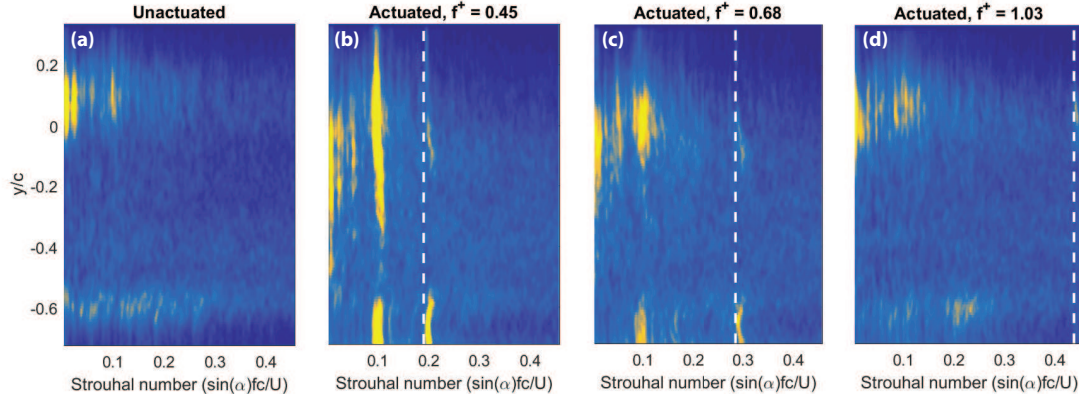


**Figure 3.13:** Spectra showing the frequency content of a wing at  $25^\circ$  and 10 m/s, for an (a) unactuated wing, as well as wings actuated at (b) 50 Hz, (c) 75 Hz, and (d) 115 Hz.

actuation frequency, as well as relatively broadband energy at a modified Strouhal number of roughly 0.1. Though this is a lower Strouhal number than expected, the addition of energy at a constant Strouhal number during actuation does suggest that the membrane actuation may be feeding the vortex shedding instability.

Because flow control via unsteady actuation relies on the excitation of one or both of the described instabilities, the frequency of actuation plays a significant role in successfully enhancing lift, as previously shown in Figure 3.7. The physical cause of this optimum range of actuation frequencies can be seen using Dynamic Mode Decomposition [76], which decomposes the time-resolved velocity data into modes, each of which has a single characteristic frequency of oscillation. The eigenvalue analysis acts to approximate a linear operator that best captures the dynamics of the flow [77]. In Figure 3.14, modes are calculated from the vorticity field in the region immediately behind the leading edge of the wing, and the mode corresponding to the frequency of actuation is selected for examination. A variety of  $Ae$  and  $f^+$  values are shown, with (a-c) showing modes with  $U_\infty = 10$  m/s,  $Ae = 3.7$  and (d-f) showing  $U_\infty = 15$  m/s,  $Ae = 1.6$ , at reduced frequencies ranging from 0.114 to 1.348. It is seen that at low reduced frequencies, where lift enhancement is negligible, there are no coherent structures associated with the the actuation frequency

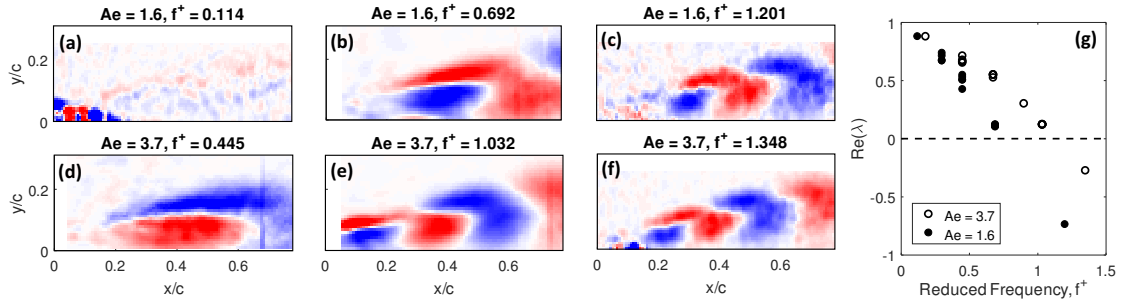


**Figure 3.14:** The DMD mode at the frequency of actuation is shown for the region immediately behind the leading edge of the wing for a range of  $Ae$  and  $f^+$  conditions (a-f). Additionally, the eigenvalue of these modes is shown in (g).

(Figure 3.14a). However, as the reduced frequency increases, lift enhancement is observed, and coherent vortical structures are seen in the region of the separated shear layer (Figure 3.14b,d,e). At a reduced frequency of 0.445, only a single pair of vortices are seen over the chord of the wing, and as the reduced frequency increases further, the vortices become more closely packed. Finally, as the reduced frequency is increased to 1.201 and 1.348, DMD continues to identify vortices in the shear layer, though lift enhancement is very small. Because DMD is an eigenvalue analysis, the real value of the mode's eigenvalue can be used to estimate the mode's growth factor. Considering the growth factor as a function of reduced frequency (Figure 3.14g), it is seen that the growth factor becomes negative at these high reduced frequencies, indicating that the vortices seen in the high reduced frequency mode, while coherent, are damped and do not grow in time.

### 3.5 Conclusions

The use of compliant membrane wings has several appealing features both in terms of aerodynamic properties - enhanced lift slope and increased stall margin - as well as several operational features including foldability and low mass. Here we have demon-

strated control of the aerodynamic properties of these wings, using the electroactive material properties of specific membrane materials. Initial results are promising, resulting in lift enhancement of up to 20%.

Successful lift enhancement by manipulating the separating shear layer has been shown to be associated with instabilities in the separated flow, requiring excitation within a range of susceptible reduced frequencies, generally on the order of  $f^+ = 1$ . The shear layer must be separated and located sufficiently near the membrane to be affected by the actuation. Additionally, the excitation of instabilities is impossible when the actuation mechanism is insufficient to overcome the fluid-induced damping of the membrane. Therefore, flow control using a membrane wing requires careful attention to both  $f^+$  and  $Ae$  for optimal performance.

Additional research is required to optimize the effectiveness of this flow control technique for membrane wings. For example, increasing the amplitude of actuation would be a step towards mitigating the flow-induced stiffness and damping issues, and could be accomplished in several ways. VHB is known to be highly viscoelastic, so the selection of silicone-based membranes, which have been shown to have lower viscoelastic losses [10] would likely improve performance, particularly at high actuation frequencies. Increasing the prestretch of the membrane has also been shown to increase actuation amplitude [3], although it is unclear if, coupled with aerodynamic load, this would also result in increased camber control [50]. Improving the conductivity of the electrodes may also have a positive effect of actuation, particularly at high cambers. Yet despite the sub-optimal design presented here, peak lift enhancements on the order of 20% were observed over a range of experimental parameters - expanding this range is a topic for future research. Additionally, optimization of the wing design may further improve performance. The membrane only accounts for 72% of the surface area in the current design. Increasing that ratio by using a

stiffer and thinner frame may improve performance, particularly at high freestream velocities. Finally, investigation of a range of membrane prestrain values may allow for greater control authority. While high prestrains generally result in high actuation authority for DEAs without aerodynamic load, the results of Barbu *et al.* suggest that the addition of aerodynamic load may lower the optimum prestrain value for actuation authority.

Extension of the experimental techniques used may also provide additional clarity on the mechanism of flow control. The low aspect ratio wing used in this study likely has a significant three-dimensional flow, including a tip vortex. Details of this flow, and the effects of actuation would be captured with more PIV planes across the span and with three-component (stereo or tomographic) PIV. Such data would be especially helpful in clarifying the effect of actuation on the spanwise location and size and shape of the separation bubble at high angles of attack, both with and without actuation.

The development of active flow control techniques for membrane wings will become increasingly important with the ongoing development of micro air vehicles (MAVs). Integrated active flow control, as demonstrated here with dielectric elastomer actuator membranes, will enable MAVs to operate in a wider range of flow conditions, respond to flow unsteadiness, and improve maneuverability.

## Acknowledgements

This research was supported by the U.S. Army Natick Soldier Research, Development and Engineering Center's AH52 basic research and Aerial Delivery Directorate,

Airdrop Research Technology programs. JB was supported by the Naval Undersea Warfare Center, Division Newport.

# CHAPTER FOUR

---

## Capacitive deformation sensing with DEA membranes

## 4.1 Abstract

The use of dielectric elastomers as integrated actuators and self-sensors offers a simple approach for closed-loop control in a wide range of applications. While a number of approaches for self-sensing have been proposed, the adaptive online algorithm offers an appealing combination of high accuracy and low computational cost. In this work, the recursive least squares algorithm will be applied to capacitive deformation sensing of dielectric elastomers. With the goal of minimizing data volume while achieving a set accuracy over a desired range of deformation frequencies, the probe frequency, sampling frequency, and forgetting factor will be optimized. It will be shown that the accuracy is primarily determined by a nondimensionalized variable,  $N_c$ , which defines the proportion of a hypothetical deformation cycle that is weighted more heavily by the algorithm. Ultimately, this optimized algorithm will be validated by variably inflating a dielectric elastomer membrane and comparing the algorithm output to membrane deformation measured by video.

## 4.2 Introduction

The use of dielectric elastomers as integrated self-sensors was first proposed by Sommer-Larson *et al.* [20], who noted that changing the geometry of dielectric elastomer actuators would result in varying electrical quantities, which could be exploited to indirectly measure the strain of the elastomer itself. Though the method proposed by Sommer-Larson *et al.*, involving the measurement of harmonics in the electrical current, has since been replaced by more precise and robust methods based on treating the dielectric elastomer as part of an electrical circuit, the suggestion of self-sensing has inspired a field of research that enables closed-loop integrated con-

trol and sensing for a variety of applications, from soft robotics [22] to reconfigurable keyboards [28].

Ultimately, self-sensing relies on the treatment of a dielectric elastomer actuator (DEA) as part of an electrical circuit, linking the changing electrical properties with changing mechanical configuration. A DEA consists of an elastomer membrane sandwiched between two compliant electrodes, which may be modeled as an equivalent electrical circuit. This model generally involves three components: the membrane and electrodes are treated as a variable capacitor, which is in series with a variable resistor (due to the resistive nature of the compliant electrodes), and in parallel with an additional resistor to account for any leakage current across the dielectric material [78]. Most models neglect the leakage current as negligible, allowing the DEA to be treated as a simple series RC circuit [25].

In general, the resistance of the compliant electrodes is known to be a function of strain [21]. However, age of the electrode material, variations in fabrication technique, and creep in the elastomer itself can complicate that relationship. Though variable resistance has been used to measure membrane strain with some success [24], it may also be used as a secondary measurement to track actuator health [79].

Most commonly, the variable capacitance of the elastomer is used as the primary sensing variable. As the elastomer is strained, the incompressible nature of the material requires that the membrane thickness decreases, thus increasing the capacitance. A number of methods have been developed to track the changing capacitance. For example, the use of an external resistor in series with the membrane creates a high-pass circuit, which may be used to measure capacitance, as demonstrated by Jung *et al.* [23] and others. However, this method neglects the variable resistance of the compliant electrodes, and is only valid for the range of capacitance (and membrane

stretch) values that result in a measurable change in capacitive reactance.

Another approach, developed by Gisby *et al.* [78], uses the amplitude and duty cycle of a pulse width modulation signal to approach a stable constant charge system. Though this method was successful in establishing real-time closed loop control of DEA arrays, it requires the system to be current-controlled, rather than the more common voltage control.

Perhaps the most complete model, simultaneously accounting for variations in capacitance, resistance, and leakage current, is the hyper-plane approach developed by Gisby *et al.* [27]. By tracking voltage, current, and charge as a function of time, the various slopes of the resulting 4D hyperplane can be used to derive each of the unknown quantities. Though it is quite thorough, this algorithm requires the measurement of charge on the electrodes. Additionally, it was seen to be quite sensitive to small changes in membrane dielectric constant resulting from strain.

Taking advantage of the finite conductivity of electrodes, more advanced applications are enabled by treating the actuator as a transmission line [29]. Due to electrode resistance, high sensing frequencies can result in decreased response and capacitance measurements at the far reaches of the electrode area. By sweeping through a range of sensing frequencies and measuring this decay, the localized strain can be measured using a single electrode pair. This enables exciting new applications such as reconfigurable soft keyboards made from dielectric elastomers [28, 80]

Finally, for applications requiring fast response times, online recursive algorithms have proven to be both computationally inexpensive and experimentally robust. Requiring only the measurement of voltage and current across the capacitor, and simultaneously measuring both variable capacitance and resistance, these algorithms can

take a number of forms, including the least mean squares (LMS) and the recursive least squares (RLS) algorithms initially investigated by Rizzello *et al.* [25], and further developed in later works [26,79]. Due to the relatively low computational cost of these algorithms, they are ideal candidates for high rate real-time implementations.

In this work, the RLS algorithm is implemented, as Rizzello *et al.* found it to be slightly more accurate than the LMS implementation. Using analytically derived voltage and current signals over a wide range of deformation frequencies, probing frequencies, and sampling frequencies, the output of the RLS algorithm is compared to the original capacitance input. With the goal of minimizing data volume for a desired accuracy at a particular deformation frequency, the RLS algorithm is optimized. The resulting optimization will be validated using a dielectric elastomer that is inflated and strained over time. The capacitance output of the algorithm will be compared to video-derived capacitance.

### 4.3 Methods

Capacitance was estimated using a recursive least squares (RLS) algorithm, which balances accuracy and computational speed, following the work of Rizzello *et al.* [25]. In this approach, the DEA is treated as a simple series RC circuit, where both the resistor and capacitor are variable in time. In this circuit, the relationship between voltage ( $V(t)$ ) and current ( $i(t)$ ) is:

$$i(t) = \frac{-1}{C(t)R(t)}Q(t) + \frac{1}{R(t)}V(t), \quad (4.1)$$

where  $Q(t)$  is the accumulated charge,  $C(t)$  is the capacitance, and  $R(t)$  is the resistance. This relationship can be discretized to each individual measurement,  $V_k$  and  $i_k$ . Assuming a sufficiently fast sampling rate, the charge can be approximated as:

$$\frac{Q_{k+1} - Q_k}{T_s} = i_k, \quad (4.2)$$

where  $T_s$  is the time step between samples. Taking the difference between each sample,

$$V_k - V_{k-1} = R_k i_k + \left( \frac{T_s}{C_k} - R_k \right) i_{k-1}. \quad (4.3)$$

If it can be assumed that voltage and current vary much faster than capacitance and resistance, Equation 4.3 is linear-in-parameters. This condition permits the application of online adaptive algorithms, such as RLS, where the values of the two linear parameters,  $R_k$  and  $T_s/C_k - R_k$ , are iteratively approximated at each timestep.

Two assumptions are necessary for the above analysis to be valid. For the linear-in-parameters assumption to be valid, it is necessary to probe the equivalent circuit at a frequency significantly higher than the expected changes in capacitance and resistance. Additionally, for the initial discretization to be valid, this probe voltage must be sampled at a sufficiently high frequency. This leads to the natural question of *how much* higher the sampling frequency ( $f_s$ ) must be relative to the probe frequency ( $f_p$ ), and similarly how much higher the probe frequency must be relative to the capacitance frequency ( $f_c$ ). To address the affect of each of these frequencies, an optimization study was undertaken.

### 4.3.1 Algorithm optimization

The algorithm was tested using analytical sinusoidal signals for capacitance and resistance, with white noise superimposed. Using the equivalent RC circuit and superimposing an applied probe voltage, the expected voltage and current outputs were calculated and fed into the RLS algorithm. The output was low-pass filtered, with a cut-off frequency of  $0.9f_p$ , and the estimated capacitance was compared with the analytical input in terms of amplitude, offset, and noise. In addition to varying  $f_c$ ,  $f_p$ , and  $f_s$ , the RLS forgetting factor,  $\mu$ , was varied, which acts to weight more recent samples more heavily in the estimation process. A forgetting factor of unity weights the entire time series equally, while a greater bias for recent samples is introduced as the forgetting factor is decreased. Typical values range from 0.9 to 1, though values as low as 0.5 were included in the optimization. The range of variables included in the optimization is shown in Table 4.1.

The effect of the forgetting factor can be approximated as  $\mu = 1 - 1/W$ , where  $W$  is the number of samples that will be weighted more heavily by the algorithm [25]. However, as the sampling frequency is varied, a constant forgetting factor will result in weighting different durations of a capacitance cycle. For example, if  $f_c = 1$  Hz,  $f_s = 1$  kHz, and the forgetting factor is set to 0.95, approximately 2% of the capacitance cycle will be weighted more heavily. If, then,  $f_s$  is decreased to 100 Hz, the same forgetting factor will weight 20% of the capacitance cycle more heavily. This effect can be taken into account with the use of a normalized variable,

$$N_c = \frac{f_c}{f_s(1 - \mu)}.$$

The variable  $N_c$  reflects the fraction of a capacitance cycle that is more heavily weighted by the RLS algorithm, regardless of any other variable values. When

**Table 4.1:** The range of variables used in the RLS algorithm optimization.

	$f_c$ (Hz)	$f_p$ (Hz)	$f_s$ (Hz)	$\mu$	$N_c$
Minimum	10	$3f_c$	$20f_p$	0.5	0.0013
Maximum	200	$80f_c$	$100f_p$	0.99	0.333

capturing dynamic changes in the capacitance, this variable will be shown to be a primary driver of the accuracy of the algorithm output, as will be discussed in Section 4.4.1.

### 4.3.2 Benchtop validation

The correlation between membrane strain and capacitance was validated in a series of benchtop experiments. A silicone membrane (BJB TC-5005 A/BC, 35% C), with carbon grease electrodes on top and bottom, was adhered to the top of an open cylindrical dish, creating a pressure vessel, as shown Figure 4.1. The strain in the membrane was manually varied by changing the pressure inside the dish over the course of 3600 seconds, and the electrodes were probed with a 1 kHz sinusoidal signal at 5 volts. The applied voltage and resulting current were recorded at 60 kHz and fed into the RLS algorithm for capacitance estimation. Additionally, the deflection of the membrane was measured by video at 60 Hz, as post-processed using the MATLAB Image Processing Toolbox.

Approximating that the pressurized membrane takes the shape of a spherical cap, the membrane stretch ( $\lambda$ ) is equal to  $4z^* + 1$ , where  $z^*$  is the peak membrane deflection normalized by the diameter of the pressure vessel. Assuming that the membrane material exhibits incompressibility and stretch-independent permittivity,



**Figure 4.1:** The benchtop membrane pressurization set-up, showing a membrane at an intermediate stretch. The compliant electrode, made from carbon grease, is seen on the surface of the transparent membrane.

stretch can be converted to expected capacitance such that:

$$C(t) = C_0\lambda^2, \quad (4.4)$$

where  $C_0$  is the capacitance of the unstrained membrane. Using this approach, the video frames were converted from membrane deflection to capacitance and compared with the RLS algorithm output.

## 4.4 Results and Discussion

### 4.4.1 Algorithm optimization

When considering the accuracy of the algorithm,  $N_c$  was seen to be the primary driver of amplitude accuracy. As plotted in Figure 4.2, it is seen that as  $N_c$  increases, the RLS algorithm increasingly underestimates the amplitude of capacitance variation. This is consistent with the physical representation of  $N_c$  - if  $N_c = 0.25$ , for example, the algorithm must estimate the capacitance at the next time-step using 25% of the previous capacitance cycle, thus smoothing the variation in capacitance over an

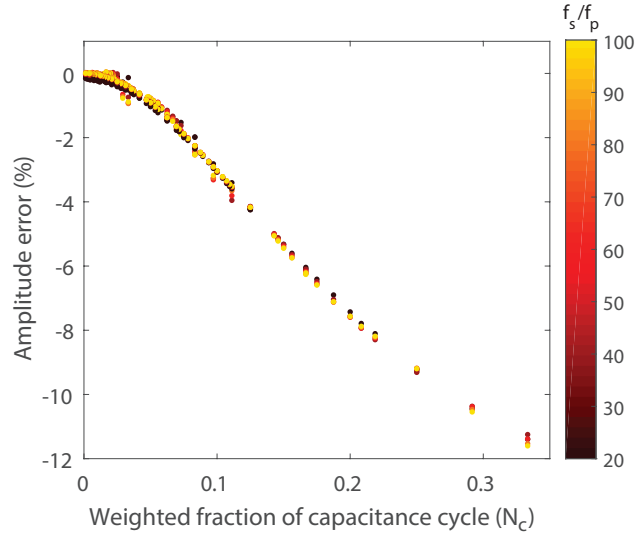


**Figure 4.2:** The effect of  $N_c$  on the accuracy of RLS output amplitude is shown for a range of  $f_c$ ,  $f_p$ ,  $f_s$ , and  $\mu$  values. It is seen that accuracy monotonically decreases with increasing  $N_c$ , regardless of the value of  $f_s/f_p$ , which is indicated by marker color.

unacceptably long period of time. Though this analysis uses pure sinusoid signals, it is equally applicable to more complex capacitance variations, with  $N_c$  acting similarly to a low-pass filter.

Taking this into account, the most accurate results require that only a small portion of the capacitance period should be heavily weighted in the algorithm. The primary implication of this finding is that the necessary sampling frequency is directly proportional to the maximum capacitance frequency that must be resolved. An application that must resolve capacitance variations up to 100 Hz will require  $f_s$  to be 100 times larger than an application that only requires capacitance variations on the order of 1 Hz to be resolved.

Additionally, it can be seen from Figure 4.2 that, if a goal is to minimize data volume, the lowest feasible forgetting factor should be chosen. However, Figure 4.3 indicates the limitation inherent to setting the forgetting factor. As the forgetting factor is lowered, noise becomes more prominent in the output. Because the algo-

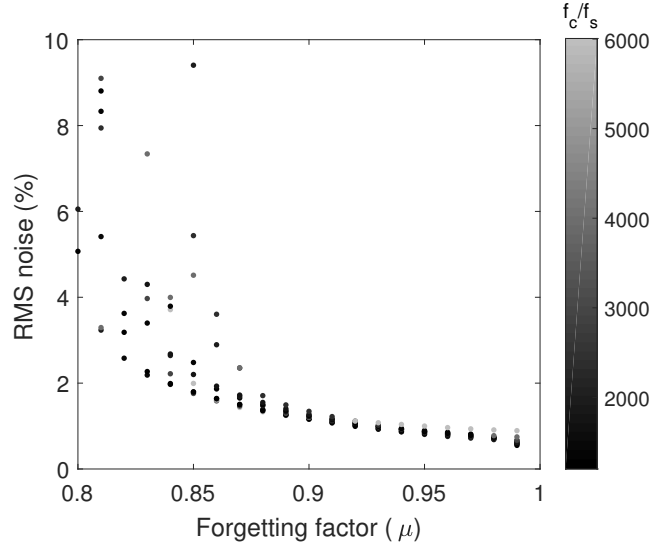


**Figure 4.3:** The effect of forgetting factor on the noise level of the RLS estimated capacitance is shown. It is seen that noise increases substantially at forgetting factors lower than 0.9. At higher lambda values, noise is low regardless of the ratio of sampling frequency to capacitance frequency (shown in grayscale).

rithm relies on numerical differentiation, this effect is likely caused by amplification of noise in the signal itself. As the forgetting factor is lowered, fewer and fewer samples are weighted heavily by the RLS algorithm, increasing the impact of the relatively high-frequency noise. Figure 4.3 shows that setting the forgetting factor below 0.9 results in a drastic increase in noise in the algorithm output – such values should be avoided. However, the minimum feasible forgetting factor is likely to be strongly influenced by the amplitude and type of noise in the experimental set-up, and should be characterized for each application.

The above analysis provides guidance on setting  $f_s$  and  $\mu$  for a desired level of accuracy at a particular deformation frequency. However, the probe frequency was not seen to play a significant role in either amplitude or noise in the RLS output. Probe frequency does have a significant effect on the mean value of the capacitance, as shown in Figure 4.4. The capacitance is seen to be increasingly underestimated as the sampling frequency decreases relative to the probe frequency, with underestimates in excess of 1% when the sampling frequency is less than 35 times the probe frequency.

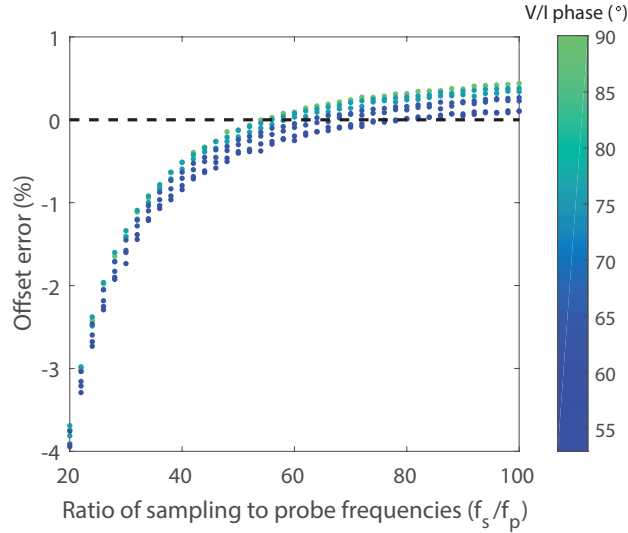


**Figure 4.4:** The effect of sampling frequency, normalized by probe frequency, on the offset error of the RLS estimated capacitance is shown. As the sampling frequency decreases, the algorithm increasingly underestimates the mean capacitance of the signal. For an offset error of 1%, the sampling frequency should be at least 35 times that of the probe frequency.

For applications in which the mean capacitance value is critical, as opposed to the frequency content, this frequency ratio should be taken into consideration.

In addition to the effect of  $f_s/f_p$ , a secondary effect is shown using marker color, representing the phase between voltage and current measurements. This phase is driven by the the ratio of resistance to reactance in the equivalent circuit, and can be easily varied using the probe frequency. Because the series RC circuit used to design the RLS algorithm is equivalent to a low-pass filter, the approximate resistance and capacitance can be used to estimate the phase between voltage and current.

Using this analysis, it becomes clear that the selection of probe frequency, sampling frequency, and forgetting factor are strongly application dependent. Applications that require only quasi-steady capacitance measurement will require much less data volume for high accuracy. However, unsteady phenomenon will require increasingly high probe and sampling frequencies for accurate results. The optimization shown here allows these variables to be selected based on the needs of the

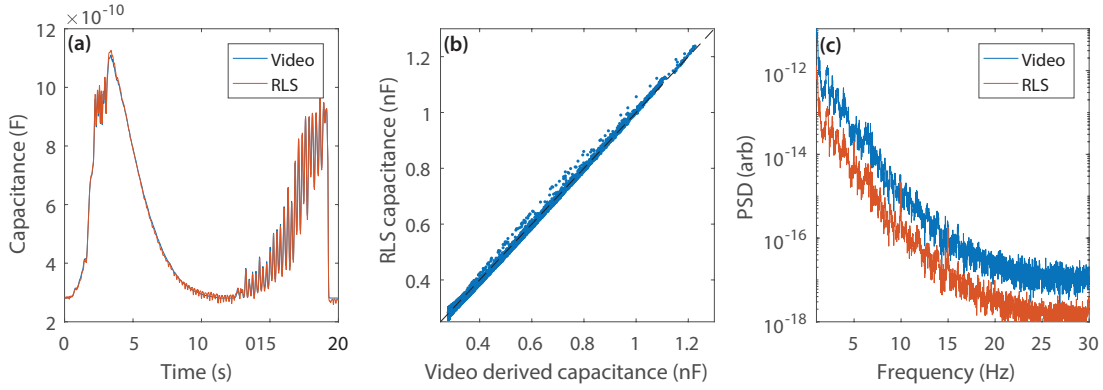


**Figure 4.5:** The RLS estimated capacitance is compared to the video-derived capacitance, over the course of six minutes of randomly varying membrane strains. (a) A representative example of video-derived and RLS capacitance values are shown over the course of 20 seconds, including both slow and fast changes in strain. (b) Comparing the values over the entire experiment, very close correlation between the values is seen, suggesting that the algorithm is performing well. (c) The frequency content of the two capacitance values (offset for clarity) compares well, showing that the RLS algorithm successfully captures capacitance variations up to the Nyquist frequency of the video data (30 Hz).

application at hand.

#### 4.4.2 Benchtop validation

The performance of the RLS capacitance estimation was tested using a pressure vessel to dynamically vary the inflation of a DEA membrane.

The RLS estimated capacitance is compared to the video-derived capacitance in Figure 4.5. In a representative time series including both fast and slow changes in strain, it is seen that the RLS algorithm closely tracks the video-derived capacitance. Indeed, when comparing the entire time-series in Figure 4.5(b), there is a close 1:1 correlation, with minimal scatter, which suggests that the capacitance measurements do not suffer from drift over the duration of the experiment, and good qualitative agreement is seen over a wide range of capacitance values. Additionally, as seen in Figure 4.5(c), the frequency content of the two measurement methods compares very

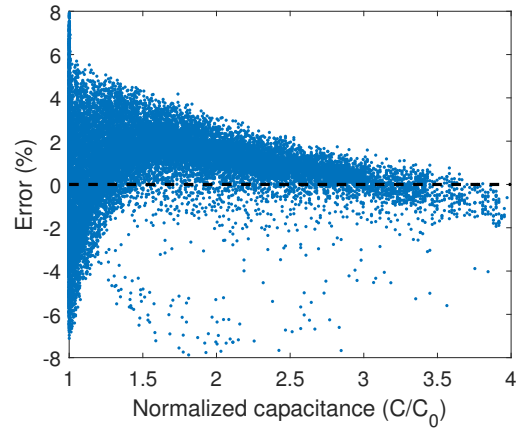


**Figure 4.6:** The error in RLS estimated capacitance  $((C_{video} - C_{RLS})/C_{video})$  is shown as a function of normalized capacitance. RLS capacitance estimations are seen to generally underpredict capacitance values at low strains, and become more accurate at higher strains.

well. This is particularly important in the context of unsteady applications, in which determining the frequency spectra of deformation is the primary goal.

Additional conclusions can be drawn on the limitations of this technique by plotting the error as a function of normalized capacitance, as shown in Figure 4.6, where the output capacitance is normalized by the unstrained value, and error is defined as  $(C_{video} - C_{RLS})/C_{video}$ . Applying Equation 4.4, it is seen that error in normalized capacitance would be proportional to error in  $\lambda^2$ . Thus, error would be expected to grow quickly in applications where very small strains are expected. However, the algorithm becomes more accurate at higher strains, where the measured capacitance will be significantly larger than  $C_0$ .

## 4.5 Conclusions

An RLS adaptive algorithm allows capacitance to be estimated with good accuracy and at low computational cost. But accuracy is highly dependent on the parameters

used for data collection (the probe and sampling frequencies), as well as the frequency of deformation that must be sensed and the forgetting factor applied during processing. Thus, the goal of minimizing data volume while maximizing accuracy for capacitive self-sensing can only be achieved by understanding each application's specific goal.

If deformation is expected to occur over relatively long timescales, the sampling frequency can be lowered without significantly decreasing accuracy, as captured using the variable  $N_c$ . The presence or relative absence of noise in the experimental may allow for the tuning of the forgetting factor without loss of accuracy, which also affects the value of  $N_c$ . Similarly, if amplitude of unsteady deformation is less important than the time-averaged values, the ratio of sampling to probe frequency should be treated as the primary driver of accuracy. As with any experimental method, trade-offs must be made. The work presented here aims to inform these trade-offs during the application of the RLS adaptive algorithm, specifically during capacitive self-sensing.

# CHAPTER FIVE

---

**Sensing aerodynamic load and flow  
structures using membrane wing  
deformation**

## 5.1 Abstract

Due to the compliant nature of extensible membrane wings, there exists a close relationship between the membrane wing camber and the aerodynamic load. Additionally, the membrane dynamics are often linked to unsteady large-scale flow structures, such as shear layer separation or leading edge vortex shedding. The integrated real-time measurement of the membrane configuration, including both mean camber and the frequency content of vibration, would lead to significant information on the surrounding flow field. In this work, one method of integrated camber sensing is demonstrated, and the relationship to aerodynamic load and flow field are shown. Camber is measured via the capacitance of the dielectric elastomer membrane, which is sandwiched between two compliant electrodes. The relationship between capacitance and camber is defined geometrically. The mean aerodynamic load is shown to be well-captured by applying a simple aeroelastic analysis to the measured camber. Finally, time-resolved flow field measurements are used to illustrate the ties between the dynamic camber, as measured by capacitance, and large-scale flow structures surrounding the wing. Ultimately, this work is a step towards developing an integrated, closed-loop control method for membrane wings.

## 5.2 Introduction

Dielectric elastomers have been shown to be effective as both actuators [2, 5, 81] and self-sensors [20]. A dielectric elastomer actuator (DEA) consists of an elastomeric membrane sandwiched between two compliant electrodes. When driven as actuators, a high voltage generates an out-of-plane strain, which is converted into an in-plane strain due to the incompressible nature of the material [2]. In an aerodynamic

environment, this strain can be used to generate both steady [48–50] and unsteady [51] changes in camber, when coupled with the aerodynamic pressure difference across the membrane.

As a self-sensor, the same DEA configuration can be driven with a high frequency/low voltage signal to measure the capacitance of the membrane [20]. As the membrane is deformed, the thickness decreases and the capacitance increases. In the context of a membrane wing under an aerodynamic load, this increase in capacitance may be used to approximate mean camber, which is related to mean aerodynamic load. Additionally, the variation of camber over time can be tied to dynamic large scale flow structures, such as shear layer location and vortex shedding [31, 34].

The connection between membrane wing camber and aerodynamic loading has been shown to be governed by a nondimensional aeroelastic number. This nondimensional number can take different forms based on the level of pretension in the wing, as introduced by Smith and Shyy [69] with the parameters  $\Pi_1$  for membrane wings with little to no pretension and  $\Pi_2$  for membrane wings dominated by pretension. Later, the need for two separate aeroelastic parameters for different prestrain values was alleviated by Waldman and Breuer [1], who developed an equivalent aeroelastic number that is consistent for both low and high pretension wings. Though a number of simplifying assumptions were made, including linear elasticity and even pressure distribution across the membrane, this framework was shown experimentally to predict membrane wing camber with good accuracy. Here, the inverse analysis will be used to predict aerodynamic load across a membrane wing using the mean membrane camber.

Membrane wings, by nature, respond unsteadily to any unsteady component of the surrounding flow field. Because of this, the dynamic camber of a membrane

wing can often be linked to large scale flow structures, such as the relative location of the shear layer or the frequency of vortex shedding. The frequency of membrane vibration has been shown to “lock-in” with the vortex shedding frequency, particularly near multiples of the natural frequency of the membrane [31,35]. Additionally, Rojratsirikul has demonstrated the correlation between the instantaneous locations of the shear layer and the membrane [36].

In this work, capacitive self-sensing will be demonstrated to be useful in a novel setting: membrane wing aerodynamics. Capacitance will be measured using an RLS adaptive algorithm. Wind tunnel measurements using a flat rectangular membrane wing will be presented, including aerodynamic load, capacitance, and single-point camber measurements using a laser displacement sensor. The relationship between these variables will be explored over a range of angles of attack and freestream velocities, using two membrane materials. Finally, time-resolved PIV will be used to show links between capacitance measurements and large-scale flow structures. This application of dielectric membrane self-sensing may, in the future, be incorporated with existing methods for membrane wing active flow control [51] to enable closed-loop control of membrane wings.

### 5.3 Methods

To test the performance of capacitive self-sensing under aerodynamic load, membrane wing frames were constructed of acrylic, with a span of 180 mm, a chord of 90 mm, and a thickness of 6.35 mm. For membrane mounting, two segments of 76 mm  $\times$  76 mm were cut on either side of the centerline, as shown in Figure 5.1(a). Two membrane materials were used for testing - a hyperelastic silicone (TC-5005 A/BC,

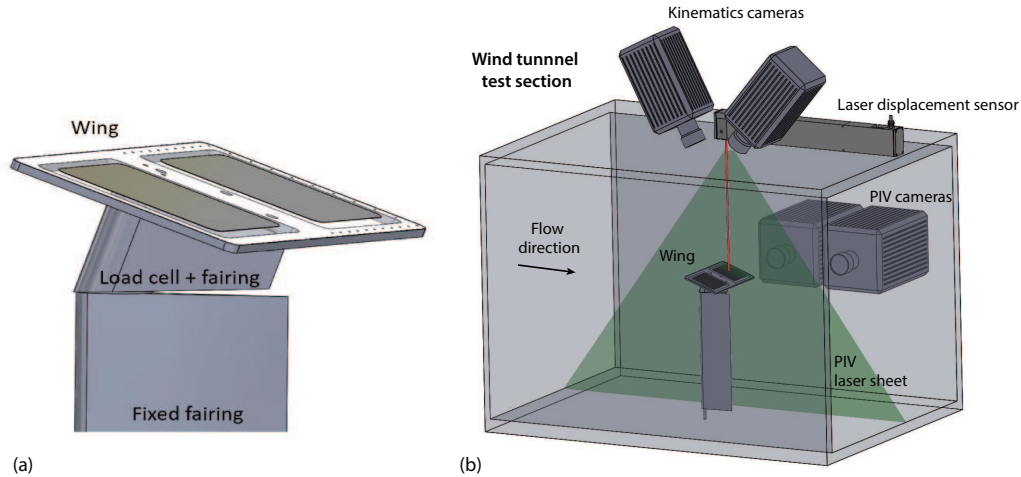


**Figure 5.1:** (a) The membrane wing is constructed from a rigid frame, to which the membrane is adhered. The load cell is mounted on a custom angle of attack adapter. (b) The wing is mounted in the center of the wind tunnel test section. Kinematics cameras are used to capture membrane kinematics, 2D-2C PIV is used to measure the surrounding flow, and a single-point laser displacement sensor measures the displacement at the center of a membrane segment.

35% C, BJB Enterprises) and a viscoelastic acrylic (VHB 4905, 3M). The silicone has a nominal thickness of 1 mm, and was tested at a prestrain of 175%, while the acrylic is 0.5 mm thick, and was tested at a prestrain of 250%. At these values of prestrain, the silicone and acrylic are approximated as linear elastic with Young’s moduli of 20.1 kPa and 41.6 kPa, respectively. Carbon grease electrodes (MG Chemicals) were applied to top and bottom of both segments for the application of both probe and actuation voltages, with a gap of approximately 3.5 mm between the perimeter of the electrode and the perimeter of the frame. Voltages were generated using a high voltage amplifier (Model 5-80, Trek) and a function generator (DS345, Stanford Research Systems).

The wing was tested in a closed-loop wind tunnel (Figure 5.1(b)), in the center of a test section measuring  $0.61 \text{ m} \times 0.61 \text{ m}$  in cross-section and 2.4 m in length. The wing was positioned at a fixed angle of attack, using a fixed fairing and a custom angle of attack adapter. A six-axis load cell (F/T Nano17, ATI Industrial Automation) was installed at the wing’s quarter-chord for measurement of the aerodynamic loads

and torques. To ensure load cell accuracy, the temperature in the test section was controlled to within  $0.1^\circ$  of the tare temperature using a water-cooled heat exchanger. Aerodynamic load data was collected at 10 kHz.

A single-point laser displacement sensor (AR700-16, Acuity Laser) was positioned outside the test section and focused on the center of one of the membrane segments. The displacement of the membrane at this location was recorded at 1 kHz. Additionally, two high speed cameras ( $1024 \text{ pixels} \times 1024 \text{ pixels}$ ) (Photron SA4, Photron Ltd) were used to capture 2D-2C PIV data in a plane parallel to the wing chord, at quarter-span (the center of the membrane segment). The plane was illuminated with a laser sheet generated using a double-pulsed Nd:YLF laser (527 nm) (DM30, Photonics Industries), with an energy output of approximately 30 mJ/pulse. PIV data was captured at a rate of 500 Hz.

Two datasets were collected for analysis. In the first dataset, only aerodynamic load and single-point membrane displacement data were collected, but at fine resolution of freestream velocity and angle of attack. Freestream velocities between 2 and 25 m/s were captured, with a resolution of approximately 2 m/s. Angles of attack were varied from  $2^\circ$  to  $30^\circ$ , in increments of  $2^\circ$ - $5^\circ$ . In addition to varying the velocity and angle of attack, both membrane materials (silicone and acrylic) were tested. Finally, data was collected both with and without high-voltage actuation. Without actuation, a sinusoidal probe voltage of 1500 Hz and 200 V was applied. For high-voltage actuation, the same probe voltage was superimposed on an actuation voltage of the form  $V(t) = 2000(1 + \sin 2\pi f_{act}t)$ , with actuation frequencies ( $f_{act}$ ) ranging from 20 Hz to 75 Hz. In all cases, the voltage and current across the membrane were recorded at 60 kHz, with a duration of 60 seconds.

In the second dataset, the primary goal was to capture unsteady interactions

between the membrane kinematics and the surrounding flow field. As such, this dataset includes the full complement of data streams: PIV data, single-point membrane displacement data, membrane capacitance, and aerodynamic load data. Due to time constraints, this analysis will focus on a single set of experimental conditions: a VHB membrane wing at  $5^\circ$  angle of attack and 16 m/s freestream velocity. This dataset was chosen due to a significant amount of observed membrane vibration and the proximity of the shear layer to the membrane. Future work will demonstrate the technique for a wider range of experimental conditions.

## 5.4 Results and Discussion

### 5.4.1 Measurement of wing camber

Capacitive self-sensing was demonstrated on a membrane wing under aerodynamic load. The camber of the membrane was estimated by assuming the membrane geometry to be approximately that of a spherical cap [82]. With that assumption, it can be shown that:

$$z^* = \sqrt{\frac{\lambda - 1}{4}} = \sqrt{\frac{\sqrt{C/C_0} - 1}{4}}, \quad (5.1)$$

where  $z^*$  is the membrane camber,  $\lambda$  is the camber-induced stretch,  $C$  is the instantaneous capacitance, and  $C_0$  is the capacitance of the uncambered wing. It should be noted that the spherical cap approximation deviates slightly from the deformation of a pre-tensioned square membrane under uniform load, which can be closely approximated as [83]:

$$z_{sq}^* = 0.0737 \frac{P_C^2}{T}, \quad (5.2)$$

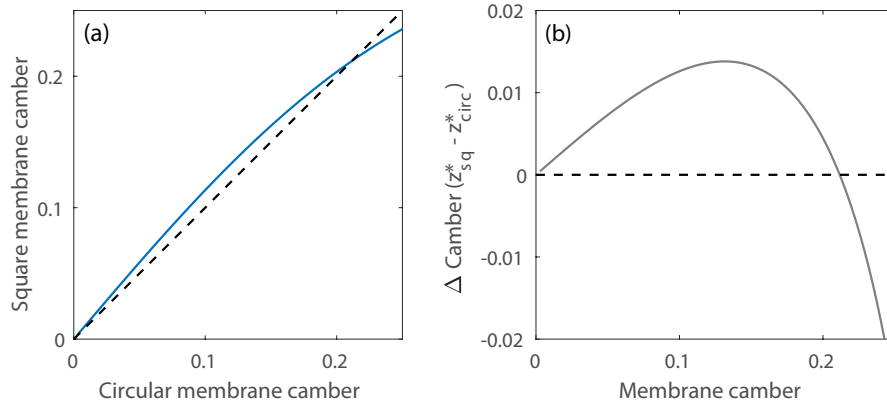


**Figure 5.2:** Analysis of the error introduced by the spherical cap assumption. (a) The camber predicted for a circular vs. a square membrane under uniform pressure is shown. (b) The error in camber is shown for the range of cambers observed in this work.

where  $P$  is the uniform applied pressure,  $c$  is the membrane wing chord, and  $T$  is membrane tension. As shown in Figure 5.2, comparing the expected cambers from each of these expressions over the range of cambers observed in this work, the spherical cap assumption results in overestimations by as much as 1.4% camber at 13.1% camber, while underestimating for cambers in excess of 21.3%. However, the spherical cap assumption allows the use of a simple analytical expression for membrane strain, which is not available for a square membrane under equivalent conditions, and will be applied throughout this work.

In Figure 5.3, the capacitance calculated with the recursive least squares (RLS) algorithm, as developed in Chapter 4, is compared to the camber as measured using the single-point laser displacement sensor. Figure 5.3(a) shows the comparison in the absence of high voltage actuation, with only the probe voltage applied. Data from the acrylic membrane is shown in cool colors, while the silicone membrane is shown in warm colors. The angle of attack is indicated with marker color, and the freestream velocity with marker size. Fairly close agreement between the displacement sensor and the camber measured via capacitance is seen, particularly at cambers above 4-5%. At low cambers, more scatter is seen, as was predicted in the error analysis of

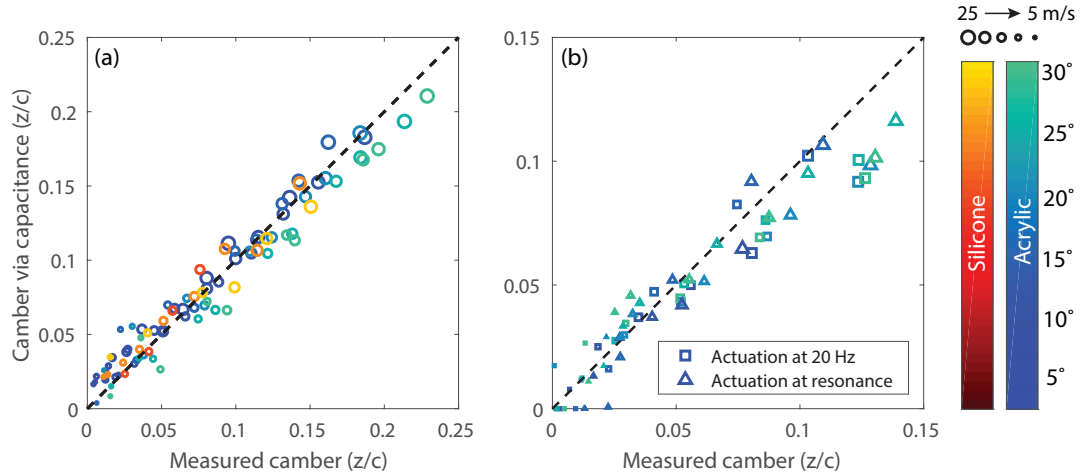


**Figure 5.3:** The mean camber as measured by displacement sensor is compared to the mean camber as measured by capacitance for (a) purely sensing (without actuation) and (b) sensing during actuation. Acrylic membrane results are shown in cool colors, while silicone tests are shown in warm colors. The angle of attack is indicated with shade, and the freestream velocity with marker size. Additionally, for tests that included actuation, both off-resonance (20 Hz) and on-resonance actuation frequencies were tested.

the benchtop results, presented in Chapter 4.

Figure 5.3(b) shows the same comparison during high voltage actuation of the membrane, with the low-amplitude/high-frequency probe voltage superimposed over the high-amplitude/low-frequency actuation voltage. At each experimental condition, actuation was performed at two frequencies: a constant frequency well below resonance (20 Hz), as well as the membrane resonance frequency. The resonance frequency is influenced by camber-induced strain and ranged from 54 to 75 Hz, as was identified for each run using a frequency sweep. For both frequency conditions, good agreement is generally seen between the displacement sensor camber and the camber measured via capacitance, though capacitive self-sensing tends to under-estimate the camber at higher mean camber values. The reason for this loss of accuracy requires further analysis, but may be connected to the spherical cap geometric assumption discussed earlier.

In addition to measuring the time-averaged camber, capacitive self-sensing is

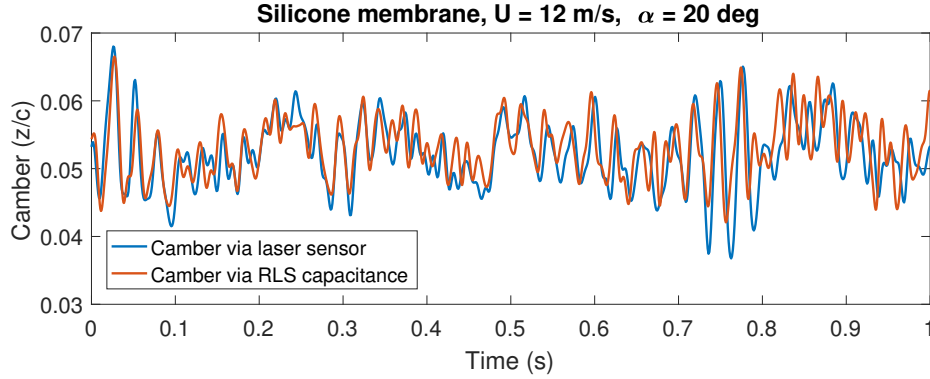


**Figure 5.4:** A representative time series of the measured camber is shown, for laser displacement sensor measurements (blue) and capacitive self-sensing estimates (red). Good correlation between the signals is seen, though some variations in amplitude and frequency are seen intermittently.

capable of measuring the dynamic camber of the membrane. A representative time series is shown in Figure 5.4, comparing the camber measured via both displacement sensor (blue) and capacitive self-sensing (red) over the course of one second. Good qualitative agreement is seen between the the two methods, with large-scale changes in camber being well captured and the frequency content appearing to be quite similar. Some variations in amplitude are seen (e.g, between 0.7 and 0.8 seconds), and some areas seem to have different frequency content (e.g, between 0.8 and 0.9 seconds). However, these variations are to be expected when comparing single-point and full-field measuring techniques. Any vibration mode that is not of the  $\langle 1 - 1 \rangle$  mode may lead to some slight variations between these two measurement techniques.

The correlation between the two measurement techniques can be quantified using a cross-correlation analysis on the full 60 second duration of each measurement period. The cross-correlation coefficient may vary from zero, indicating absolute lack of correlation, to unity, indicating perfect correlation. The time-series in Figure 5.4, for example, has a cross-correlation coefficient of 0.744. In Figure 5.5, this coefficient is shown for all tested configurations as a function of mean camber. The correlation is seen to be poor at cambers below 4% before reaching a plateau of roughly 0.5-0.8 at higher mean cambers. The loss of accuracy is consistent with the

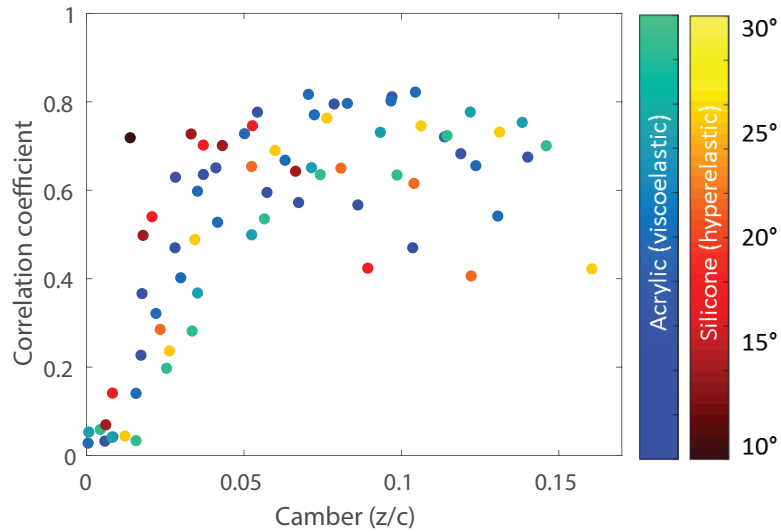


**Figure 5.5:** The cross-correlation coefficient is shown as a function of camber, for both acrylic and silicone membranes. Very little correlation is seen at low cambers, with correlation coefficients increasing to 0.5-0.8 at cambers of above roughly 4%. This trend holds across all angles of attack and velocities tested, for both acrylic and silicone membranes.

analysis of benchtop results in Chapter 4. Because the camber measurement is a function of the time-varying capacitance normalized by the unstrained capacitance, small changes are difficult to detect. Additionally, the failure to reach perfect correlation is similarly expected, based on the previous argument regarding differences between single-point and full-field measurement techniques. Ultimately, capacitive self-sensing appears to produce reliable results at mean camber values above 4%, in both mean camber and dynamic camber measurements.

### 5.4.2 Measurement of aerodynamic load

Following the analysis of Waldman and Breuer [1], the camber can be used to estimate the aerodynamic load on the membrane. The Young-Laplace equation allows the curvature of the membrane ( $\kappa$ ) to be balanced with the aerodynamic pressure

( $p$ ), and the tension in the membrane ( $T$ ):

$$\kappa + \frac{p}{T} = 0, \quad (5.3)$$

which can be rearranged to solve for the pressure on the membrane:

$$p = T\kappa. \quad (5.4)$$

Assuming a uniform pressure distribution, linear elasticity in the membrane (i.e.,  $T = Eh(\lambda - 1)$ ), and a membrane shape that can be approximated by a spherical cap geometry (i.e.,  $\kappa = 8z^*/(1 + 4z^{*2})$ ), the force acting normal to the membrane (i.e., pressure) can be solved as:

$$F_N = Eh(\lambda - 1) \frac{8z^*}{1 + 4z^{*2}} \quad (5.5)$$

where  $E$  is the membrane Young's modulus,  $h$  is the membrane thickness,  $\lambda$  is the instantaneous membrane stretch, and  $z^*$  is the membrane camber. With a known angle of attack ( $\alpha$ ), the normal force acting on the membrane can be decomposed into the lift ( $L$ ) and drag ( $D$ ) force, such that:

$$F_N = L \cos(\alpha) + D \sin(\alpha). \quad (5.6)$$

Applying this analysis to the dataset at hand, the measured normal aerodynamic load is compared to the derived force using the measured capacitance in Figure 5.6(a). The measured and predicted normal force collapses well throughout the range of parameters tested, including both silicone and acrylic membranes over a range of angles of attack (shown with color shading) and freestream velocities (shown with marker size). Some deviation is seen at the highest loading scenarios, which may

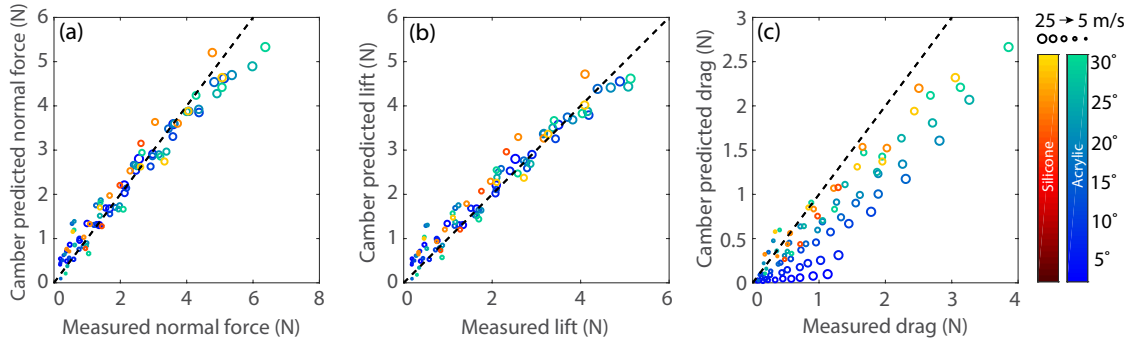


**Figure 5.6:** (a) The aerodynamic load normal to the membrane is estimated via capacitance, and compared with the measured normal load. This force is then decomposed into (b) lift and (c) drag using the angle of attack.

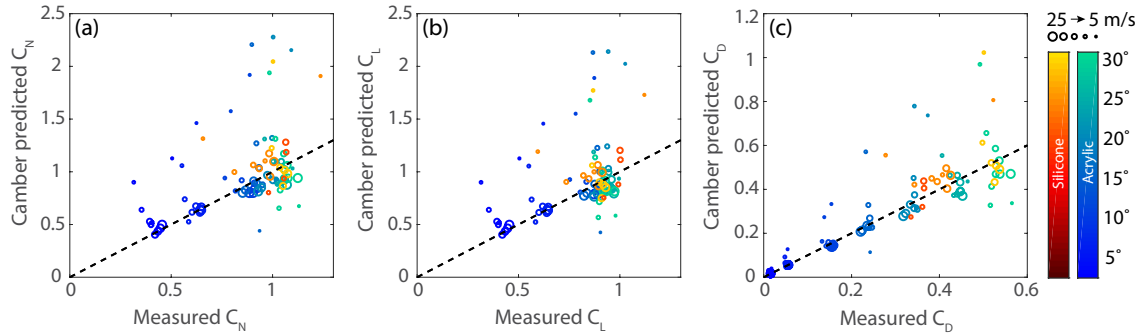


**Figure 5.7:** Aerodynamic loads are converted into aerodynamic coefficients, including (a) the normal force coefficient, (b) the lift coefficient, and (c) the drag coefficient. Good agreement is seen at higher velocities (larger markers), with loss of accuracy at low velocities (small markers).

indicate that the linear elastic assumption is breaking down with increasing camber-induced strain. The normal load is also broken down into lift (Figure 5.6(b)) and drag (Figure 5.6(c)). The lift force is seen to be well collapsed, with some scatter at low forces. This is consistent with an observed increase in error at low cambers, and is a consequence of dividing by the unstrained capacitance to approximate the membrane strain. Finally, the derived drag is seen to be the least accurate quantity, and is consistently underestimated, particularly at low angles of attack. This is likely a result of the increasingly small proportion of the overall normal force that is directed in the drag direction at low angles of attack.

The aerodynamic forces being applied to the membrane can be converted into

aerodynamic coefficients by dividing by the dynamic pressure. The comparison between measured coefficients and predicted coefficients is shown in Figure 5.7 using the same data and legend as in Figure 5.6. In all three cases ( $C_N$ ,  $C_L$ , and  $C_D$ ), the freestream velocity is seen to be the strongest predictor of accuracy, with predicted coefficients generally rising well above measured coefficients as freestream velocity decreases. This loss of accuracy is another reflection of the increasing error at low cambers. Velocity is the primary driver of membrane wing self-cambering [31], with camber increasing roughly proportionally to  $U^2$ . At low velocities, the mean membrane camber is below the threshold of 4% that was identified in Section 5.4.1, and accurate measurements are not possible. However, the predicted coefficients, including  $C_D$ , are seen to be captured with much greater accuracy at higher freestream velocities.

### 5.4.3 Connection with flow structure

In addition to sensing time-averaged camber and aerodynamic forces, capacitive self sensing can provide some insight into the flow structures surrounding the wing. At high angles of attack, vortex shedding may be the primary phenomenon to be captured with capacitive self-sensing. At lower angles of attack, the location of the shear layer relative to the wing surface can be sensed, as will be demonstrated here using high speed PIV collected simultaneously with capacitance and aerodynamic load data.

A wing at  $5^\circ$  angle of attack in a 16 m/s freestream velocity will be used for the purposes of this demonstration. The mean vorticity field and streamlines are shown in Figure 5.8(a), where it is seen that the flow remains largely attached the the surface of the wing. In addition to the mean flow field, the mean membrane

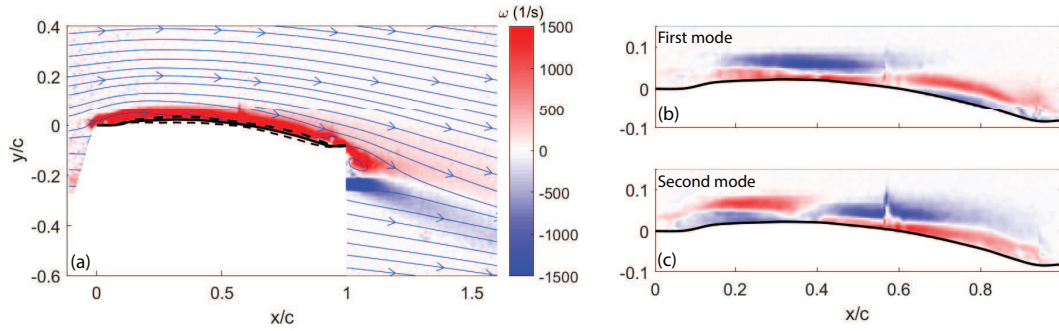


**Figure 5.8:** (a) The time-averaged vorticity field and streamlines are shown for a membrane wing at  $5^\circ$  and 16 m/s. The mean membrane camber is shown (solid black line), as well as the camber standard deviation (dashed lines). Additionally (b) the first POD mode and (c) the second POD mode are shown for the region of interest immediately above the membrane.

shape is shown (solid black line), as well as the standard deviation of the membrane deformation (dashed black lines). Under these flow conditions, the mean camber is 5.7%, which is modestly above the cut-off for accurate capacitive self-sensing results, while the standard deviation of the camber is roughly 0.8%.

In addition to the mean flow field, the flow field dynamics are captured using Proper Orthogonal Decomposition (POD), which utilizes an eigenvalue analysis to decompose the unsteady flow field into the most energetic modes [77]. Following the identification of modes, the relative contribution of each mode is calculated at each time-step. These coefficients capture the time-varying nature of each mode and can be used to calculate frequency content. In Figure 5.8(b-c), the first two POD modes of the vorticity field immediately above the wing surface are shown. The first POD mode, in particular, appears to suggest a node at roughly  $0.5c$ , which will be seen to be reflected in membrane deformation data as well.

A POD analysis can also be applied to the membrane dynamics, as detected by the reflection of the PIV laser sheet on the membrane surface. The first three POD modes of the membrane deformation are shown in Figure 5.9(a), as well as the cumulative energy captured by the first five POD modes in Figure 5.9(b). The first

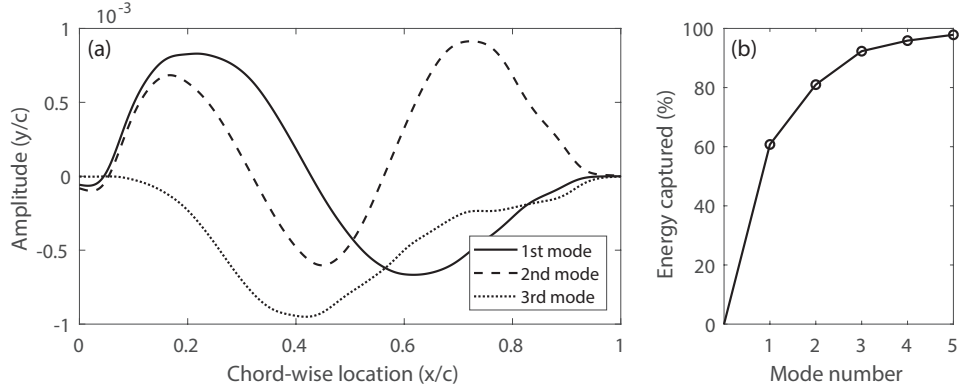


**Figure 5.9:** (a) The first three POD modes are shown for the membrane deformation along the chord at quarter-span of the wing. In (b), the cumulative energy captured in the first five POD modes is shown. Over 90% of the dynamics are captured in the first 3 modes.

mode, which captures 61% of the membrane dynamics, represents a second mode vibration in the chordwise direction, with a nodal line at roughly  $0.5c$ . The second POD mode captures a  $< 1 - 3 >$  vibration mode, while the third POD mode is a fundamental vibration mode. The combination of these first three modes captures 92.3% of the overall membrane dynamics. The first POD mode, in particular, will be seen to be tightly coupled with the surrounding flow and will be the focus for the remainder of the analysis.

To begin to understand the interplay between the flow field and the wing, the power spectral density (PSD) of several variables can be considered. In addition to lift and capacitance, the PIV POD coefficients and shear layer height were calculated. The shear layer height was defined as the location of maximum vorticity above the membrane. This value was measured as a function of location along the chord, and the shear layer height at  $0.5c$  was used for the PSD analysis.

The frequency content of these four variables, as shown in Figure 5.10, shows some clear connections between the wing and the surrounding flow. Two primary peaks are seen in both the PIV POD spectra and the shear layer height spectra, at 47 Hz and 66 Hz. Assuming the peak at 47 Hz to be a  $< 1 - 2 >$  mode resonance peak,

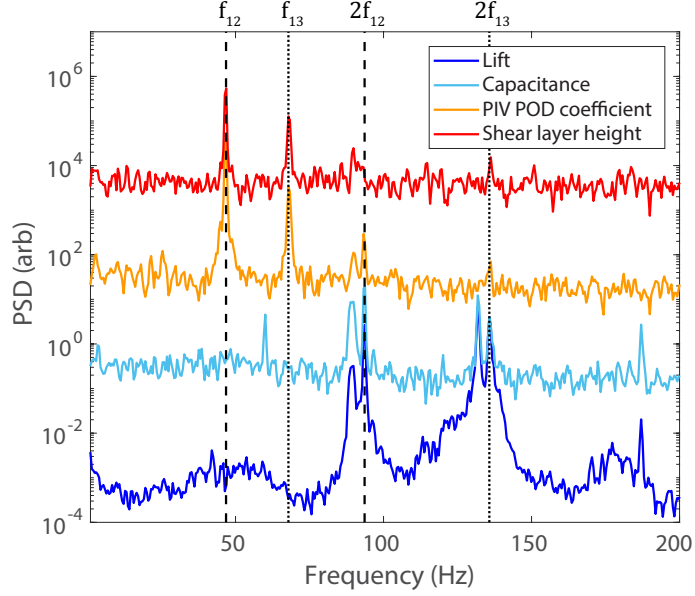


**Figure 5.10:** The power spectral density is shown for lift, capacitance, membrane strain, and shear layer location at  $0.5c$ . The peak frequencies for lift and capacitance are seen to be doubled relative to the peak frequencies for membrane strain and shear layer location. Spectra are offset for clarity.

$f_{12}$ , it can be noted that 66 Hz is equal to  $\sqrt{2}f_{12}$ . Because the vibration frequency of a square membrane is defined as [72]:

$$f_{nm} = \frac{1}{2c} \sqrt{\frac{E(\lambda - 1)}{\rho_m}} \sqrt{n^2 + m^2}, \quad (5.7)$$

where  $c$  is the membrane chord,  $E$  is the Young's modulus,  $\lambda$  is the applied prestretch, and  $\rho_m$  is the membrane density, it can be seen that the  $\sqrt{2}$  factor is consistent with the ratio of  $f_{12}$  to  $f_{13}$ . Just as the membrane dynamics were seen to be dominated by the  $\langle 1 - 2 \rangle$  and  $\langle 1 - 3 \rangle$  modes, the dominant frequencies in the surrounding flow field are connected by the same factor.

The frequency peaks of the lift and capacitance, however, occur at double the frequency peaks of the shear layer height and PIV POD, suggesting that both lift and capacitance are agnostic as to the phase of vibration. This frequency doubling is likely tied to the nature of the membrane vibration and surrounding vorticity fields.

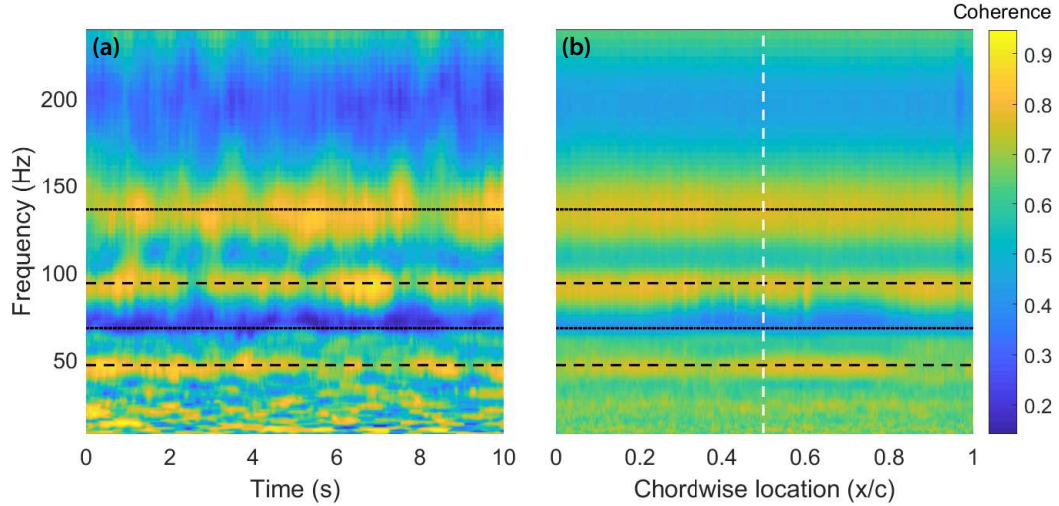


**Figure 5.11:** The coherence of lift with the shear layer location is shown as a function of (a) time and (b) the chord-wise location on the membrane. Time-based coherence was taken at  $0.5c$ , and the spatial coherence was averaged over the full time-series, such that the white dashed line is the average of the time-based plot. In both cases, bands of coherence are seen at  $f_{12}$ ,  $2f_{12}$ , and  $2f_{13}$ , with very little coherence at  $f_{13}$

In the POD analyses of both of these variables, most of the energy was seen to be in the  $\langle 1 - 2 \rangle$  vibration mode, such that vorticity and membrane stretch had a node of minimal variation at approximately  $0.5c$ . However, capacitance would essentially rectify this sinusoidal stretch, resulting in a frequency doubling.

To better understand the connection between lift, capacitance, and flow structures, the coherence between the various quantities can be measured. Perfect coherence indicates that two signals have a constant phase lag, identical frequency content, and identical waveforms. To measure coherence as a function of time and frequency, the Morelet wavelet coherence was computed using MATLAB’s Wavelet Toolbox. The coherence of lift with the shear layer location measured at  $0.5c$  is shown in Figure 5.11(a) over time. The same four frequencies that are marked in Figure 5.10 are also indicated with black dashed and dotted lines. Bands of relatively high coherence are seen at  $f_{12}$ ,  $2f_{12}$ , and  $2f_{13}$ , with minimal coherence at  $f_{13}$ . Interestingly, though the lift signal has very little energy at  $f_{12}$ , and the shear layer measurement has very little energy at  $2f_{12}$  and  $2f_{13}$ , the energy present at these frequencies indicates high

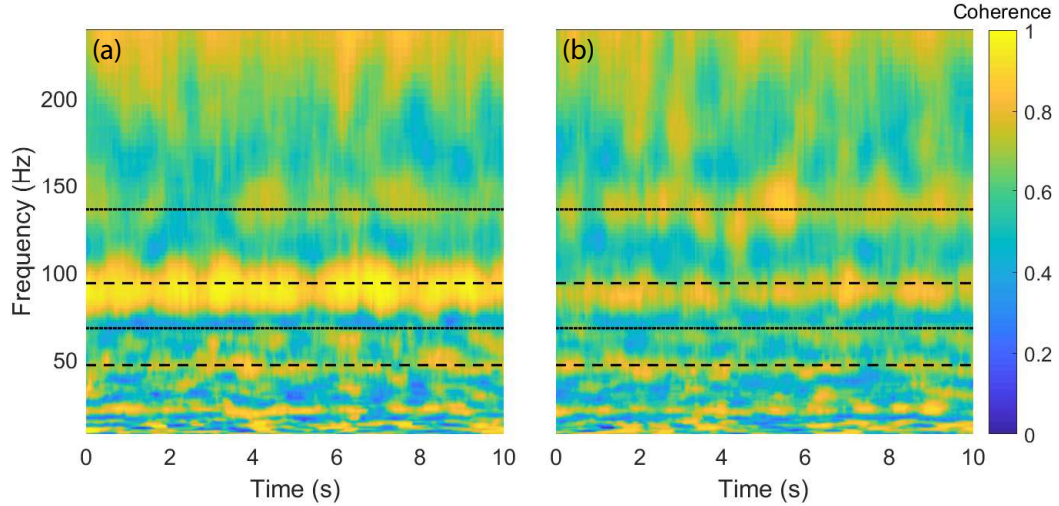


**Figure 5.12:** The coherence of the capacitance with (a) the first POD mode coefficient and (b) the second POD mode coefficient is shown as a function of time. For the first POD mode, high coherence is seen across the entire time series at  $2f_{12}$ . Less coherence is generally seen with the second POD mode, though there are bands of somewhat enhanced coherence at both  $2f_{12}$  and  $2f_{13}$

correlation between lift and the shear layer location.

Because the shear layer location is measured at every chord-wise location on the wing, the coherence with lift can also be calculated as a function of location, as shown in Figure 5.11(b). In this case, each vertical cross-section represents the time-averaged coherence of the lift and shear layer location, such that the white dotted line corresponds to the time-averaged values from Figure 5.11(a). Just as coherence was seen to be relatively time independent in Figure 5.11(a), it is seen to be quite independent of location on the wing.

Ultimately, for capacitance to be a useful sensing device for the surrounding flow structures, coherence between the capacitance and the flow field must be demonstrated. Because capacitance inherently measures the deflection of the whole membrane, a variable that captures the full flow field is the most likely to be coherent with capacitance. This is accomplished by using the coefficients of the first two POD modes of the PIV field immediately above the membrane (Figure 5.8(b-c)). By mea-

suring the coherence of the capacitance with POD mode coefficients, two full-field quantities can be compared.

As shown in Figure 5.12(a), for the first PIV POD mode, the POD coefficients and capacitance show a high level of coherence at  $2f_{12}$  across the full time-span measured, with much lower levels of coherence seen at other frequencies. This frequency doubling is consistent with capacitance measured during  $\langle 1 - 2 \rangle$  mode vibrations, as previously discussed. The high level of coherence at a frequency relevant to the surrounding flow field demonstrates that, indeed, capacitive self-sensing can be used to detect relevant flow structures that interact with the membrane wing.

Furthermore, extending the analysis to the second POD modal coefficient (Figure 5.12(b)), some additional coherence can be seen in the  $f_{13}$  band. Considering the relative contributions of the  $\langle 1 - 2 \rangle$  and  $\langle 1 - 3 \rangle$  modal vibrations to the membrane dynamics (Figure 5.9(b)), it is seen that the  $\langle 1 - 2 \rangle$  mode accounts for 61% of the total energy, while the  $\langle 1 - 3 \rangle$  mode captures only an additional 20% of the total energy. Because of this differential in total energy, it is perhaps not surprising that the strongest coupling between membrane deformation and the surrounding flow field is seen in the  $\langle 1 - 2 \rangle$  mode. However, the enhanced coherence at  $f_{13}$  does suggest that higher order flow structures can be sensed using membrane wing capacitance.

## 5.5 Conclusions

In this work, capacitive self-sensing has been demonstrated to be effective in detecting membrane wing camber above a noise floor of roughly 4% camber. Because

membrane wings are dynamically self-cambering based on the instantaneous aerodynamic loading, camber sensing naturally leads to the ability to approximate the steady and unsteady aerodynamic pressure that the wing is experiencing. Finally, because the dynamic component of the aerodynamic pressure is largely influenced by flow structures surrounding the wing, it is possible to show the connection between unsteady capacitance and changes in the surrounding flow. In this case, the unsteady oscillation of the relative location of the shear layer above the membrane was demonstrated to be highly coherent at the frequency of oscillation.

Though membrane wings demonstrate some significant advantages over rigid wings at low Reynolds numbers, challenges of implementing active sensing and flow control prevent any real-time response to changing flow conditions. With sufficient development, this sensing technique has the potential to provide that capability. Though the technique would benefit from further refinement in order to lower the noise floor and extend the range of aerodynamic conditions under which it generates accurate results, the utility of capacitive self-sensing is broad and promising. When combined with the ability to actuate the membrane for active flow control, the information gained through capacitive self-sensing could ultimately lead to closed-loop control in micro-air-vehicle applications, using a simple, cheap, and integrated sensor/actuator.

# CHAPTER SIX

---

## Conclusions

This work concerns the development of sensing and flow control techniques for membrane wings at low Reynolds numbers. While a few options have previously been demonstrated for active flow control (specifically, the DC and AC actuation of dielectric elastomer actuators), here we explore the parameter space of AC actuation in greater detail, allowing the underlying mechanics to be more fully clarified. Regarding self-sensing, no fully integrated methods currently exist - the measurement of camber, aerodynamic load, and surrounding flow structures generally requires significant external equipment. The combination of integrated self-sensing and active flow control, ultimately, lays the groundwork for implementing closed-loop control of membrane wing micro-air-vehicles.

Self-sensing has been implemented by measuring the variable capacitance of the membrane wing as it deforms. The capacitance is calculated using a recursive online RLS algorithm, which was optimized and validated on the benchtop. With the addition of aerodynamic load in a series of wind tunnel tests, it was shown that capacitance could be used to accurately measure cambers above 4%, and that these cambers could be correlated to mean and dynamic aerodynamic load. Additionally, it was shown that variations in camber (and the corresponding capacitance) are coherent with the dynamics of the surrounding flow, as measured with POD decomposition coefficients, for a single test case of 16 m/s freestream velocity and 5° angle of attack. The demonstration of additional test cases, such as a separated flow with bluff body vortex shedding, remains for future work.

Active flow control via AC actuation of a dielectric elastomer actuator was also demonstrated, and the underlying mechanism of flow control was discussed. Effective flow control was seen to be a function of shear layer location, fluid-induced damping, and reduced frequency effects. Lift enhancements on the order of 20% were seen when these factors had been optimized, at roughly 10 m/s freestream velocity, 20° angle

of attack, and a reduced frequency of order unity. Near this range of variables, the shear layer is separated from the leading edge, but remains close enough to the wing to be influenced by the unsteady camber. Additionally, effective flow control is only possible when membrane actuation results in significant unsteady camber variations, which is negatively impacted by fluid-induced damping at freestream velocities above 15 m/s. Finally, the frequency of actuation must be such that instabilities in the separated shear layer are effectively excited, resulting in shear layer vortex roll-up. When these three contributing factors are met, lift enhancement via AC actuation of the membrane wing is most effective.

While both active flow control and membrane self-sensing were demonstrated to be effective over a certain range of variables, the respective ranges could be significantly expanded with further development work. In the case of self-sensing, cambers under 4% cannot be accurately measured due to the presence of a noise floor. Lowering this floor with the application of additional pre- or post-processing filtering would significantly expand the range of applications for the technique. Additionally, further development of the RLS algorithm could lower the sampling frequency necessary for accurate capacitance calculations, potentially enabling real-time processing, as would be necessary for closed-loop control.

Active flow control could be similarly optimized for performance over a wider range of aerodynamic variables. First and foremost, the effect of fluid-induced damping may be counteracted by improving membrane actuation amplitude, extending the range of freestream velocities over which this method of active flow control is effective. This may be accomplished in many ways, such as raising the relative permittivity of the material, decreasing the elastic modulus, decreasing viscoelastic damping, or increasing the maximum applied electric field. The body of literature on dielectric elastomer actuators suggests many ways to optimize actuation authority,

any of which might be effective in overcoming fluid-induced damping at moderate freestream velocities and increasing the range of parameters over which active flow control is possible.

Ultimately, this work aims to provide proof-of-concept demonstrations of integrated self-sensing and active flow control for membrane wings, along with an understanding of the underlying mechanics and limitations of each method. While additional work in optimization and development promises to extend the usefulness of these techniques, the fundamental approaches have been found to be effective. It is hoped that these techniques can lay the foundation for effective closed-loop control of membrane wing micro-air-vehicles.

# Bibliography

- [1] R. M. Waldman and K. S. Breuer, “Camber and aerodynamic performance of compliant membrane wings,” *Journal of Fluids and Structures*, vol. 68, pp. 390–402, 2017.
- [2] R. E. Pelrine, R. D. Kornbluh, and J. P. Joseph, “Electrostriction of polymer dielectrics with compliant electrodes as a means of actuation,” *Sensors and Actuators, A*, vol. 64, no. 97, pp. 77–85, 1998.
- [3] R. Pelrine, R. Kornbluh, Q. Pei, and J. Joseph, “High speed electrically actuated elastomers with strain greater than 100%,” *Science*, vol. 287, no. 5454, pp. 836–839, 2000.
- [4] G. Kofod, P. Sommer-Larsen, R. Kornbluh, and R. Pelrine, “Actuation response of polyacrylate dielectric elastomers,” *Journal of Intelligent Materials Systems and Structures*, vol. 14, pp. 787–793, 2003.
- [5] P. Brochu and Q. Pei, “Advances in dielectric elastomers for actuators and artificial muscles,” *Macromolecular Rapid Communications*, vol. 31, no. 1, pp. 10–36, 2010.

- [6] F. Carpi, C. Salaris, and D. De Rossi, “Folded dielectric elastomer actuators,” *Smart Materials and Structures*, vol. 16, no. 2, 2007.
- [7] S. Shian, R. M. Diebold, and D. R. Clarke, “Tunable lenses using transparent dielectric elastomer actuators,” *Optics Express*, vol. 21, no. 7, p. 8669, 2013.
- [8] R. Heydt, R. Kornbluh, J. Eckerle, and R. Pelrine, “Sound radiation properties of dielectric elastomer electroactive polymer loudspeakers,” *Proceedings of SPIE*, vol. 61681, 2006.
- [9] R. Palakodeti and M. R. Kessler, “Influence of frequency and prestrain on the mechanical efficiency of dielectric electroactive polymer actuators,” *Materials Letters*, vol. 60, pp. 3437–3440, 2006.
- [10] S. Michel, X. Q. Zhang, M. Wissler, C. Löwe, and G. Kovacs, “A comparison between silicone and acrylic elastomers as dielectric materials in electroactive polymer actuators,” *Polymer International*, vol. 59, no. 3, pp. 391–399, 2010.
- [11] H. Wang, M. Lei, and S. Cai, “Viscoelastic deformation of a dielectric elastomer membrane subject to electromechanical loads,” *Journal of Applied Physics*, vol. 113, no. 21, 2013.
- [12] J. Sheng, H. Chen, L. Liu, J. Zhang, Y. Wang, and S. Jia, “Dynamic electromechanical performance of viscoelastic dielectric elastomers,” *Journal of Applied Physics*, vol. 114, no. 13, 2013.
- [13] R. Sarban, B. Lassen, and M. Willatzen, “Dynamic electromechanical modeling of dielectric elastomer actuators with metallic electrodes,” *IEEE/ASME Transactions on Mechatronics*, vol. 17, no. 5, pp. 960–967, 2012.

- [14] G. Y. Gu, U. Gupta, J. Zhu, L. M. Zhu, and X. Zhu, "Modeling of viscoelastic electromechanical behavior in a soft dielectric elastomer actuator," *IEEE Transactions on Robotics*, vol. 33, no. 5, pp. 1263–1271, 2017.
- [15] J. Guo, R. Xiao, H. S. Park, and T. D. Nguyen, "The temperature-dependent viscoelastic behavior of dielectric elastomers," *Journal of Applied Mechanics*, vol. 82, no. 9, 2015.
- [16] C. Chiang Foo, S. Cai, S. Jin Adrian Koh, S. Bauer, and Z. Suo, "Model of dissipative dielectric elastomers," *Journal of Applied Physics*, vol. 111, no. 3, 2012.
- [17] S. Wang, M. Decker, D. L. Henann, and S. Chester, "Modeling of dielectric viscoelastomers with application to electromechanical instabilities," *Journal of the Mechanics and Physics of Solids*, vol. 95, 06 2016.
- [18] F. Carpi, P. Chiarelli, A. Mazzoldi, and D. De Rossi, "Electromechanical characterisation of dielectric elastomer planar actuators: Comparative evaluation of different electrode materials and different counterloads," *Sensors and Actuators A: Physical*, vol. 107, no. 1, pp. 85–95, 2003.
- [19] S. Rosset and H. R. Shea, "Flexible and stretchable electrodes for dielectric elastomer actuators," *Applied Physics A: Materials Science and Processing*, vol. 110, no. 2, pp. 281–307, 2013.
- [20] P. Sommer-Larsen, J. Hooker, G. , K. West, M. Benslimane, and P. Graveson, "Response of dielectric elastomer actuators," *Proceedings of SPIE*, vol. 4329, pp. 157–63, 2001.
- [21] L. A. Toth and A. A. Goldenberg, "Control system design for a dielectric elastomer actuator: the sensory subsystem," *Proceedings of SPIE*, vol. 4695, pp. 323–334, 2002.

- [22] T. A. Gisby, S. Xie, E. P. Calius, and I. A. Anderson, “Integrated sensing and actuation of muscle-like actuators,” *Proceedings of SPIE*, vol. 6927, 2008.
- [23] K. Jung, K. J. Kim, and H. R. Choi, “A self-sensing dielectric elastomer actuator,” *Sensors and Actuators, A: Physical*, vol. 143, no. 2, pp. 343–351, 2008.
- [24] B. O’Brien, J. Thode, I. Anderson, E. Calius, E. Haemmerle, and S. Xie, “Integrated extension sensor based on resistance and voltage measurement for a dielectric elastomer,” *Proceedings of SPIE*, vol. 6524, 2007.
- [25] G. Rizzello, D. Naso, A. York, and S. Seelecke, “Self-sensing in dielectric electro-active polymer actuator using linear-in-parameters online estimation,” in *IEEE International Conference on Mechatronics (ICM)*, pp. 300–306, 2015.
- [26] G. Rizzello, D. Naso, A. York, and S. Seelecke, “A self-sensing approach for dielectric elastomer actuators based on online estimation algorithms,” *IEEE/ASME Transactions on Mechatronics*, vol. 22, no. 2, pp. 728–738, 2017.
- [27] T. A. Gisby, B. M. O’Brien, and I. A. Anderson, “Self sensing feedback for dielectric elastomer actuators,” *Applied Physics Letters*, vol. 102, no. 19, 2013.
- [28] D. Xu, A. Tairyck, and I. A. Anderson, “Localised strain sensing of dielectric elastomers in a stretchable soft-touch musical keyboard,” *Proceedings of SPIE*, vol. 9430, 2015.
- [29] D. Xu, S. Michel, T. McKay, B. O’Brien, T. Gisby, and I. Anderson, “Sensing frequency design for capacitance feedback of dielectric elastomers,” *Sensors and Actuators, A: Physical*, vol. 232, pp. 195–201, 2015.
- [30] W. Shyy, P. Ifju, and D. Viieru, “Membrane wing-based micro air vehicles,” *Applied Mechanics Reviews*, vol. 58, no. 4, p. 283, 2005.

- [31] A. Song, X. Tian, E. Israeli, R. Galvao, K. Bishop, S. Swartz, and K. Breuer, “Aeromechanics of membrane wings with implications for animal flight,” *AIAA Journal*, vol. 46, no. 8, pp. 2096–2106, 2008.
- [32] R. E. Gordnier, “High fidelity computational simulation of a membrane wing airfoil,” *Journal of Fluids and Structures*, vol. 25, no. 5, pp. 897–917, 2009.
- [33] L. Tregidgo, Z. Wang, and I. Gursul, “Fluid-structure interactions for a low aspect-ratio membrane wing at low Reynolds numbers,” in *41st AIAA Fluid Dynamics Conference and Exhibit*, pp. 1–17, 2011.
- [34] P. Rojratsirikul, M. S. Genc, Z. Wang, and I. Gursul, “Flow-induced vibrations of low aspect ratio rectangular membrane wings,” *Journal of Fluids and Structures*, vol. 27, no. 8, pp. 1296–1309, 2011.
- [35] P. Rojratsirikul, Z. Wang, and I. Gursul, “Effect of pre-strain and excess length on unsteady fluid-structure interactions of membrane airfoils,” *Journal of Fluids and Structures*, vol. 26, no. 3, pp. 359–376, 2010.
- [36] P. Rojratsirikul, Z. Wang, and I. Gursul, “Unsteady fluid-structure interactions of membrane airfoils at low Reynolds numbers,” *Experiments in Fluids*, vol. 46, no. 5, pp. 859–872, 2009.
- [37] J.-Z. Wu, X.-Y. Lu, A. G. Denny, M. Fan, and J.-M. Wu, “Post-stall flow control on an airfoil by local unsteady forcing,” *Journal of Fluid Mechanics*, vol. 371, pp. 21–58, 1998.
- [38] G. Jones, M. Santer, and G. Papadakis, “Control of low Reynolds number flow around an airfoil using periodic surface morphing: A numerical study,” *Journal of Fluids and Structures*, vol. 76, pp. 95–115, 2018.

- [39] M. M. Zhang, Y. Zhou, and L. Cheng, “Control of post-stall airfoil aerodynamics based on surface perturbation,” *AIAA Journal*, vol. 46, no. 10, pp. 2510–2519, 2008.
- [40] D. Munday, J. Jacob, and G. Huang, “Active flow control of separation on a wing with oscillatory camber,” *40th AIAA Aerospace Sciences Meeting and Exhibit*, vol. 39, no. 1, pp. 187–189, 2002.
- [41] F.-B. Hsiao, J.-Y. Shyu, and C.-F. Liu, “Control of wall-separated flow by internal acoustic excitation,” *AIAA Journal*, vol. 28, no. 8, pp. 1440–1446, 1990.
- [42] T. C. Corke, C. L. Enloe, and S. P. Wilkinson, “Dielectric barrier discharge plasma actuators for flow control,” *Annual Review of Fluid Mechanics*, vol. 42, pp. 505–529, 2010.
- [43] A. Glezer and M. Amitay, “Synthetic jets,” *Annual Review of Fluid Mechanics*, vol. 34, no. 29, pp. 503–529, 2002.
- [44] D. Greenblatt and I. J. Wygnanski, “Control of flow separation by periodic excitation,” *Progress in Aerospace Sciences*, vol. 36, no. 7, pp. 487–545, 2000.
- [45] M. Amitay and A. Glezer, “Role of actuation frequency in controlled flow reattachment over a stalled airfoil,” *AIAA Journal*, vol. 40, no. 2, pp. 209–216, 2002.
- [46] A. Glezer, M. Amitay, and A. M. Honohan, “Aspects of low- and high-frequency actuation for aerodynamic flow control,” *AIAA Journal*, vol. 43, no. 7, pp. 1501–1511, 2005.
- [47] A. Seifert, D. Greenblatt, and I. J. Wygnanski, “Active separation control: An overview of Reynolds and Mach numbers effects,” *Aerospace Science and Technology*, vol. 8, no. 7, pp. 569–582, 2004.

- [48] M. R. Hays, J. Morton, B. Dickinson, and K. Uttam, “Aerodynamic control of micro air vehicle wings using electroactive membranes,” *Journal of Intelligent Material Systems and Structures*, vol. 24, no. 7, pp. 862–878, 2012.
- [49] M. R. Hays, A. Hart, A. Guettler, L. Ukeiley, and W. S. Oates, “Fluid-structural dynamic characterization of an electroactive membrane wing,” *Journal of Intelligent Material Systems and Structures*, vol. 27, no. 11, pp. 1510–1522, 2015.
- [50] A. Barbu, R. de Kat, and B. Ganapathisubramani, “Aerodynamic performance of electro-active acrylic membrane wings,” *AIAA Journal*, vol. 56, no. 11, pp. 1–18, 2018.
- [51] O. M. Curet, A. Carrere, R. Waldman, and K. S. Breuer, “Aerodynamic characterization of a wing membrane with variable compliance,” *AIAA Journal*, vol. 52, no. 8, pp. 1749–1756, 2014.
- [52] S. Buoso and R. Palacios, “Viscoelastic effects in the aeromechanics of actuated elastomeric membrane wings,” *Journal of Fluids and Structures*, vol. 63, pp. 40–56, 2016.
- [53] S. Buoso and R. Palacios, “Electro-aeromechanical modelling of actuated membrane wings,” *Journal of Fluids and Structures*, vol. 58, pp. 188–202, 2015.
- [54] J. Kiser, M. Manning, D. Adler, and K. Breuer, “A reduced order model for dielectric elastomer actuators over a range of frequencies and prestrains,” *Applied Physics Letters*, vol. 109, no. 13, 2016.
- [55] S. J. A. Koh, X. Zhao, and Z. Suo, “Maximal energy that can be converted by a dielectric elastomer generator,” *Applied Physics Letters*, pp. 1–3, 2009.
- [56] R. D. Kornbluh, R. Pelrine, H. Prahald, A. Wong-Foy, B. McCoy, S. Kim, J. Eckerle, and T. Low, “From boots to buoys: Promises and challenges of di-

- electric elastomer energy harvesting,” in *Electroactivity in Polymeric Materials* (L. Rasmussen, ed.), pp. 67–93, Springer US, 2012.
- [57] R. Pelrine, R. Kornbluh, Q. Pei, S. Stanford, S. Oh, J. Eckerle, R. Full, M. Rosenthal, and K. Meijer, “Dielectric elastomer artificial muscle actuators : Toward biomimetic motion,” *Smart Structures and Materials*, vol. 4695, pp. 126–137, 2002.
- [58] M. Wissler and E. Mazza, “Mechanical behavior of an acrylic elastomer used in dielectric elastomer actuators,” *Sensors and Actuators, A: Physical*, vol. 134, no. 2, pp. 494–504, 2007.
- [59] Z. Suo, “Theory of dielectric elastomers,” *Acta Mechanica Solida Sinica*, vol. 23, no. 6, pp. 549–578, 2010.
- [60] N. Goulbourne, E. Mockensturm, and M. Frecker, “A nonlinear model for dielectric elastomer membranes,” *Journal of Applied Mechanics*, vol. 72, p. 899, 2005.
- [61] H. S. Park and T. D. Nguyen, “Viscoelastic effects on electromechanical instabilities in dielectric elastomers,” *Soft Matter*, vol. 9, no. 4, p. 1031, 2013.
- [62] W. N. Findley and F. A. Davis, *Creep and Relaxation of Nonlinear Viscoelastic Materials*. Courier Corporation, 1976.
- [63] W. Ma and L. Cross, “An experimental investigation of electromechanical response in a dielectric acrylic elastomer,” *Applied Physics A: Materials Science & Processing*, vol. 78, pp. 1201–1204, 2004.
- [64] P. Lochmatter, G. Kovacs, and S. Michel, “Characterization of dielectric elastomer actuators based on a hyperelastic film model,” *Sensors and Actuators, A: Physical*, vol. 135, no. 2, pp. 748–757, 2007.

- [65] M. Nishioka, M. Asai, and S. Yoshida, “Control of flow separation by acoustic excitation,” *AIAA Journal*, vol. 28, no. 11, pp. 1909–1915, 1990.
- [66] M. Gad-el Hak and D. M. Bushnell, “Separation control: Review,” *Journal of Fluids Engineering*, vol. 113, no. 1, p. 5, 1991.
- [67] K. Taira, C. W. Rowley, T. Colonius, and D. R. Williams, “Lift enhancement for low-aspect-ratio wings with periodic excitation,” *AIAA Journal*, vol. 48, no. 8, pp. 1785–1790, 2010.
- [68] M. D. Zhou, H. Fernholz, H. Ma, J. Wu, and J. Wu, “Vortex capture by a two-dimensional airfoil with a small oscillating leading-edge flap,” in *3rd Shear Flow Conference*, p. 3266, 1993.
- [69] R. Smith and W. Shyy, “Computational model of flexible membrane wings in steady laminar flow,” *AIAA Journal*, vol. 33, no. 10, pp. 1769–1777, 1995.
- [70] M. P. Païdoussis, S. J. Price, and E. De Langre, *Fluid-Structure Interactions: Cross-Flow-Induced Instabilities*. Cambridge University Press, 2010.
- [71] R. D. Blevins, *Flow-Induced Vibration*. Van Nostrand Reinhold Co., Inc., 1990.
- [72] R. D. Blevins and R. Plunkett, “Formulas for natural frequency and mode shape,” *Journal of Applied Mechanics*, vol. 47, p. 461, 1980.
- [73] Y. Abdel-Aziz, “Direct linear transformation from comparator coordinates in close-range photogrammetry,” in *ASP Symposium on Close-Range Photogrammetry in Illinois*, pp. 1–18, 1971.
- [74] L. E. Kinsler, A. R. Frey, A. B. Coppens, and J. V. Sanders, *Fundamentals of Acoustics*. Wiley, 1999.
- [75] C.-M. Ho and P. Huerre, “Perturbed free shear layers,” *Annual Review of Fluid Mechanics*, vol. 16, no. 1, pp. 365–422, 1984.

- [76] P. J. Schmid, “Dynamic mode decomposition of numerical and experimental data,” *Journal of Fluid Mechanics*, vol. 656, pp. 5–28, 2010.
- [77] K. Taira, S. L. Brunton, S. T. Dawson, C. W. Rowley, T. Colonius, B. J. McKeon, O. T. Schmidt, S. Gordeyev, V. Theofilis, and L. S. Ukeiley, “Modal analysis of fluid flows: An overview,” *AIAA Journal*, pp. 1–29, 2017.
- [78] T. A. Gisby, E. P. Calius, S. Xie, and I. A. Anderson, “An adaptive control method for dielectric elastomer devices,” *Electroactive Polymer Actuators and Devices (EAPAD), Proc. of SPIE*, vol. 6927, no. 69271C, 2008.
- [79] G. Rizzello, M. Hodgins, S. Seelecke, and D. Naso, “Self-sensing at low sampling-to-signal frequency ratio: an improved algorithm for dielectric elastomer actuators,” *2016 12th IEEE/ASME International Conference on Mechatronic and Embedded Systems and Applications (MESA)*, pp. 1–6, 2016.
- [80] D. Xu, A. Tairyck, and I. A. Anderson, “Stretch not flex: programmable rubber keyboard,” *Smart Materials and Structures*, vol. 25, no. 015012, 2016.
- [81] A. O’Halloran, F. O’Malley, and P. McHugh, “A review on dielectric elastomer actuators, technology, applications, and challenges,” *Journal of Applied Physics*, vol. 104, no. 7, 2008.
- [82] J. W. Harris and H. Stöcker, *Handbook of mathematics and computational science*. Springer Science & Business Media, 1998.
- [83] M. DiSalvo, D. M. Harris, S. Kantesaria, A. N. Pena, J. D. Allbritton-King, J. H. Cole, and N. L. Allbritton, “Characterization of tensioned pdms membranes for imaging cytometry on microrraft arrays,” *Analytical chemistry*, vol. 90, no. 7, pp. 4792–4800, 2018.